TRIBOTECHNOLOGIES OF STRENGTHENING AND WEAR MODELING OF STRUCTURAL MATERIALS

M. Stechyshyn
M. Macko
O. Dykha
S. Matiukh
J. Musial

TRIBOTECHNOLOGIES OF STRENGTHENING AND WEAR MODELING OF STRUCTURAL MATERIALS

Bydgoszcz, 2023

M. Stechyshyn, M. Macko, O. Dykha, S. Matiukh, J. Musial. Tribotechnologies of strengthening and wear modeling of structural materials. Bydgoszcz: Foundation of Mechatronics Development, 2023.

Reviewers:

Mykhaylo Pashechko
Prof. dr hab. eng, Department of Fundamental of Technology, Lublin University of Technology, Poland
Juozaas Padgurskas
Prof. Dr., Institute of Power and Transport Machinery Engineering, Vytautas Magnus University, Kaunas, Lithuania

ISBN 978-83-938655-8-1

85-343 Bydgoszcz, ul. Jeżynowa 19, Poland

TABLE OF CONTENTS

Chapter 4.
Tests of tribological and operational properties of lubricants

INTRODUCTION

Most machines and mechanisms fail as a result of wear of the working surfaces of the parts. Accordingly, increased attention is paid to the research of technologies for increasing wear resistance and restoration of machine parts. Among the large number of existing technologies in the field of surface engineering, recently preference is given to the introduction of methods of controlled modification of metal surfaces, which are based on the action of concentrated flows of energy and chemicals on the surface. Widely used are vacuum, laser and ion technologies, which allow to form the specified physical and chemical characteristics of the surface layers of metals and at the same time are characterized by the least energy-intensive technological processes. Among the listed technologies, from the point of view of energy intensity and universality of application, anhydrous is the most progressive, both for parts made of structural steels, and for parts of stamping and foundry productions, nodes of food and chemical enterprises, which are subject to intensive effects of various types of corrosion and mechanical wear. The effectiveness of technologies for increasing wear resistance is evaluated by comparing the quantitative indicators of the durability of modified parts according to the wear criterion. Reliable indicators of wear resistance can be obtained only from the results of wear tests of strengthened samples of materials. The application of the theory of test methods allows building analytical dependencies – models characterizing wear kinetics depending on the determining factors. In this way, wear models allow optimizing the parameters of strengthening technologies according to the criterion of the best wear resistance of structural materials.

The monograph consists of four chapters. In the first chapter of the monograph, the effect of regime (temperature, composition of the gas mixture, its pressure, and nitriding time) and energy (current density and electric field strength in the gas chamber) parameters on the structure, phase composition, and microhardness of the surfaces of structural steels nitrided in the glow discharge is investigated.

The second chapter analyzes the physicochemical and tribological characteristics of structural steels nitrided in an anhydrous environment during corrosion-mechanical destruction in an acidic model environment. The influence of the energy parameters of the discharge (specific capacity, current density and voltage in the gas discharge chamber) on the physicochemical and tribological properties of structural steels pre-nitrided in a glow discharge under dry friction conditions was studied.

The third chapter is devoted to computational and experimental modeling of the behavior of modern sliding and rolling tribosystems. The theory of methods of testing materials for wear was developed to construct analytical dependences of wear of materials on determining factors. Methodical examples of calculating wear and tribotechnical reliability of friction pairs are shown, taking into account the variability of operational factors.

The fourth chapter describes the general method of testing structural materials for wear with the determination of the basic quantitative parameters of the laws of wear under conditions of extreme friction. Methods for determining the deformation characteristics of the lubricated contact have been established for tribotechnical couplings working with lubrication. An analytical model of transient processes in lubricated tribosystems is constructed.

The book can be useful to scientists and young researchers in the field of creating new progressive integral technologies for strengthening and modeling the wear of structural materials.

Chapter 1.
TRIBOLOGICAL PROPERTIES OF STRUCTURAL STEEL MODIFIED BY ANHYDROUS NITRIDATION IN A GLOW DISCHARGE

1.1. Influence of the ionic nitriding of steels in glow discharge on the structure and properties of the coatings

The present work is a continuation of the investigations of vacuum-diffusion gas-discharge processes used to form modified surface layers of metals under the mutual influence of the autonomous parameters of treatment: temperature, the composition of a saturating medium, pressure in a gas-discharge chamber, and the duration of saturation. On the basis of the obtained experimental results, we formulate our ideas concerning the possibility of practical application of this principally new technological process based on the optimization of the combination of its autonomous modes of saturation, which would promote the formation of surface structures improving the reliability and durability of machine parts under the operating conditions. In this case, as a basis, we use an absolutely new energy model whose principal specific feature can be described as follows. The main role in the hardening of the surface layers of metals is played by the subprocesses that can be regarded as the most appropriate under the specific operating conditions of the products [1].

The analysis of the literature sources [2–4] demonstrates that all known theoretical models of ionic nitriding are, to a great extent, hypothetical. Many of these models have no analytic substantiation and the criteria for optimization of the nitrided surfaces (and, hence, the procedures of control over nitriding required to get the desired operational characteristics) are absent. The accumulation of a great amount of technological data that are not based on the general theoretical foundation does not promote the development of practical applications of the procedure of ion-plasma hardening of the products and frequently leads to the opposite results because the accumulated results are not based on the actual operation conditions.

In the planned cycle of works, we formulate absolutely new concepts of the theory of diffusion gas-discharge processes of ionic nitriding in metals based on the priority of the energy approaches [1]. From this viewpoint, the indicated processes were considered neither in Ukraine, nor abroad, despite the fact that the proposed approach opens absolutely new possibilities for the production of diffusion ion-nitrided layers with new properties and extends the sphere of their application in the field of hardening of the metal surfaces.

Methods of Investigations. We performed ion nitriding in glow discharge by using a specially designed installation at the Podillya Scientific Physicotechnological Center of the Khmel'nyts'kyi National University [1].

In our investigations, we chose the following materials extensively used for the production and the repair of elements of the technological equipment of food industry: 20, 45, 45Kh, U8A, 38KhMYuA and 12Kh18N10T steels. 38KhMYuA steel was taken to study the influence of alloying elements on the physicomechanical characteristics of the surfaces after ionic nitriding in glow discharge. We applied the methods of metallographic, electron-microscopic, and X-ray diffraction analyses and the method of ferromagnetic resonance.

The structure of cross section of the diffusion layer and the distribution of microhardness over its thickness were studied on etched microsections. The submicroscopic structure of the nitride zone was analyzed in a REM-200 scanning electron microscope. The X-ray phase diffraction analysis of the surface layers of the specimens was carried out in a DRON-200 diffractometer with the use of $K\alpha$-radiation.

The residual stresses were found by the Davidenkov method by measuring the deflection of plane specimens in the course of etching of the nitrided layer [6].

Results of Investigations and Discussion. The intensity of vacuum-diffusion ionic nitriding in glow discharge is 1.5–2 times higher than the intensity of furnace nitriding, which determines new properties of the ion-nitrided layers [3]. According to [1, 5], the equilibrium between the processes of spraying and deposition of nitrogen ions is attained for 4 h. Therefore, our main investigations of the properties of nitrided surfaces were performed for the indicated duration of the process.

Note that the changes in microhardness across the thickness of the diffusion layer characterize the fractions and distributions of the structural and phase components of the coating and may serve as the measure of the energy capacity of the surface layers [5, 7]. Therefore, we studied the influence of the parameters of ionic nitriding on the indicated characteristic (Figs. 1.1, *a*, *b*).

The analysis of the accumulated results of investigations enables us to formulate the following general regularities of changes in the microhardness of the nitrided zone depending on the parameters of the mode of nitriding:

(1) the maximum hardness increases with the content of carbon and the amount of alloying elements in the base (Fig. 1.1, *a*; curves *1*–*4*); the influence of the alloying elements (especially, of the nitride-forming elements) on the microhardness is much more pronounced than the influence of carbon (curves *1*–*3*);

(2) as the nitriding temperature increases, the microhardness of the nitrided zone decreases and the rate of decrease becomes higher as the degree of alloying and the carbon content of the base increase;

(3) the level of microhardness increases with the content of nitrogen and the pressure of the gas medium but the rate of increase is much lower than the rate of decrease in the case of growing temperature;

(4) the increase in the duration of nitriding for constant temperature, pressure, and the composition of gaseous mixture does not affect microhardness and promotes its smoother transition to the hardness of the base with simultaneous extension of the zone with higher levels of microhardness (Fig. 1.1, *b*).

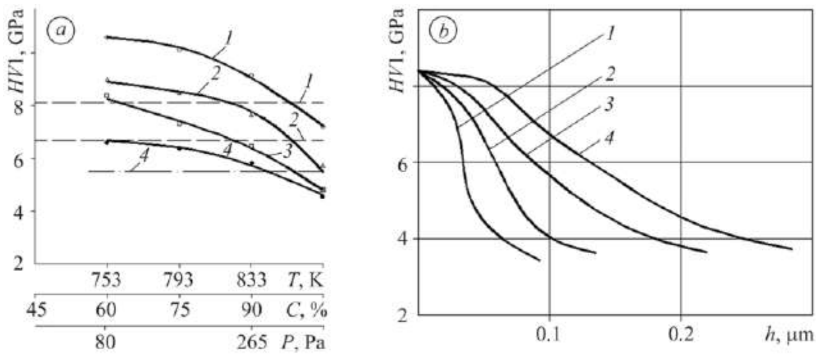

Fig. 1.1. Dependences of the microhardness of nitrided zone on temperature *T* (solid lines), nitrogen content *C* (dashed lines), and the pressure of gaseous mixture *P* (dash-dotted lines) for: *1* – 38KhMYuA, *2* – 45Kh, *3* – 45, *4* – 20 steels (*a*) and the distributions of microhardness HV1 over the thickness of the diffusion nitrided layers for specimens made of 45Kh steel for the following durations of nitriding: *1* – 1 h; *2* – 2 h; *3* – 3 h; *4* – 4 h (*b*)

The maximum microhardness of the nitrided zone is obtained for 38KhMYuA steel because the nitrides of alloying elements have a higher hardness, dispersion, and heat resistance as compared with iron nitrides. Moreover, the decrease in microhardness observed as the nitriding temperature increases is explained by a decrease in the degree of discreteness of nitrides. Since iron nitrides are characterized by the low heat resistance and high rate of coagulation [3], the level of hardness of carbon steels insignificantly depends on the nitriding temperature (Fig. 1.1, *a*, curve *4*).

According to the results obtained in [3], the dispersion of inclusions in the form of nitrides of alloying elements exerts the crucial influence on the level and distribution of microhardness over the thickness of the nitrided layer. Thus, the investigations of the fine structure of 45Kh nitrided steel in the REM-200 scanning electron microscope showed that, as the nitriding temperature increases from 833 to 873 °K, the surface area of nitrides becomes, on the average, 38 times larger and, hence, the level of microhardness decreases.

The obtained results are confirmed by the data of X-ray diffraction analysis. It is known that the maximum microhardness of the nitrided layer corresponds to the formation of coherent nuclei of the nitride phase, which lead to the most pronounced distortions of the crystal lattice of the matrix whose mean value is characterized by the width and intensity of the diffraction maxima of the α-phase. As the nitriding temperature and the size of nitride particles increase, the coherence is violated and the distortion of the crystal lattice of the matrix and the hardness of the layer decrease (Fig. 1.1, *a*).

The alloying elements increase the solubility of nitrogen in the alloyed α-phase and, hence, promote a decrease in the diffusion coefficient of nitrogen and in the thickness of the diffusion layer. The thickness also decreases with the increase in the carbon content of the matrix. In this case, the concentration of nitrogen in the surface layer of the ε-phase insignificantly varies. Thus, the fractions of the ε-phase on 20 and 45 steels are equal to 19 and 21 %, respectively.

The analysis of the influence of the parameters of ionic nitriding on the thicknesses of the nitride zone h_N and the diffusion layer h and microhardness HV1 revealed the possibility of efficient control over these characteristics, mainly by changing the temperature of the process. Hence, the nitriding temperature is the most universal energy parameter of the process (Fig. 1.2). In this case, the most intense growth of the diffusion layer was observed for 45 carbon steel (Fig. 1.2; curve *2* of the dependence $h = f(T)$. The least intensity of growth was detected for the 38KhMYuA alloyed steel (curve *3*).

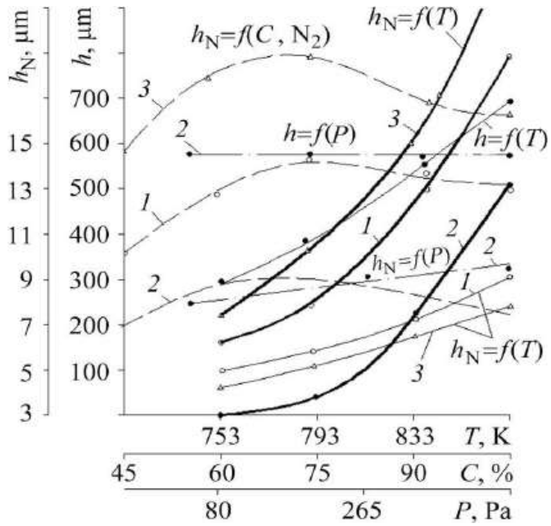

Fig. 1.2. Dependences of the depth of diffusion layer h (thick solid lines) and the thickness of nitride zone h_N (thin solid lines) on the temperature, nitrogen concentration in the saturating mixture (dashed lines) and pressure *P* (dash-dotted lines) for:
1 **– 45Kh,** ***2*** **– 45,** ***3*** **– 38KhMYuA steels**

This fact is explained by the low mobility of nitrogen in the nitrides of alloying elements, which block diffusion processes in the solid solution [3]. On the contrary, the depth and the intensity of growth of the nitride zone h_N increase with the degree of alloying with nitride forming elements (with the exception of aluminum and silicon which somewhat decrease the solubility of nitrogen) [3]. Then iron nitrides and alloying elements inhibit the diffusion of nitrogen into the bulk of the metal and the development of the zone of internal nitriding.

As the concentration of nitrogen in gaseous mixture increases to 75 %, the thickness of the nitride zone h_N also increases. However, the subsequent increase in the nitrogen concentration leads to a decrease in h_N. This is possibly explained by the deterioration of cleaning of the metal surface caused by the lower kinetic energy of nitrogen ions as compared with argon ions [1], Fig. 1.2; $h_N = f(C, N_2)$.

The elevation of the pressure of nitrogen-argon mixture exerts almost no influence on the thickness of the diffusion layer h but somewhat increases the thickness of the nitride zone hN (the dash-dotted lines in Fig. 1.2).

The application of the method of active planning of the experiments enables us to develop statistical models of the influence of ionic nitriding on the thickness and microhardness of the hardened layers. As a result of statistical processing of the experimental data on a significance level of 5 %, we obtain the following regression equations:

$$y_1 = 256{,}12 + 18{,}27x_1;$$

$$y_2 = 16{,}72+0{,}95x_1 + 0{,}16x_2 + 0{,}20x_3;$$

$$y_3 = 7{,}30 - 0{,}65x_1 + 0{,}08x_2 + 0{,}19x_3;$$

where y_1 is the total thickness of the diffusion layer h, y_2 is the thickness of the nitride zone h_N, y_3 is the level of microhardness HV_1, x_1 is the nitriding temperature, x_2 is the concentration of nitrogen in the gas mixture C, and x_3 is the pressure of gas mixture.

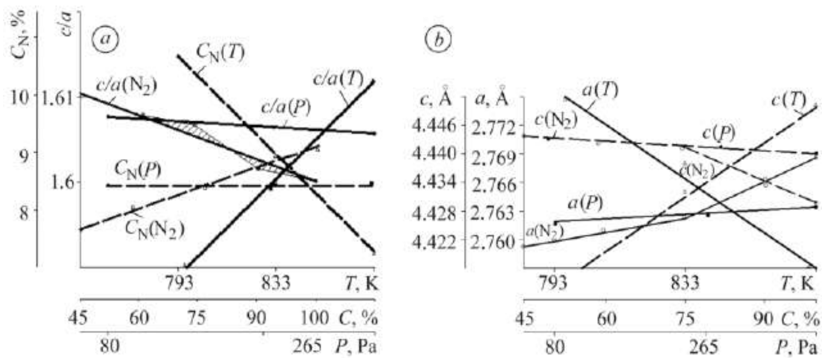

Fig. 1.3. Dependences of the ratio of lattice parameters (*c/a*), the concentration of nitrogen in the surface layer (C_N) (*a*) and the parameters and (*b*) on the mode of nitriding (*T*, *C* and *P*) of 45Kh steel

The analysis of the developed models confirms the results on ionic nitriding obtained earlier and allows one to determine the thicknesses of the nitride and diffusion zones and the microhardness of the nitride zone according to its known parameters.

In recent years, the investigations of the structural states of surface layers and the analysis of the process of wear of the metals based on the physics of strength and plasticity of crystalline bodies attract significant attention of the researchers [8].

The dependences of the parameters of crystal lattice on the mode of ionic nitriding were established with the help of the X-ray diffraction analysis. These dependences enable us to quantitatively evaluate the characteristics of strength of the surface layers (Fig. 1.3).

The results of the X-ray diffraction analysis are corroborated by the data of metallographic analyses, the levels of microhardness and the character of its distribution (Figs. 1.1 and 1.2). Thus, the lattice parameter *c* increases with the nitriding temperature, whereas the parameter strongly decreases (Fig. 3, *b*). Hence, the ratio c/a increases (Fig. 3, *a*). As a result of the diffusion of nitrogen into the depth of the diffusion layer, its concentration C_N on the surface of the nitride layer decreases with the increase in the nitriding temperature and, therefore, the microhardness of the nitride layer also decreases (Fig. 1.1, *a*).

The process of weakening of distortions of the crystal lattice (ratio c/a) with increase in the concentration of nitrogen in the gas mixture (the curve c/a (N_2) in Fig. 1.3, *a*) is simultaneously compensated by the increase in the concentration of nitrogen in the nitride zone CN (N_2) (Fig. 1.3, *a*) and causes an insignificant increase in the microhardness of the surface layer (Fig. 1.1).

The increase in the pressure of gas mixture has almost no influence on the ratio of the parameters c/a (P) (Fig. 1.3, *a*), which is confirmed by the character of changes in the parameters $c(P)$ and $a(P)$ (Fig. 1.3, *b*) and exerts almost no effect on the microhardness of the nitride zone under given conditions of changes in the pressure of the gas mixture in a gas-discharge chamber (Fig. 1.1, *a*; curve *4*).

However, the decrease in the ratio c/a observed as the concentration of nitrogen in the gas mixture (and simultaneously in the nitride layer) increases (Fig. 1.3, *a*) and also its deviations from the linear dependence within the range 75–90 % (shaded triangles in Fig. 1.3, *a*) require additional explanations. For this purpose, we plotted the dependences of the lattice parameters and on the mode of nitriding (Fig. 1.3, *b*). These dependences enable us to conclude that the parameter a increases with the concentration of nitrogen in the gas mixture, whereas *c* decreases.

When the nitrogen content becomes equal to 75 %, the rates of changes in the lattice parameters become inversely proportional, which enables us to describe the dependence of the ratio c/a on the nitrogen content of the gas mixture by a straight line (c/a (N_2) in Fig. 1.3, *a*). At the same time, the established regularities of changes in the parameters $c(N_2)$ and $a(N_2)$ enable us to substantiate the optimal choice of the mode of ionic nitriding in a gas mixture formed by 75 % N_2 + 25 % Ar.

The data of X-ray diffraction analysis enable us to conclude that, independently of the composition of gaseous atmosphere, the ε–($Fe_{2-3}N$), γ′–(Fe_4N), and α-phases are formed in the surface layer. In this case, the phase composition and the fractions of phase structures in the nitrided layer can be regulated by changing the parameters of the mode nitriding *T*, *C* and *P* (Fig. 1.4).

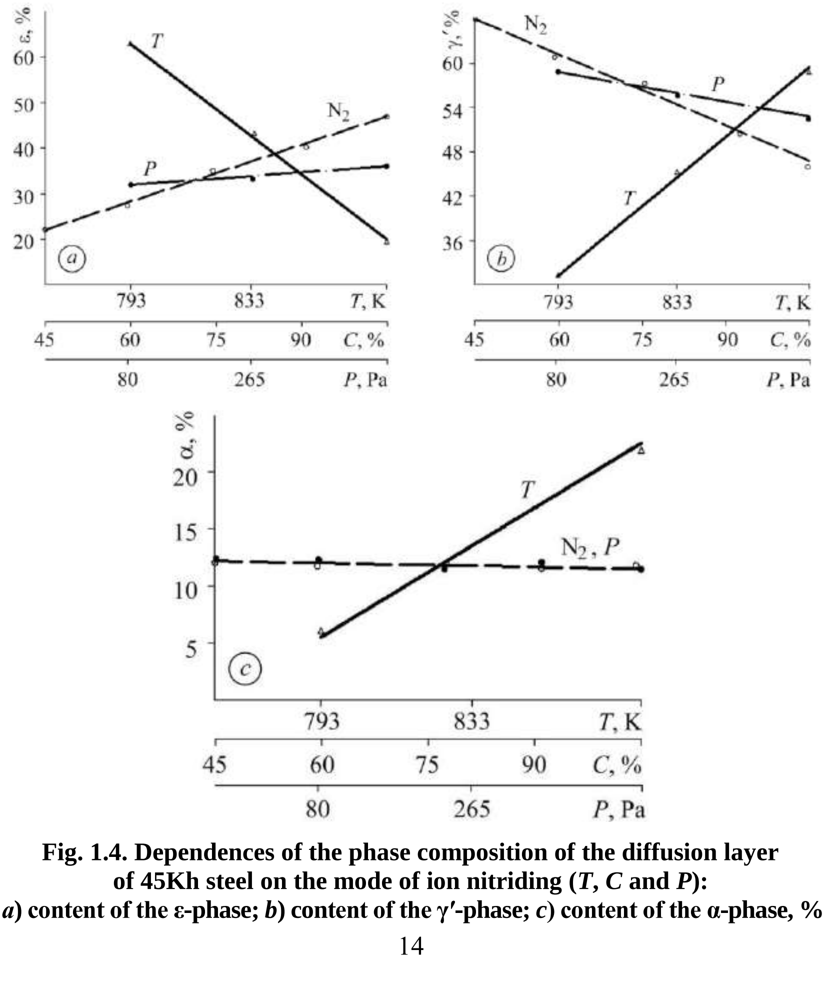

Fig. 1.4. Dependences of the phase composition of the diffusion layer of 45Kh steel on the mode of ion nitriding (*T*, *C* and *P*):
***a*) content of the ε-phase; *b*) content of the γ′-phase; *c*) content of the α-phase, %**

The analysis of the obtained dependences shows that the temperature of ionic nitriding exerts a strong influence on the amounts of certain phases. Thus, the amounts of the γ′- and α-phases in the surface layer increase with temperature (Fig. 1.4, *b*, *c*), whereas the amount of the ε-phase decreases (Fig. 1.4, *a*).

Moreover, the amount of ε-phase increases with the content of nitrogen and the pressure of gas mixture (Fig. 1.4, *a*) and, at the same time, the amount of the γ′-phase decreases (Fig. 1.4, *b*). In this case, the content of the α-phase remains practically invariable (Fig. 1.4, *c*). Its amount depends solely on the temperature of ionic nitriding in glow discharge, which is a function of the energy characteristics of the process (current density and voltages on the electrodes of the gas-discharge chamber).

In view of the strong difference between the physicochemical properties of the phase-structural components of the nitrided layer and the possibility of regulation of their amounts and fractions, we get an efficient tool for the creation of layers with prescribed characteristics of the surfaces.

The results of numerous investigations [1–3, 6] demonstrate that the structure of the layer and its phase composition specify the operating characteristics of the products. Thus, in particular, the high-hardness components formed on the basis of the ε-phase (Fe_2N) are used in open friction couples (gear wheels, sprockets of chain drives, conveyor pins, etc.). For closed friction couples (plane bearings, gear wheels, gear boxes, etc.), it is necessary to create a nitrided layer with developed nitride zone formed by low-nitrogen plastic nitride phases γ and γ′ (Fe_3N and Fe_4N), which are well running in, localize plastic strains, and inhibit the development of fracture processes in the component. The main contribution to the increase in the fatigue strength under alternating loads is made by the zone of internal nitriding (α-phase). It is also worth noting that the α-phase {but of the second kind, i.e., corresponding to the formation of the nitrides of alloying elements (TiN, ZrN and HfN) [3]} also increases the heat resistance.

For the reliable operation of products in corrosive media at high temperatures, it is reasonable to create diffusion layers with surface nitride zones. Due to its high corrosion resistance, the ε-phase blocks the transportation of oxygen atoms into the matrix and prevents the adsorption decrease in strength (Rehbinder effect) both under static conditions and under the action of alternating stresses [3, 6].

The subsequent X-ray diffraction investigations of the phase structural components of ion-nitrided layers would enable us to better comprehend the mechanisms of their formation, to evaluate their quantitative and qualitative influence on the physicochemical properties of nitrided surfaces, and (which is especially important) to modify their properties depending on the operating conditions of the machine parts.

On the basis of the results of our investigations and the analysis of literature sources, we substantiated the significance and urgency of the analysis of fine mechanisms of the ionic nitriding of metals in glow discharge for their practical application by the optimal combination of the parameters of technological mode with priority of the energy approaches.

The formulated general regularities of the variations of microhardness in the nitride zone depending on the autonomous parameters of the mode of nitriding are formulated and are substantiated by results of the X-ray diffraction analysis of the phase composition of nitrided surfaces.

The structure of the nitrided layer and its phase composition determine the physicomechanical characteristics of the surfaces of machine parts. For this reason, we obtained and analyzed the dependences of the thicknesses of the nitride zone h_N and diffusion layer h on the parameters of nitriding, temperature, composition of the gas mixture, and its pressure. We also developed statistical models of the relationship between the parameters of nitriding and the thicknesses of the nitride and diffusion zones and their microhardnesses. We performed the X-ray diffraction analysis of the phase structural components of the nitrided layers, analyzed the changes in the lattice parameters and for nitride particles depending on the concentration of nitrogen in the nitride zone C_N, and studied the phase composition of the diffusion layer on 45Kh steel as a function of the parameters of nitriding (T, C and P).

1.2. Corrosion and electrochemical characteristics of the metal surfaces (nitrided in glow discharge) in model acid media

The physicochemical properties of ion-nitrided metal surfaces are usually regulated by the changes in the saturation parameters: temperature, pressure, the composition of saturating mixture, and the duration of saturation, which enables us to get the best characteristics of strength, plasticity, fatigue resistance, friction coefficients, and wear intensity in rolling friction [8]. There are works in which the modes of surface hardening by the coatings [9, 10] are directed toward the enhancement of their adhesion to the base metal and improvement of the physicomechanical characteristics of the coating materials: wear resistance, contact durability, corrosion resistance, etc. [11]. At the same time, the influence of the energy parameters on the physicomechanical characteristics of nitrided layers remains poorly studied, the relationship between their phase and structural components is not analyzed on the basis of general regularities of the physics of strength and plasticity of crystalline solids, and also little attention was given to the investigation of the dynamic equilibrium of the processes of formation and destruction of the films of secondary structures, i.e., to the phenomena of structural adaptation [12]. However, just these directions of investigations enable us to establish the most general regularities of the wear and fracture of metals.

The aim of the present work is to study the influence of nitriding in the glow discharge (NGD) on the corro-sion and electrochemical properties of metals in acid media typical of the operation of plants of the food industry of Ukraine and also to substantiate the results obtained from the viewpoint of the physics of strength and plasticity of crystalline metals.

Methods of Investigations. We carried out the procedure of NGD in an UATR-1 industrial installation of the Physical-and-Technological Center of the Khmel'nyts'kyi National University, which corresponds to a diode-type model on the direct current and is additionally equipped with heating elements placed in a gas-discharge chamber. This feature enables us to perform arbitrary changes in the energy parameter, i.e., in the voltage U, and determine the current density I (the ratio of current to the total area of the batch and suspension) by a combination of an arbitrarily given voltage, the pressure of the gas mixture, and the duration of nitriding ($\tau = 4h$).

We monitored the assigned temperature with the help of an APIRS-M pyrometer, which was calibrated directly under the conditions of glow discharge in the chamber of our installation. To decrease the electrochemical heterogeneity of the nitride zone, we used two-stage nitriding with an addition of a gas mixture (90 % nitrogen plus 10 % propane) for 1 h in the last stage. For this purpose, we included a balloon with propane in the sys-tem of gas preparation.

We studied the corrosion and electrochemical characteristics of nitrided layers for Armco iron, 20, 45, 40Kh, and 38KhMYuA steels, and SCh20 grey cast iron in a model acid medium [buffer solution of citric acid (5 g/liter)] and double-substituted sodium phosphate

(10 g/liter) with pH 6.5 by the gravimetric and potenti-ostatic methods based on plotting polarization curves and according to the kinetics of changes in the potential with time [13].

The X-ray diffraction analysis was carried out in a DRON-3 diffractometer in filtered radiation within the angle range $2\theta = 20–100^{\circ}$ at a scanning step of 0.1 for a time of holding of 10 sec.

The structure and thickness of the phase components of nitrided layers were determined on metallographic sections etched in a 3 % alcohol solution of nitric acid with the use of a MIM-10 metallographic microscope.

Experimental Results and Discussion. Clearly, the corrosion resistance and kinetics of the electrochemical processes in nitrided materials are determined by several factors and, first of all, by the phase composition, concentration of nitrogen in the diffusion layer, type of alloying elements, the degree of alloying of the matrix, and the concentration of carbon in the base. Hence, for the same steel, depending on the operation conditions and energy parameters of the NGD, its electro-chemical characteristics may undergo significant changes. Thus, unlike the strength characteristics, the corro-sion resistance of steel in acid media decreases as carbon content increases and as the degree of alloying of the base decreases (Fig. 1.5). For Armco iron and 20 steel, the corrosion rate decreases over the thickness of the dif-fusion layer and approaches the corrosion rate of the unhardened layer. For 45 steel, as the carbon content in-creases, the corrosion rate in acid media, on the contrary, increases across the thickness of the layer (Fig. 1.5).

As the degree of alloying increases, the corrosion rate also increases and gradually approaches the values of corrosion resistance of the base (Fig. 1.1, Table 1.1). Thus, the corrosion rate on the surface of nitrided 38KhMYuA steel is 2.7 times higher than for 20 steel. Moreover, at a certain distance from the surface, it becomes four times higher (Table 1.1). Another important conclusion is fact that the nitride zone exerts practically no influence on the corrosion resistance in acid media (Fig. 1.5). The accumulated results show that the corrosion rate in solutions of acids is controlled by cathodic processes, and the overvoltage of hydrogen release becomes lower as the degree of alloying and carbon content of the base increase. This leads to an increase in the number of microgalvanic couples facilitating the acceleration of corrosion processes. The X-ray diffraction analysis shows that nitrided materials are dissolved in acid media according to the heterogeneous electrochemical mechanism.

Thus, for the nitrided 40Kh steel after holding in an acid medium for 720 h and the removal of corrosion products from the surface, the diffraction maxima of the γ-phase disappear and the intensity of diffraction maxima of the γ-phase decreases with simultaneous increase in the diffraction maxima of ferrous oxides.

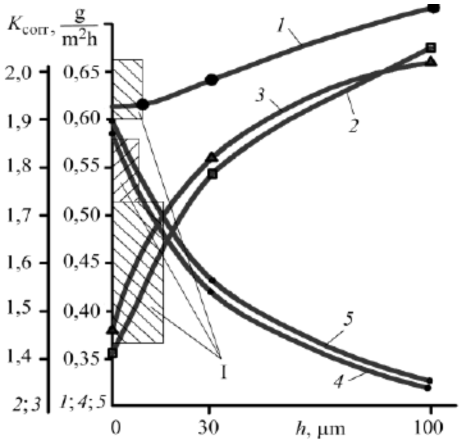

Fig. 1.5. Variations of the corrosion rate of nitrided steels (843 °K, 75 % N_2 + 25% Ar, 265 Pa; 4 h) in the acid medium across the thickness of the diffusion layer: (I) nitride zone; *1* – 45 steel, *2* – 38KhMYuA steel, *3* – 40Kh steel, *4* – γ–Fe, *5* – 20 steel

Table 1.1

Corrosion Rates (g/(m²h)) of Nitrided Materials Held in an Acid Model Medium for 720 h

Material	Distance from the surfaces, μm						Without nitriding
	Nitriding			Combined nitriding			
	0	30	100	0	30	100	
Armco-iron	0.585	0.415	0.328	0.590	0.384	0.291	0.236
20 steel	0.593	0.442	0.336	0.587	0.400	0.301	0.263
45 steel	0.612	0.644	0.721	0.560	0.579	0.724	0.762
40Kh steel	1.411	1.797	2.069	1.409	1.623	2.164	3.069
38KhMYuA steel	1.448	1.811	0.992	1.438	1.616	2.179	3.132
SCh18 cast iron	3.271	3.491	3.623	3.252	3.372	3.426	6.148

In analyzing the accumulated results, we can assume that the decrease in the degree of heterogeneity of the nitride zone leads to the enhancement of the corrosion resistance of the metals. As one of the methods of this kind, we can mention the NGD with a combined mode of saturation with the addition of carbon-containing gases (e.g., propane) in the final stage of the process (Fig. 1.6).

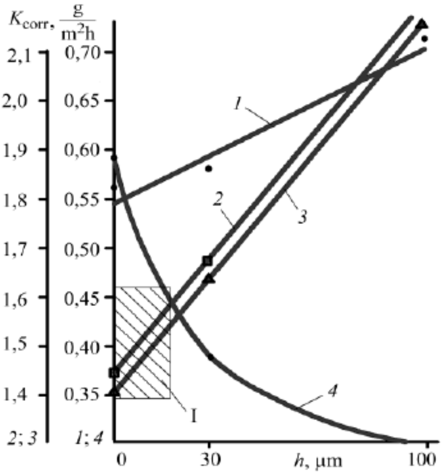

Fig. 1.6. Variations of the corrosion rate of nitrided steels in model acid media over the thickness of the diffusion layer after combined nitriding (843 °K, 75 % N_2 + 25 % Ar, 265 Pa, τ = 3 h; 90 % N_2 and 10 % propane for τ = 1 h): (I) nitride zone; *1* – 45 steel, *2* – 38KhMYuA steel, *3* – 40Kh steel, *4* – Armco iron

The character of changes in the corrosion rate for the investigated metals remains practically invariable but can be approximated (with a sufficiently high accuracy) by rectilinear dependences (except Armco iron and 20 steel). It is worth noting that the corrosion resistance of the nitride zone becomes 1.4–1.9 higher as compared with the case of nitriding performed without adding propane (Figs. 1.5 and 1.6). In view of the fact that carbides can be regarded as a more efficient means of hardening of the diffusion layer of nitrided metals than nitrides [14] we can expect an increase in the wear resistance of steels nitrided by the combined method in corrosive media.

This is very important because corrosion itself is not the main factor of destruction of the surface but plays the role of catalyst in the course of stress-corrosion processes (friction, cavitation, hydroerosion, etc.) in corrosive media. The changes in physicochemical properties of metals exert the strongest influence on the potential of the metal–medium systems (cavitation and hydroerosion) or metal–medium–metal systems (friction). By using the relationship between the potential and internal stresses, we found their values in microvolumes of the metal near crack bottom and in the regions of other defects: on grain boundaries, in some crystals, etc. (both in the course of loading and after it) [14].

It is shown [14] that the process of microplastic deformation in the subsurface layers of the metal can be split, in the general case, into two main stages: in the initial stage, their abnormal behavior is observed as the easier formation and motion of dislocations in the subsurface layers of crystalline metals, as compared with their inner layers. In the next stage (barrier effect of the surface), a layer with high density of dislocations, the so-called “debris-layer”, is formed near the surface. This layer blocks the exit of slip planes onto the crystal surfaces and inhibits the development of volume deformation. The barrier effect of the surface becomes stronger in the presence of various coatings. Since the electrode potential determines the thermodynamic state of metal in the medium, we can represent it in the form:

$$\Delta\varphi = -\frac{U}{k \cdot F}, \tag{1.1}$$

where $\Delta\varphi$ is the increment of the potential, V; U is the thermodynamic potential of the surface layer, J; k is the proportionality coefficient (k = 2 for iron), and F = 26,8 A·h/g.eqv is the Faraday constant.

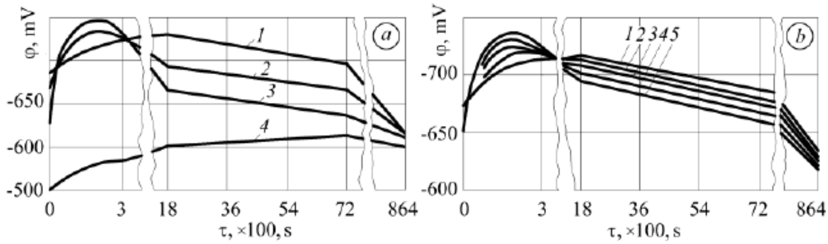

Fig. 1.7. Kinetics of changes in the electrode potential in the acid medium after nitriding (100 % N_2, 265 Pa) at temperatures of 873 °K (*1*), 833 °K (*2*), 793°K (*3*) after nitriding in the glow discharge (*4*) (*a*) and depending on the composition of a gas mixture (*b*): *1* – 45 % N_2, *2* – 60, *3* – 75, *4* – 90 % (balance, argon), *5* – 100 % N_2

According to [15], it is possible to use, instead of U, the energy of elastic distortions of the lattice with dislocations. Thus, knowing the dynamics of changes in the potential of metal–medium system, we can find the changes in the thermodynamic potential of the surface layer, the energy of elastic distortions of the crystal lattice, and hence, the efficiency of the barrier effect of the debris-layer. The investigations of the kinetics of changes in the electrode potentials of materials nitrided in acid media under various conditions (Fig. 1.3) demonstrate that the electrode potential, as an integral characteristic of state of the subsurface layer, clearly determines its dynamic equilibrium with the medium depending on the joint action of external factors, including the parameters of the NGD.

The statistical processing of the accumulated experimental results enable us to obtain mathematical models of the electrode potential y_1 and the corrosion rate y_2 in the case of mixing with a circular velocity of 1 m/sec (40Kh steel):

$$\begin{cases} y_1 = 684,5 + 9x_1 - 2,5x_3; \\ y_2 = 22,34 + 1,02x_1 - 0,3x_2 - 2,5x_3, \end{cases} \tag{1.2}$$

where x_1 is the temperature of NGD, x_2 is the nitrogen content of the gas mixture, and x_3 is its pressure.

Thus, it is easy to see that the temperature of nitriding most strongly affects the potential and the corrosion rate. If this temperature increases, then the electrode potential takes higher (in modulus) negative values (becomes less noble), and the corrosion resistance becomes lower. As the nitrogen content of the gaseous medium x_2 and pressure x_3 increase, then the potential and corrosion rate of 40Kh steel in acid media decrease. Similar dependences of the corrosion resistance were also obtained for the other considered metals (Table 1.1).

The kinetics of changes in the potential of nitrided and unhardened metals shows (Fig. 1.3) that the initial period of interaction with acid media is characterized by the active dissolution of the surface layer (the potential shifts to the negative side). However, for the unhardened metals, the corrosion rate in the initial period is lower than for the nitrided metals (Table 1.1), which can be explained by the less pronounced heterogeneity of the surface layer. This is confirmed by the fact that the rate of changes in the potential at the initial moment of contact of the specimens nitrided at T = 793 °K (Fig. 1.7, *a*, curve *3*) with a solution is much higher as compared with the specimens nitrided at higher temperatures (Fig. 1.8, *a*, curves *1* and *2*).

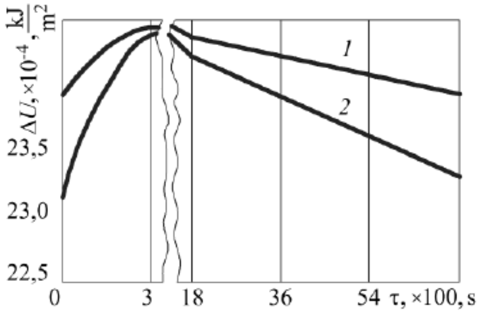

Fig. 1.8. Kinetics of changes in the thermodynamic potential of the nitrided surfaces (843 °K, 75 % N_2 + 25 % Ar, 265 Pa, 4 h) of SCh20 cast iron and 20 and 45 steels (*1*), 40Kh and 38KhMYuA steels (*2*) in the acid medium

Table 1.2.

Corrosion Rates (g/(m^{2}h)) of Nitrided Materials in Model Acid Media with and without Periodic Removals of the Protective Films

Material	Without removal	With removal of the films	Degree of increase in the corrosion rate
20 steel	0.593	0.861	1.45
45 steel	0.612	1.103	1.80
40Kh steel	1.411	3.102	2.20
38KhMYuA steel	1.448	3.382	2.34
SCh18 cast iron	3.271	3.972	1.21
U8A steel	6.035	6.839	1.13

As temperature decreases, the amount of the α-phase in the surface layer increases and, hence, its hetero-geneity also increases, which leads to the intensification of corrosion processes, especially in the initial period of contact of the specimens with acid solutions (~5 min). After this, corrosion products protect the base surface against destruction and, for a certain period (~24 h), the corrosion rates of hardened and unhardened metals are comparable. However, in the process of stress corrosion wear of the components of friction units, the corrosion products are permanently removed from the friction surfaces. The periodic removal (every 70 h for 560 h) of the corrosion products (Table 1.2) increases the rate of corrosion of nitrided metals by a factor of 1.2–1.8

for carbon steels and SCh20 cast iron and by a factor of 2–2.3 for alloyed steels.

Thus, the corrosion resistance of nitrided metals in acid media is determined, to a large extent, by the rate of formation of protective films of corrosion products on their surfaces and this rate increases with the carbon con-tent of the base and the degree of its alloying.

The analysis of relation (1.1) shows that the thermodynamic potential is a function of the electrode potential, i.e., $U = f(\Delta\varphi)$. The results of calculations performed by using this relation reveal the growth of the thermody-namic potential of the nitrided surface of 40Kh steel in the acid medium as compared with NGD ($\Delta\varphi = -120$ mV), to a value of 23.16 kJ/cm^2. The kinetics of changes in the thermodynamic potential (Fig. 1.8) shows that, from the onset of contact of the specimen with the acid medium, the crystal lattice of the surface layers is intensely reconstructed as a result of which the thermodynamic potential decreases to its initial value. In this case, the amplitude of the energy of elastic distortions of the lattice increases with the degree of alloying of the base (Fig. 1.8, curve *2*).

The interaction of dislocations with the free surface was studied in numerous works [12–14]. As follows from these results, if a dislocation approaches the free surface, then the energy of its deformation decreases because the free surface provides an escape to the strain field and we observe the appearance of a force pushing the dislocation onto the surface, i.e., the so-called force of the mirror image. However, it is opposed by the resistance force required for the formation of a step on the surface. In the general case of interaction between dislocations and the free surface, it is necessary to consider the ratio of the force of mirror image to the force that blocks the attainment of the surface by the analyzed dislocation:

$$g = -\frac{G \cdot b}{c \cdot \gamma}, \tag{1.3}$$

where G is the shear modulus, b is the Burgers vector, γ is the surface energy of dislocation step, and $c = 4$ is the proportionality factor [16].

The ratio g for iron given by this formula is 2.36, i.e., the force pushing the dislocation out is 2.36 times higher than the force that blocks the exit of dislocation onto the surface.

Clearly, in the first approximation, we can assume that $\gamma \cong 4$ [14] and, hence, $g = G{\cdot}b$. According to the results presented in [14], for iron, we get $U = 2J/m^2$. By using the data obtained earlier (Fig. 1.8), after nitriding, we find $g = 12.5$. In other words, in the initial stage of the corrosion action of acid media on the nitrided surface, the forces of pushing out the dislocations are almost five times greater (as compared with the nonnitrided surface) than the forces of attraction of dislocations. After 5 min of interaction with the medium, this ratio becomes six times larger. This fact explains the abnormal behavior of nitrided layers in the initial stage of interaction with the acid medium. After this, the potential energy of the surface decreases but a high possibility of structural reconstruction depending on the external conditions remains.

Unlike the strength characteristics, as the carbon content in the base and the degree of its alloying increase, the corrosion rates of steels in acid media increase across the thickness of the nitrided diffusion layer and gradually approach the values of corrosion rate of the base. The nitride zone almost does not affect the corrosion resistance in acid media. The addition of propane to the gas mixture leads to a decrease in the electrochemical heterogeneity of the nitride zone and its corrosion resistance becomes 1.4–1.9 times higher.

It is established that the thermodynamic potential of the surface is closely connected with the electrode potential and its much higher value for the nitrided surface explains the elevated rate of formation of the protective films.

The abnormal behavior of the nitrided layers is explained by both their high thermodynamic potentials and high values of the forces of mirror image of the debris-layer, which promotes the exit of dislocations on the sur-face at the initial moment of contact with corrosive media, thus decreasing the surface energy, and then blocks the exit of dislocations on the surface.

1.3. Strength and plasticity of the surface layers of metals nitrided in glow discharge

In the course of nitriding of iron alloys, high hardness is exhibited solely by the ε-phase (Fe_4N) occupying an insignificant volume on the nitrided layer. This is why the process of nitriding of carbon steels insignifi-cantly increases the hardness of the ε-phase $(Fe, Me)_4N$ and the zones of internal nitriding. At the same time, in the case of alloyed steels, nitriding, on the contrary, strongly increases their hardness [15], which is mainly connected with the formation of dispersed nitrides of the alloying elements (TiN, CrN, and $(Fe, Al)_4N$) in the asolution. The hardness of these elements depends on the nitrogen content in the phases and is equal to 20, 10–15, and 10–12 GPa, respectively [16]. Their formation is accompanied by elastic distortions of the crystalline lattices of the α-phase, which is confirmed by the results of investigations carried out in [16]. The highest hardness corresponds to the nitriding temperature of formation of the nitrides completely coherent with the α-phase. In this case, strong fields of elastic distortions in the lattice of the matrix promote the process of hardening.

In the course of nitriding at high temperatures, particles of nitrides become coarser, coherence is violated, and, therefore, the level of hardness decreases. In this case, the dislocations are arrested at the nitride precipitates until the applied stresses attain values sufficient for bending the dislocations and their passing between the particles. The maximum stresses for the motion of dislocations correspond to the distances between the particles comparable with their sizes [16]. By changing the parameters of the mode of nitriding (temperature, pressure, composition of the gas mixture, and duration of nitriding) and the energy parameters (current density and voltage), it is possible to obtain precipitates with different morphologies and geometries and, hence, with different degrees of hardening in the diffusion zone [17]. In what follows, we perform the theoretical investigation of changes in the fine structure of nitrided diffu-sion coatings with an aim to get their maximum strength and plasticity.

Procedure of Investigation. Nitriding was performed in a UATR-1 diode-type installation in the DC mode in hydrogen-free gas atmos-pheres (75 % N–25 % Ar and 90 % N–10 % Ar) at nitriding temperatures of 793–873 °K under a pressure of gas mixtures varying within the range 80–450 Pa for 1–4 h. The installation was additionally equipped with heating elements located in a gas-discharge chamber, which makes it possible to arbitrarily change the voltage and current density [18].

The microhardness was measured by a PMT-3 device with recording the values of H 0.1 both on the surface and at distances of 0.25, 50, 100, 200, 300, 500 and 1000 μm from it. The structure and thickness of the phase components of nitrided samples were determined with the help of an MIM-10 metallographic microscope after their etching in a 3 % alcohol solution of nitric acid. The X-ray diffraction analysis was carried out in a DRON-3 diffractometer in the filtered radiation of iron anode within the range of angles $2Q$ = 20–100° with scanning steps of 0.1° and an exposure of 10 sec.

Results and Discussion. The characteristics of the zone of internal nitriding, i.e., its strength and plasticity, have the maximum influence on the wear resistance of nitrided layers. This is why the surfaces of the components of open friction couples must have high hardness [19], whereas in closed friction couples, one surface should be soft and guarantee the possibility of running-in in the contact zone.

According to the theory of dislocations, the effect of hardening observed in the process of formation of the zones of internal nitriding is a result of retardation of dislocations by the precipitates of iron nitrides and nitrides of alloying elements. Therefore, their degree of hardening can be found according to the Orowan and Motto–Nabarro models.

In view of the corrections proposed by some authors, in the case of incoherent precipitates, the Orowan formula for tangential stresses takes the form:

$$\Delta\tau = 0,85\frac{Gb}{2\pi\left(R-2r\right)}0,5\left[1+\left(1-\mu\right)\right]\ln\frac{R-2r}{2b}, \qquad (1.4)$$

where $\Delta\tau$ is the degree of hardening, G is the shear modulus of the material of the matrix, b is the Burgers vector, r is the radius of particles, R is the distance between their centers, and μ is Poisson's ratio of the material of the particles.

By using the accumulated results of investigations of the fine structure of nitrided layers [15], the available literature data [17, 20], and the MathCad software, we computed the variations of strength $\Delta\tau$ depending on the diameters of nitride particles (5–100 nm) and distance between their centers (5–140.5 nm).

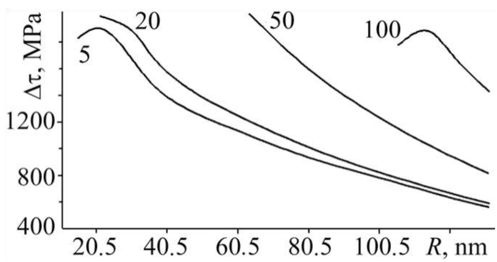

Fig. 1.9. Dependences of the degree of hardening $\Delta\tau$ on the size *R* of the zone of internal nitriding of iron, i.e., the distance between the centers of particles according to the Orowan model; the numbers near the curves correspond to the diameters of particles, nm

It was estab-lished (Fig. 1.9) that the resistance of the zone of internal nitriding to shear plastic strains becomes weaker as the size of dispersed phases and the distance between them increase.

In the case of coherent precipitates, particles are cut by dislocations in the process of deformation. In this case, according to the Motto–Nabarro model, the yield stresses depend on the arithmetic mean of the internal stresses:

$$\tau = 2G\cdot\varepsilon\cdot f_V, \tag{1.5}$$

where τ, G are the shear stresses and f_V is the volume fraction of particles:

$$f_V = (0,81d/R)^3, \tag{1.6}$$

where, $d = 2r$ is the diameter of particles and R is the distance between the centers of particles. The degree of hardening is determined as follows [16]:

$$\varepsilon = \frac{3KS}{SK + 4G}, \tag{1.7}$$

where $K = (E/3)(1-2\mu)$ is the bulk modulus of particles, E is Young's modulus of the material of particles, and $S = C/2$ is the parameter of distortion of the matrix lattice [17]. As a result, the computational formula for the evaluation of the critical shear stress takes the form:

$$\tau = \frac{2GE(1-2\mu)C/2}{\left[C/2E(1-2\mu)\right]/3 + 4G}(0,81\alpha/R)^3, \tag{1.8}$$

By using formula (1.8), for the evaluation of shear stresses in the zone of internal nitriding of iron and its alloys with coherent chromium and titanium precipitates, we obtain the dependences of the degree of hardening τ on the diameter of particles (2–80 nm) and the distance between them (2–180 nm), Fig. 1.10. The initial data for numerical calculations were taken from the literature [15–20].

It was established that the internal nitrided layer can be maximally hardened by optimizing the diameters of coherent and incoherent precipitates and the distance between them. Thus, the contemporary technologies of nitriding in glow discharge do not take into account this factor of hardening for the optimization of the properties of materials and, therefore, do not completely realize all potentialities introduced in the nitriding processes.

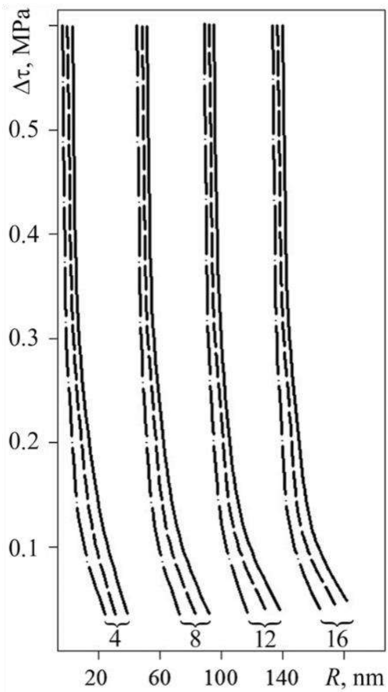

Fig. 1.10. Dependences of the degree of hardening of the zone of internal nitriding of iron alloys on the distance between the centers of nitride particles according to the Motto–Nabarro model. The numbers near the curves correspond to the diameters of particles, nm. The solid curves correspond to CrN, the dotted curves correspond to Cr_2N, and the dash-dotted curves correspond to TiN

The numerical analyses performed according to formula (5) also confirm the dependence of the degree of hardening of the zone of internal nitriding on the volume fraction of precipitating nitrides and their nature (Fig. 1.11). In this case, the hardening action of nitrides of alloying elements (Ti and Cr) is almost identical (curves 1 and 2 in Fig. 1.11). At the same time, the effect of hardening of the matrix by carbides (curves *3*) shows that it is reason-able to perform carbonitriding with an aim to increase the strength and plasticity of the zone of internal nitriding, which was corroborated by the results of investigations of the corrosion-mechanical wear of nitrided steels in acid, alkali, and neutral corrosive media [15].

We now represent the Motto–Nabarro formula in a somewhat different form:

$$\tau \approx 0,6\frac{Gb}{r}\sqrt[3]{f_V}\,. \tag{1.9}$$

It is easy to see that the effect of hardening strongly depends on the size *r* of precipitating particles and depends weaker on their total volume content. In Fig. 1.11 (curve *4*), we illustrate the possibility of hardening of the matrices of 20 and 45 carbon steels by decreasing the range of particle sizes of nitrides. Thus, to make the shear strength three times higher, it is necessary to make the range of particle sizes two times smaller.

It was discovered (Fig. 1.11) that the effect of hardening of the iron matrix by titanium nitrides (TiN) is more pronounced than in the case of hardening by chromium nitrides (CrN) but it seems to be reasonable to form carbides of the alloying elements.

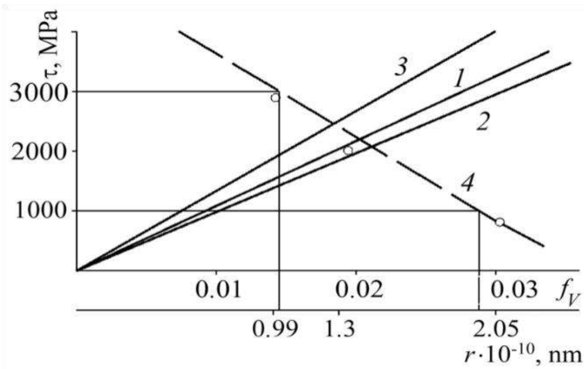

Fig. 1.11. Influence of the volume fraction of nitrides f_V – (*1*) TiN; (*2*) CrN and tungsten carbide (*3*) and the radius of dispersed nitride particles τ (curve *4* corresponds to τ = *f*(*r*)) on the shear stresses in the zone of internal nitriding (Motto–Nabarro model)

In this case, the hardening actions of the nitrides of alloying elements (Cr, Zr, W, Al, etc.) are almost equal (curves *1* and *2* in Fig. 1.11). In particular, the variations of the moduli of elasticity of different materials at room temperature [20] and the results of theoretical calculations confirm the efficiency of (Fe, Me)$_n$(NC)- or (Fe, Me)$_n$(NCO)-type carbide phases of alloying elements, i.e., of the carbonitride and carbooxynitride phases.

It was established that it is possible to attain a strength of 300–400 MPa as a result of nitriding of carbon low-alloy steels and to elevate the value of τ for 38KhMYuA steel up to 700–800 MPa by increasing the degree of alloying [20]. However, according to the theoretical estimates, it may vary from 45 up to 5000 MPa, which makes it possible to increase the strength of the nitrided layer (Fig. 1.11).

In [16], it was proposed to determine the characteristics of plasticity not according to the results of microhardness measurements [18] but from the loading diagrams, where the role of a criterion of plasticity is played by the ratio of the area bounded by the region of loading and unloading to the total area under the curve of the diagram, which is proportional to the total work of pressing.

It was discovered that, for the nitrided 45 steel, μ= 80 % (for the Fe_3N and Fe_4N phases) or 65 % for the Fe_2N phase, i.e., the high-nitrogen ε-phase has the minimum plasticity, whereas the Fe_3N and Fe_4N low-nitrogen nitride phases and Fe_3NC, Fe_2NC coatings of mixed carbonitride type have high plasticities.

It is shown that nitrided layers can be maximally hardened by optimizing the structure of coherent and incoherent precipitates of nitrides. It is also established that the plasticity of nitrided layers depends on their phase compositions. The high-nitrogen ζ- and ε-phases are characterized by the minimum plasticity, whereas the Fe3N and Fe_4N low-nitrogen phases are characterized by the maximum plasticity. The composition of the alloys can be predicted according the volume fraction of nitrides in the matrix and the concentration of alloying elements bound in nitrides.

1.4. Residual stresses in layers of structural steels nitrided in glow discharge

The procedure of nitriding in glow discharge (NGD) is one of the most widespread means of the surface hardening of metals by concentrated energy sources. This procedure enables us to control the process of saturation of the surface with an aim to obtain modified layers with given structures and phase compositions on the basis of a nitrogen-containing α-solid solution either with external nitride zone, or without this zone, or with nitride zone based solely on the ε- or γ'-

phases. The thickness and phase composition of the modified layer are determined by the properties of nitrided steel. The nitride zone containing solely the γ'-phase is sufficiently plastic, whereas the zone formed by the ε-phase is less plastic but has a higher corrosion resistance. A single-phase zone improves the mechanical properties of the nitrided surface as compared with the two-phase ($\varepsilon + \gamma'$)-zone characterized by the enhanced brittleness. However, for high friction rates (more than 3 m/sec), the two-phase zone prevents the adhesive interaction of the components of friction couples. The most plastic layer has no nitride zone. Generally speaking, the thinner the nitride zone, the more plastic the nitrided layer. However, its resistance to abrasive wear is lower, especially under the conditions of dry friction.

Thus, both the thickness and phase composition of the modified layer should be regulated taking into account the specific conditions of operation of the products. Thus, in particular, for products operating in corro- sive media and under the conditions of wear with low contact loads, it is necessary to have a nitrided layer with developed nitride zone guaranteeing their high corrosion resistance and the realization of the process of running- in of the friction surfaces.

The nitrided layer without nitride zone is recommended for the elements operating under the conditions of wear under high specific dynamic loads. Under the conditions of friction without lubrication, the corrosion and abrasive wear resistances are lower.

The process of modification of the surfaces in the course of NGD is regulated by changing the technological parameters of nitriding. They are separated into two groups: operating parameters (surface temperature, pressure in the discharge chamber, composition of the gas mixture, and the duration of saturation) and power parameters (current density and voltage on the electrodes of the discharge chamber). The influence of operating parameters on the thickness, phase composition, and properties of the modified layer was analyzed in [21–24]. At the same time, their influence on the residual stresses and the character of their distribution is studied insufficiently well.

It is known that the durability of elements under the action of various loads depends on the relationship between the distribution of residual stresses, the zone of their action, and the type of complex stressed state. In the course of saturation of the surface layers of steels with nitrogen, the surface stresses are formed due to the changes in their chemical composition and the phase and structural characteristics [23, 25]. This strongly affects the workability of the elements [26].

In what follows, we study the influence of the technological parameters of NGD (temperature, pressure, composition of the gas medium, and the duration of nitriding) on the residual stresses and their distribution over the thicknesses of the nitrided diffusion layers in structural steels.

Methods of Investigations. The procedure of NGD was realized in a UATP installation [7]. The residual stresses were determined by the Davidenkov method, by measuring the bending deflection of a flat specimen (plate 70 × 10 × 2.5 mm in size with Rz = 0.63) in the course of etching of the nitrided stressed layer.

After the mechanical treatment and polishing, the specimen was nitrided and its three sides were covered with a melted mixture of paraffin and rosin in the 2:1 ratio. The tip of inductive gauge of a BV-662 self-recorder was supported by a corundum plate that was not etched in solutions of nitric and hydrofluoric acids.

The etching rate was 3–10 μm/min. For the nitrided specimens (small thicknesses of components of the coating; see Fig. 1.12–1.14), we used the lower part of the range of etching rates.

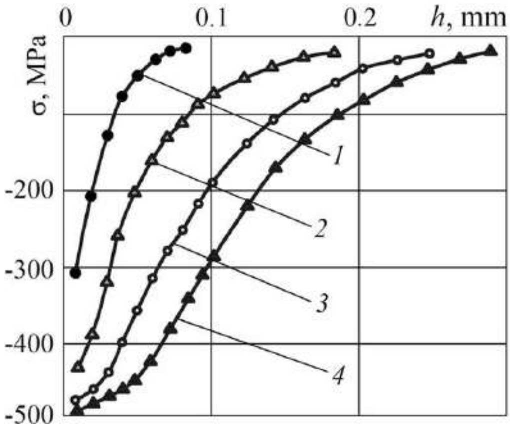

Fig. 1.12. Dependences of changes in the residual stresses across the thickness of the diffusion layer of 40Kh steel on the duration of NGD: *1* – 1 h, *2* – 2.5, *3* – 4, *4* – 6 h

The residual stresses are computed by the formula [28]:

$$\sigma = \frac{a^2 E}{3в^2}\frac{dx}{da}, \tag{1.10}$$

where E is the elasticity modulus of a structural component of the diffusion layer, and b are the thickness and width of the specimen, respectively, and dx/da is the strain rate. In the sections where the level of strains undergoes rapid changes, in particular, at the points of inflection of the curve of bending deflection, we performed calculations with regard for the elasticity modulus of the material measured after the procedure of etching of a part of the coating [29]:

$$E = E_0 \frac{\alpha+\beta}{2} + E_П \left(1 - \frac{\alpha+\beta}{2}\right);$$
$$\alpha = 1 - \left(\frac{2h_П}{a-u}\right)^3; \;\; \beta = \left[1 - \frac{2\left(h_П - u\right)}{a-u}\right] \qquad (1.11)$$

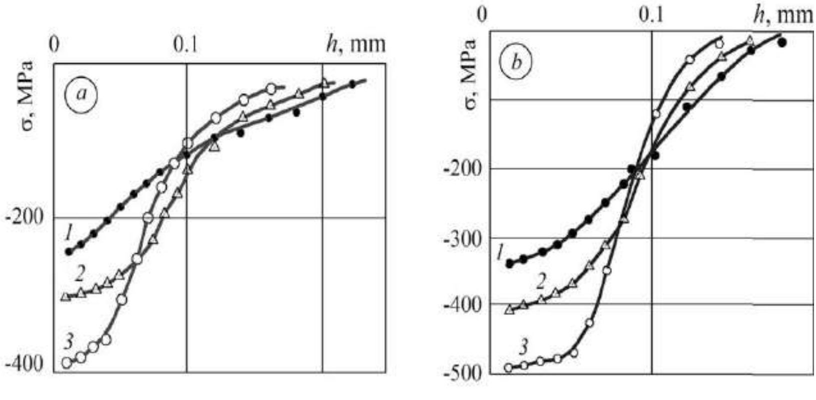

Fig. 1.13. Variations of the residual stresses across the thickness of diffusion layers of 40Kh (*a*) and 38KhMYuA (*b*) steels depending on the nitriding temperature (100 % N, 265 Pa): *1* – 873; *2* – 833; *3* – 793 °K

Here, E_0 is the elasticity modulus of the material of the specimen base; E coat is the elasticity modulus of the coating; h coat is the thickness of the structural layer of the coating, and h is a half thickness of the etched layer of the coating.

In view of relation (*1*), we get:

$$\sigma = \frac{a^2}{3в^2}\left[E_0 \frac{\alpha+\beta}{2} + E_П\left(1 - \frac{\alpha+\beta}{2}\right)\right]\frac{dx}{da}. \qquad (1.12)$$

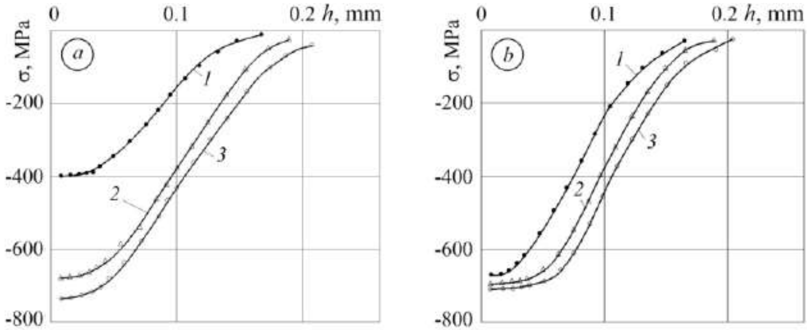

Fig. 1.14. Variations of residual stresses over the thickness of the diffusion layer of 38KhMYuA steel depending on the composition of the gas mixture (*a*) (*T* = 833 °K and *p* = 265 Pa): *1* – 100 % N_2; *2* – 45 N_2 + 55 Ar; *3* – 75 N_2 + 25 Ar and on the gas pressure (*b*) (*T* = 833 °K and 75 % N_2 + 25 % Ar): *1* – 450; *2* – 80; *3* – 265 Pa

We studied the magnitude and character of the distribution of stresses σ for 45; 40Kh, and 38KhMYuA nitrided structural steels as functions of temperature, time, the composition of gas mixtures, and their pressure. The thickness of the diffusion layer of nitrided specimens was determined with the help of a MYM-10 metallographic microscope after their etching in a 3 % solution of nitric acid in alcohol.

Results and Discussion**.** In the course of NGD, the residual compression stresses are formed in the surface layer. Varying the operating and power characteristics of the process of nitriding, we can get the diagrams required for a given mode of operation.

It was discovered (Fig. 1.12) that the residual compressive stresses first increase with the duration of NGD. Then, after 4 h of nitriding, they are stabilized depending on the degree of alloying and the content of carbon in the matrix.

As the duration of NGD increases, the maximum value of residual stresses does not increase but the depth of the zone of their action increases. We also detected their smoother decrease across the thickness of the diffusion layer.

It is clear that one of the most important causes of the formation of residual compressive stresses is a large specific volume of the nitride phases as compared with the volume of iron. In the increasing order, they can be arranged as follows: Fe $\rightarrow \gamma' \rightarrow \varepsilon \rightarrow \xi$. The nitrides of alloying elements have, as a rule, larger specific volumes than iron nitrides [30].

Thus, the maximum residual stresses should be formed on the surfaces of nitrided layers. In fact, their maximum is located at a distance of 10–15 μm from the surface (Fig. 1.12). In other words, the ξ-phase is formed as a result of phase recrystallization in the process of cooling in the zones of the ε-phase characterized by nitrogen concentrations varying within the range 11–11.35 wt.% [23]. It was shown that the ξ- and ε-phases contain a large number of pores with oxidized walls. This is explained by the metastability of nitride phases. The nitrogen present in these phases tries to escape in the molecular form. As a result, the dislocations, grain boundaries, and cavities are filled with the gas in the high-pressure state either in the atomic or in the molecular form. It seems likely that, under the action of its pressure, the dislocations are transformed into pores, which is detected by the metallographic analysis. The walls of the pores are oxidized in the course of cooling of the products because the volumes of the ε-phase are connected with the surface by channels allowing the penetration of air. In the process of initiation and development of pores, the residual stresses relax and are shifted into the depth of the diffusion layer. As the temperature of NGD increases, the zone of their action is expanded with simultaneous decrease in their values.

The residual stresses strongly depend on the composition of gas mixture during nitriding. As the content of argon increases, the process of saturation intensifies and the residual stresses become higher. In this case, their maximum values were recorded in the case of nitriding in a 75 % N_2 + 25% Ar mixture, which is explained by the character of changes in the parameters of crystal lattice [25]. The dependences of the parameters of crystal lattice and on the nitrogen content were obtained according to the results of X-ray phase diffraction analysis. They show that, as the nitrogen content in a gas mixture increases, the parameter increases with simultaneous decrease in the parameter. For the nitrogen content equal to 75 %, the rate of changes in these parameter varies inversely, which reveals a more pronounced distortion of the crystal lattices of the phase components of the diffusively nitrided layer and, hence, the elevation of residual stresses. A similar dependence was obtained by analyzing the influence of gas pressure on the distribution of residual stresses in the diffusion layer. Despite the fact that the thickness of the nitride zone is greater for high nitrogen concentrations in gas mixtures [25], the residual stresses decrease as the brittleness of these layers increases. Therefore, the maximum value corresponds to a pressure of gas mixture equal to 265 Pa (Fig. 1.14, *b*).

By using the method of active planning of experiments, we constructed the following mathematical models of formation of the residual stresses in nitrided layers (for 40Kh steel):

$$y = 418{,}1 - 28{,}6x_1 + 6{,}1x_2 + 2{,}1x_3, \quad (1.13)$$

where x_1 is temperature, x_2 is the nitrogen content, and x_3 is the pressure of gas mixture.

It was discovered that the residual stresses are, for the most part, affected by the nitriding temperature. Thus, they decrease as temperature increases. Moreover, as the nitrogen content of the gas mixture and its pressure increase, the maximum residual stresses become somewhat higher but, at the same time, the zone of their action becomes somewhat smaller (Fig. 1.14). In this case, the maximum values were obtained in the course of nitriding in a 75 % N_2 + 25 % Ar gas mixture under a pressure of 265 Pa.

We obtained the experimental dependences of the residual compressive stresses in structural steels after NGD on the duration and temperature of nitriding, the composition of gas mixtures, and gas pressure. It is shown that the nitriding temperature exerts the strongest influence: as it increases, the residual stresses decrease and the zone of their action becomes smaller. We plotted the dependences of the residual compressive stresses on the temperature, nitrogen content, and pressure. Their maximum values in the course of nitriding were recorded for a gas mixture with the following composition: 75 % N_2 + 25 % Ar under a pressure of 265 Pa.

1.5. Fatigue strength of nitrided steels in corrosion-active media of the food enterprises

The electrochemical fatigue fracture of metals under the conditions of stress-corrosion wear in corrosive media (CM) of the food enterprises [31] requires the investigation of the fatigue characteristics of metals. However, these characteristics are studied quite poorly, which restricts the possibilities of development of scientifically substantiated recommendations for the choice of friction units in technological installations used in the food industry.

The aim of the present work is to study the influence of the modes of nitriding in glow discharge (NGD) on the fatigue life and strength of nitrided structural steels in model corrosive media of food enterprises.

Methods of Investigations. The NGD was carried out in a UATR-1 installation designed and produced at the research-experimental base of the Podil's'kyi Scientific-Technological Center of the Khmelnytskyi National University [32]. The diode-type DC UATR-1 installation operates in waterless gaseous media. It is additionally equipped with heating elements placed in a gas-discharge chamber, which enables one to arbitrarily vary the voltage and the current density [33]. To study the low-cycle lifetime, we used a modernized installation IP-2 designed at Karpenko Physicomechanical Institute of the Ukrainian National Academy of Sciences [34]. On this installation, we tested plane specimens for the pure bending by a stiff loading scheme. The specimens were subjected to the elastoplasic deformation by bending with a frequency of 0.38 sec^{-1}. The high-cycle durability was studied on a vibration stand VÈDS-200 with electromagnetic excitation. The specimens were bent by the cantilever scheme at a resonance with the first form of vibrations [35].

According to work [35], the disjoining action of oxides in the fatigue tests in CM affects insignificantly the cracks with sizes > 2.5 mm and strongly at the early stages of their propagation. Therefore, we ceased the test, if the crack length attained 0.5 mm. We accepted 10^7 and $5 \cdot 10^7$ loading cycles as the bases of tests in air and in CM, respectively. The influence of a strengthening on the cyclic durability was determined on specimens with stress concentrators which were cut before the nitriding.

The degree of influence of the diffusion coatings on the durability of details is closely related to their strength properties. The strength of nitrided specimens was tested on an installation "ALA-TOO" of the IMASh-20-75 type. The loading evenness was 1.5 % of the applied load, which ensures the mean rate of deformation to be $3.3 \cdot 10^{-6}$ m/sec if the error of the movement velocity of a specimen holder is 1 %. The ultimate strength was determined by the largest load preceding the fracture of a specimen. We studied 20, 45, 40Kh, and 38KhMYuA steels, by using the metallographic, electron-microscopic, and X-ray diffraction analyses. We carried out the tests for the fatigue durability in buffer aqueous solutions which model the majority of working media at food enterprises: neutral (condensate in evaporators), acidic (bisubstituted sodium phosphate Na_2HPO_4 – 10 g/liter, citric acid $C_2H_8O_7$ – 5 g/liter), and alkaline (calcium oxide CaO – 250 g/liter and sucrose – 15 % of the mass of CaO) media.

The studies of the low-cycle lifetime of nitrided steels showed (Table 1.3) that the nitriding temperature has the highest effect on the lifetime: the low-cycle lifetime decreases, as the temperature increases.

Table 1.3

Low-Cycle Lifetime under the Elastoplastic Deformation of Specimens (ε = 0.75 %) in an Acidic Medium for Different NGD Modes

Steel	Number of cycles N prior to fracture										
	Temperature, °K[1]			Content of nitrogen, %[2]				Pressure, Pa[3]			
	793	833	873	45	60	75	90	100	80	265	450
38KhMYuA	3190	2485	2030	2412	2415	2460	2458	2485	2400	2460	2450
40Kh	3150	2390	1690	2400	2405	2430	2395	2398	2386	2430	2427
45	2840	2620	2480	2630	2620	2640	2642	2620	2600	2640	2630
20	2700	2540	2410	2510	2520	2540	2550	2540	2520	2540	2540

Comments: 1) 100 % N_2, 265 Pa; 2) 833 °K, 265 Pa.

The tests for static strength indicate that NGD causes some increase in the static strength characteristics of 20, 45, and 38KhMYuA steels and an insignificant decrease for 40Kh steel. At the same time, the plasticity of the studied steels decreases significantly, which is caused by an increase in the hardness of the surface layer as a result of NGD (Table 1.4).

Table 1.4

Mechanical Properties of Steels

Steel	σ_y, MPa	σ_u, MPa	δ, %	ψ, %	A, kN·m/m^3
38KhMYuA	880/950	1050/1200	9/5	40/20	85/50
40Kh	840/830	1000/1000	10/6	50/25	90/50
45	340/450	580/670	15/10	40/30	70/60
20	230/330	390/500	20/15	55/40	65/60

Comments: Numerator – improved steel; denominator – nitrided steel (833 °K, 75 % N_2 + 25 % Ar, 265 Pa).

It is established (Table 1.3) that the durability limit for nitrided steels increases with the strength of a core. We note that the fracture foci are usually placed under the surface layer during the nitriding. Therefore, the nitride zone composition insignificantly affects the fatigue characteristics, and an increase in the resistance to a low-cycle deformation is mainly determined by the strength characteristics of a core. However, the significant factor for the improvement of the fatigue durability is the diffusion layer thickness. Its decrease [36] and the simultaneous increase in the strength of a core result in an increase in the number of cycles prior to the fracture under a low-cycle load.

The application of the method of active planning of experiments enabled us to develop a statistical model of low-cycle lifetime of 40Kh steel in an acidic medium (ε = 0.5%):

$$Y = 4{,}90 - 0{,}20x_1 + 0{,}03x_2 + 0{,}03x_3, \quad (1.14)$$

where x_1 is the NGD temperature, x_2 is the content of nitrogen in a gas mixture, and x_3 is its pressure.

The analysis of the developed model shows that the nitriding temperature has the highest statistical influence on the low-cycle durability. As it increases, the durability of specimens decreases. On the contrary, an increase in the content of nitrogen in a gas mixture and in its pressure increases slightly the fatigue durability of 45 and 40Kh steels under a low-cycle loading (Fig. 1.15).

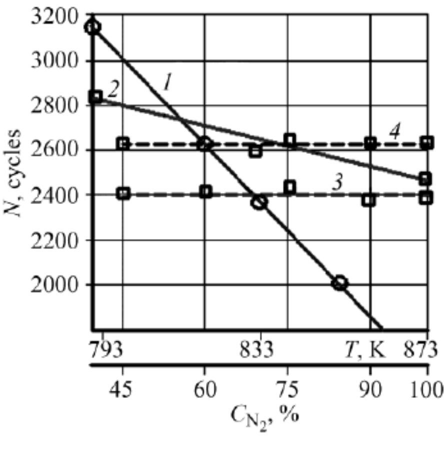

Fig. 1.15. Dependences of the number of cycles before the fracture of specimens at a low-cycle loading (ε = 0.75 %) in the acidic environment on the temperature (*1, 2*) and on the nitrogen content (*3, 4*) under NGD: *1, 3* – 40Kh steel, *2, 4* – 45 steel

It is established that, as the deformation amplitude increases, the difference in the lifetimes of nonhardened steels decreases and practically disappears at $\varepsilon \geq 3$ %. It is obvious that its action is stronger than the influence of the structure and the strength characteristics of the studied steels. In this case, a steel with higher specific work A of a deformation (Table 1.4) has a higher fatigue durability under a low-cycle loading (Fig. 1.16, curves *1* and *4*). As is seen (Figs. 1.16 and 1.17), NGD is not efficient for all media for $\varepsilon > 0.25$ %. Under a low-cycle loading, the general regularity is a decrease in the lifetime of steels, as their plasticity decreases. Therefore, NGD decreases the number of loading cycles prior to the fracture (Table 1.4), by decreasing the plasticity. In this case, the firmer the nitrided steel, the faster its durability decreases in acidic media. This is explained by an increase in a shift of the potential to the negative side at higher deforming stresses which are always higher in firmer steels. This results in an acceleration of the corrosion and in the hydrogen embrittlement at the tips of cracks.

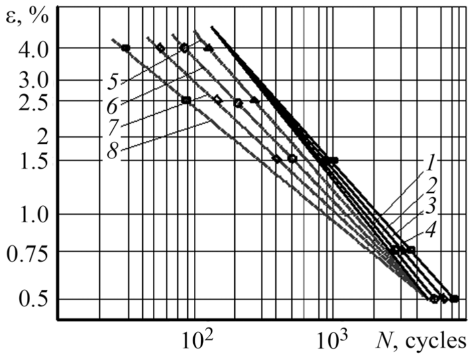

Fig. 1.16. Resistance to a low-cycle loading of nonhardened (*1–4*) and nitrided (833 °K, 75 % N_2 + 25 % Ar, 265 Pa) (*5–8*) 40Kh (*1, 8*), 38NMYuA (*2, 7*), 45 (*3, 5*) and 20 steels (*4, 6*) in an acidic model environment

Our analysis shows (Fig. 1.17) that the number of cycles prior to the fracture under a low-cycle loading of nitrided and nonhardened steels in alkaline media is higher than in air, condensate of evaporators, and acidic media. An increase in the low-cycle fatigue durability in an alkaline medium as compared with the durability in air is explained by the formation of a hydroxide layer on the surface of specimens. This hampers the access of oxygen to the deformation zone and blocks the rise of dislocations to the surface.

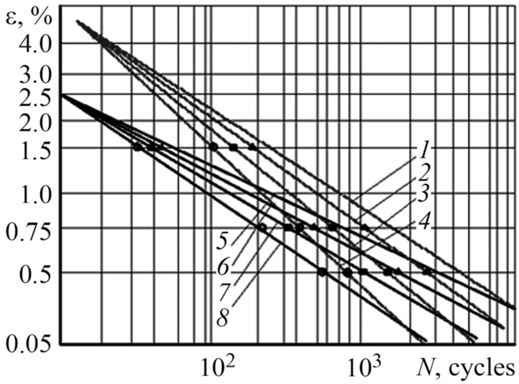

Fig. 1.17. Resistance to a low-cycle loading of improved (*1–4*) and nitrided (833 °K, 75 % N_2 + 25 % Ar, 265 Pa) 40Kh steels (*5–8*) in the following media: *1, 5* – alkaline, *2, 6* – air, *3, 7* – neutral (condensate with pH 7 in evaporators), *4, 8* – acidic (pH 6.5) media

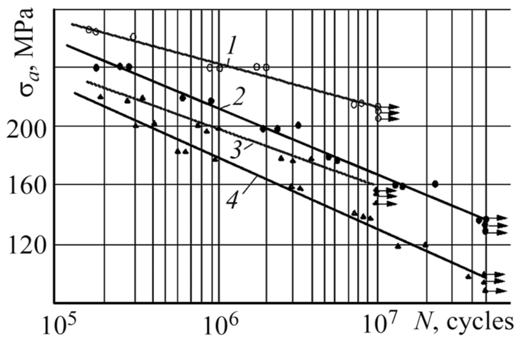

Fig. 1.18. Resistance to the high-cycle loading of nitrided (833 °K, 75 % N_2 + 25 % Ar, 265 Pa) (*1, 2*) and improved (*3, 4*) specimens made of 40Kh steel in air (*1, 3*) and in an acidic medium (*2, 4*)

The fatigue durability in a condensate in evaporators which has a lower corrosion activity as compared with acidic media slightly increases. However, as the deformation amplitude increases, the influence of the corrosion activity of a medium is leveled. For $\varepsilon \geq 2.5$ % for nitrided specimens and for $\varepsilon \geq 4$ % for improved specimens, their durabilities in air and in a corrosion medium coincide (Fig. 1.17). In this case, it is clearly seen that, starting from the deformation amplitude $\varepsilon \geq 2.5$ %, the use of NGD to increase the low-cycle durability is not efficient.

The durability of details of friction units is determined mainly by the resistance to the fatigue high-cycle fracture under the conditions of contact of details of the equipment at food enterprises with CM. For the definite conditions of loading of a friction contact, the low-cycle fracture can transit to the high-cycle fracture and vice versa. The studies indicate (Fig. 1.18) that the high-cycle durability of 40Kh steel after NGD increases by at least 35 % and by 30 % in an acidic medium.

It is known that if a metal operates under the action of stresses, the diffusion layer hampers the rise of dislo- cations to the surface, by preventing the initiation and propagation of microcracks. In addition, the durability limit of nitrided steels in corrosive media increases with the corrosion resistance [36] and the residual compressive stresses after NGD in surface layers.

The application of the method of active planning of experiments enabled us to develop a statistical model of high-cycle lifetime of 40Kh steel in the acidic model medium:

$$N \cdot 10^7 = 15{,}52 - 0{,}025T + 0{,}008C_{\mathrm{N}_2} + 0{,}0006P, \ldots\ldots..(1.15)$$

where T is the nitriding temperature, °K, C_{N2} is the content of nitrogen in a gas mixture, %, and P is its pressure, Pa.

Relation (1.15) indicates that the number of cycles prior to the fracture N is mostly affected by the nitriding temperature whose increase leads to a decrease in the durability. The fatigue durability of 40Kh steel in an acidic medium increases with the content of nitrogen and the pressure of a gas mixture.

The studies of the low-cycle durability of structural steels after NGD in an acidic model medium show that it is mainly affected by the nitriding temperature. As the nitriding temperature increases, the low-cycle durability decreases. The number of cycles prior to the fracture decreases more rapidly, as the content of carbon in the matrix and the degree of its doping increase. An increase in the content of nitrogen and in the pressure of a gaseous medium does not influence practically the low-cycle durability of nitrided steels in an acidic medium.

During the nitriding, the focus of cyclic fracture is located usually under the surface nitride layer. Therefore, its composition has practically no influence on the fatigue characteristics of steels. An increase in the resistance to the low-cycle fracture is determined by the strength characteristics of the diffusion layer (γ- and α-phases). The tests for static strength show that NGD of steels increases their strength characteristics (σ_u and σ_y) and decreases simultaneously the plasticity. It is established that the number of cycles prior to the fracture under a low-cycle loading of 40Kh steel in an alkaline solution is even larger than in air. This is explained by the formation of a hydroxide layer blocking the rise of dislocations to the surface. If the amplitude of vibrations $\varepsilon <$ 0.5 %, the difference in the durabilities of nitrided and nonhardened steels under a low-cycle loading is insignificant. For $\varepsilon \geq 2.5$ % for nitrided and $\varepsilon \geq 4$ % for improved specimens, their durabilities in air and in the corrosive medium coincide. In this case, by starting from the deformation amplitude $\varepsilon > 0.25$ %, the use of NGD to increase the low-cycle durability is not efficient. The high-cycle durability is mainly affected by the nitriding temperature: as it increases, the durability of nitrided steels decreases. The fatigue high-cycle durability of nitrided steels increases with the content of nitrogen and the pressure in a gas atmosphere: for example, it is higher for 40Kh steel by at least 35 % in air and by 30 % in an acidic medium.

1.6. Hydrogen nitrogening in great discharge

To date, research continues on the theoretical foundations, improvement of technologies and structures and types of equipment for technological processes of anhydrous nitriding in the glow discharge (BATR) [37]. Widespread use of BATR in industry has led to the exclusion of ammonia from gaseous media and, thus, to a fundamental improvement in the working conditions of equipment and maintenance personnel, environmental friendliness of the process [38]. In turn, this has led to an expansion of the range of performance indicators in accordance with the requirements and conditions of the friction contact load [39, 40]. Much of the research is devoted to methods of providing discharge in fundamentally different hardware implementations of power supplies [40]. In addition to nitriding with a constant power supply from a DC source, installations with additional heating from special screens or thermoradiation heaters are used, which reduces the relationship between electrical parameters of the technological mode and mode factors, especially temperature, because the energy factor is not only glow discharge. The development of new theoretical approaches is based primarily on the basic principles of gas discharge physics [41, 42]. The technological process has become multistage, in which it consists of macro- or microphases, which also significantly affects the results and productivity of the processing process. Fundamentally different nitriding results are achieved due to the introduction of cyclic-switched discharge (CCR), in which compared to the period of time sufficient to extinguish the transition from the glow discharge to the arc, the power supply to the camera electrodes is interrupted. In addition to simplifying control systems in CCR installations, the positioning of parts in the chamber is simplified, as the presence of gaps between parts and equipment for placing parts in the chamber no longer plays such a significant role. However, given the fact that the power supply to the electrodes of the chamber when using alternating current is not all the time, but in a much shorter period, the processing productivity decreases to about the same extent. Voltage and current emissions at the beginning and end of the power cycle are a problem, which can cause local damage to the treated surface [43]. The aim of the research is to analyze the possibilities and conditions for simplifying the design of nitriding installations in the glow discharge, as well as the possibility of using as a power supply electrodes discharge chamber cyclic-switched or alternating current industrial frequency (HF). The structure and functional purpose of the individual components (for example, a three-chamber installation) are shown in Fig. 1.19.

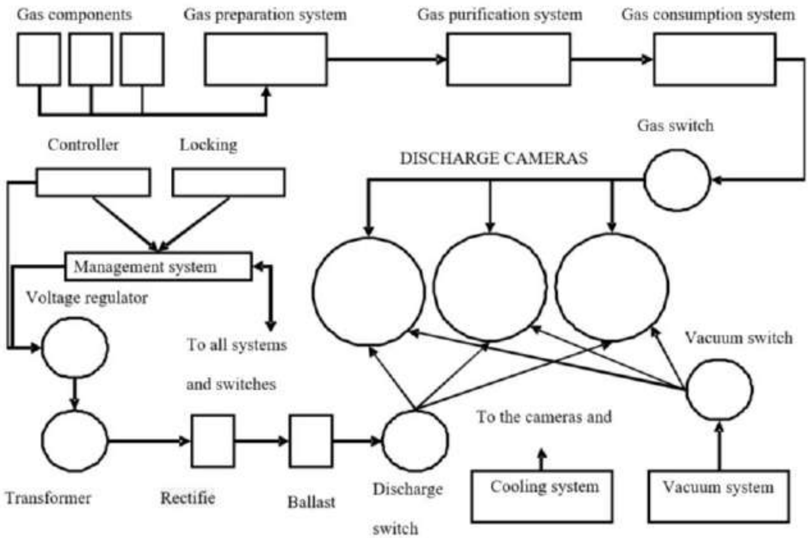

Fig. 1.19. Block diagram of a three-chamber installation

In the installation, when the process is powered by direct current, the power supply must include the following components: voltage regulator (set the voltage at the input to the power supply system); step-up transformer (under the influence of the control signal from the voltage regulator changes the voltage up to values of about 1200 V – at the end of the surface cleaning phase by cathodic bombardment; rectifier that converts alternating current into conditionally constant output voltage includes ripples of greater or lesser magnitude compared to the rated voltage, ballast rheostat for redistribution of electric current at the input of the chamber. With cyclic-switched power supply, there are significant voltage emissions at the beginning and end of the pulse up to values that can cause local surface damage. In addition, perhaps the most important argument, the discharge control system is significantly complicated by the mandatory inclusion of control pulse generators operating at a frequency of 1–5 kHz, as well as CCR significantly reduces the productivity of the modification process [38, 40].

The above-described power structure of nitriding installations in the glow discharge is most suitable for single-phase processes, when the whole technological process takes place at constant technological parameters. However, it should be borne in mind that the main task of the power supply is not to maintain the specified electrical characteristics of the discharge, but to ensure a stable temperature on the surface of machined parts, which primarily affects the formation of a given phase-structural composition of the surface. Prospects for the practical application of anhydrous nitriding in a glow discharge with AC power supply (BATR HRT) are determined taking into account this circumstance as a determinant, because with variable current amplitude, respectively, in the period when the camera electrodes are negative voltage is no longer heated the cathode, which serves as a cage, and the anode or component of the installation, which acts as an anode. It is obvious that with such a design solution it is necessary to ensure reliable insulation of the anode from the housing, because in case of violation of such insulation there will be a real threat of electric shock. In the case of using BATR SPC power supply of electrodes is a single-phase current, the design of the transformer is significantly simplified, and the cost is reduced by at least three times. Similarly, it would be logical to manufacture and apply a single-phase voltage regulator, which in combination with a single-phase transformer will inevitably have a positive impact on the cost of the entire installation. This will reduce depreciation costs, which will also have a positive impact on cost. The lack of a rectifier and a ballast rheostat makes a certain contribution to reducing the cost of installations. From this analysis there is a question of reaching the temperature of the nitrided surface necessary for carrying out the planned technological mode. If this task cannot be performed, additional heaters can be used to ensure the independence of the discharge energy parameters. Thus, it is possible to use technological modes with high discharge voltage or current, which allow to form the necessary under the conditions of subsequent operation of the phase structure of the surface modified layer. The next task of the staging nature is the study of the electrical characteristics of the process, which is associated with the need to establish the magnitude of the ignition voltage of the discharge and its stable combustion in the anomalous mode. It is also necessary to establish analytical or experimental dependences of the parameters of the technological regime, taking into account its energy characteristics and thus establish the limits of energy characteristics necessary for the implementation of the process. The next question is to study the process of formation of a given phase structure in BATR HRC. The essence is that the nitriding process is always a combination of individual subprocesses: the formation of nitrides, surface spraying and diffusion of nitrogen into the depth of the surface layer. With normal nitriding (direct current), an equilibrium is established between the individual subprocesses, usually in favor of nitride formation and diffusion. The process in the conditions of this equilibrium takes place stationary and with different intensity, which depends not only on the energy conditions, but also on the material of nitrided parts. It is known that chromium steels can be nitrided only in gaseous media, where the neutral component predominates. This is because chromium is a nitrogenous material. Already in the initial period of nitriding, a monolayer of nitrogen is formed on the surface, which then acts as a barrier to the penetration of nitrogen into the depth of the surface. Nitriding is almost non-existent and the thickness of the nitride layer is very small. Given the significant relative duration of the half-life of the negative voltage (0.02 s) on the electrodes of the chamber, it is appropriate to hope that under the action of electron flow the nitride monolayer will be destroyed, and in the next half-period when the flow is directed to the cathode (detail) , will promote the intensification of both nitride formation and diffusion of nitrogen into the depth of the surface layer. Therefore, in principle, nitriding in a glow discharge with power supply of industrial frequency is possible. This significantly simplifies and reduces the cost of installation for the process.

Device for increasing the wear resistance of steels by nitriding in ACR with AC. The process of nitriding parts in the glow discharge is mainly carried out using a constant power supply discharge. Thus, when using a discharge with constant power on the outer surface of the part for a relatively short period of time (duration of the nitriding process 4 h), you can get a modified surface with specified properties with high stability of the discharge. The big disadvantage of this process is that parts of complex configuration (with a large number of small holes, with narrow slits, with sharp tops) require proper preparation of these parts for nitriding. All these holes and crevices must be properly closed because they significantly complicate the nitriding process using a constant discharge power supply and can provoke corona and arc discharges, which leads to overheating of the part and in most cases the nitriding process itself becomes impossible. Therefore, one of the options to solve this problem is to use a glow discharge with non-stationary power supply. When using AC industrial frequency, you do not need to create new equipment, but only need to upgrade existing ones. The essence of the modernization is to replace the uninterruptible power supply of the discharge with a source of non-stationary power supply of the discharge with alternating current of a given frequency. Adjusting the switching frequency, or as it is called duty cycle, is the ratio of the cycle period to the signal duration, and the shape of the signal itself makes it possible to influence the results of surface treatment. The influence of the shape and frequency of the discharge power signal on the nitriding process is due to the shutdown of the electric field, which allows to change the flight trajectory of the incident flux particles. That is, the switched off electric field allows the particles to move for some time by inertia along the tangent to their trajectory and allows the particles to penetrate to a much greater depth. And also to influence impossibility of transition of a glowing category in an arc. The use of cyclically switched AC power discharge makes it possible to nitriding parts with slits, with small diameter holes without the use of special equipment and you can not be afraid of corona and arc discharges. As a disadvantage, it should be noted that the nitriding process itself increases at least two or more times. The device for nitriding in a glow discharge with a direct current consists of a power supply to the chamber which contains a thyristor voltage regulator, a rectifier, a transformer, current and voltage sensors, a ballast rheostat, an automatic shut-off unit. The disadvantage of this device is its complexity and significant energy losses on the current converter, the need to use special filters to smooth the current. The work is based on the task of creating a device for nitriding in the glow discharge with AC power, which provides the opportunity to significantly simplify the equipment and, accordingly, reduce its cost. The problem is solved by the fact that the device for nitriding in the glow discharge introduced a source with non-stationary power supply with alternating current of a given frequency [44]. The purpose of the proposed device is primarily to significantly simplify the design of the installation for nitriding in the glow discharge and increase its reliability, as well as to reduce the cost of equipment, which is solved by replacing a constant discharge power supply with non-stationary AC power supply. This increases the reliability of the installation, and also due to a significant reduction in electricity losses reduces the cost of processing nitrided parts. The use of alternating current also affects the course and results of nitriding, as periodic changes in the polarity of the electrodes of the chamber contributes to the cleaning of the surface from the adsorption layer, which in turn leads to a significant change in phase composition of the surface modified layer [9]. The possibility of using the claimed device for conducting BATR on the existing industrial installation was experimentally tested. At the same time, the need for electricity significantly decreased due to the absence of losses for rectification, which also led to a reduction in the cost of processing. Analysis of the results of metallographic studies of the modified layer indicated the presence of a more uniform gradient of hardness in depth (gradient decreased by 1.7–3.5 times), which, in turn, increases the wear resistance of parts and quality performance of parts (Ukrainian patent № 118327).

Method of nitriding in ACR with AC power supply. The most common method of BATR surface in which the part throughout the process serves as a cathode powered by a DC source. The disadvantage of this method is that its implementation is possible in the presence of an adjustable DC source, as well as special control devices. The problem of developing a method of nitriding in a glow discharge with AC power, which would simplify the process power supply, is solved by powering the process from an AC power source, the voltage should vary depending on the parameters of the technological mode of surface modification. The essence of the proposed idea is that the part and body of the camera or its special shell, which serve as electrodes, receive power of different polarity, and parts of the cage and the body of the camera or its special part, which acts as electrodes, are powered by AC power source , and the voltage varies depending on the parameters of the technological mode of modification of the surface of the parts. Unlike traditional incandescent nitriding methods, in which the part is always the cathode and the chamber shell or its special part serves as the anode, there is a constant threat of the incandescent discharge in the arc, which also complicates the process because the part is damaged locally or the entire surface. In addition, it is impossible to obtain a stable constant supply of the electrodes of the discharge chamber, ie to some extent the process takes place when supplied with non-constant current, although stable polarity. The experiments performed on the existing industrial plant indicate the possibility of implementing the claimed method of nitriding in a glow discharge with AC power supply of industrial frequency. If necessary, the frequency of the current can be easily changed using a simple frequency converter using an electromechanical device. In this case, the process of regulating the parameters of the technological process is significantly simplified, the reliability of technology implementation is increased, which has a positive effect on the cost of processing metal parts [46]. The idea of using industrial frequency AC as a power source for BATR, the possibility of switching the shape of pulses, changing their polarity has led to the development of a number of developments in methods and technologies of nitriding [46, 47].

At BATR in CCR with supply of current of industrial frequency the installation for realization of process becomes cheaper. The latter factor will contribute, among other aspects, to the wider introduction of BATR technologies.

The use of alternating current affects the course and results of nitriding, as periodic changes in the polarity of the electrodes of the chamber contributes to the cleaning of the surface from the adsorption layer, which positively affects the nature of nitrogen saturation (gradient of microhardness times), contributes to a significant change in the phase composition of the surface modified layer and allows to expand the technological capabilities of nitriding in the direction of obtaining the required performance characteristics of working surfaces, in particular tribological characteristics.

References for Chapter 1

1. Pastukh, I. M. Theory and Practice of Hydrogen-Free Nitriding in Glow Discharge [in Russian]. Khar'kov Physicotechnical Institute. Ukrainian National Academy of Sciences. Kharkov (2006).

2. Semenov, M. Y., Kai, J. D., Smirnov, A. E. et al. Use of Glow Discharge Nitriding for Raising the Surface Hardness of Bearing Parts from Precision Nickel Alloys. Met Sci Heat Treat 61, 173–177 (2019). https://doi.org/10.1007/s11041-019-00396-0.

3. Wehner, G. Advances in Electronics and Electron Physics (Academic, New York, 1955), Vol. 7, p. 239.

4. Alonso, J. A. and March, N. H. Electrons in Metals and Alloys. Academic Press. London (1989).

5. Kindrachuk, M. V., Stechyshyn, M. S., Mykhailiv, N. P. Influence of the preliminary ion-plasma hydrogenation on the tribological properties of ion-nitrided surfaces. In: Problems of Friction and Wear [in Ukrainian], NAU-Druk. Kiev (2009). Issue 50. Pp. 180–189.

6. Stechyshyn, M. S. Durability of Parts of the Equipment for Food Industry under the Conditions of Stress-Corrosion Wear [in Ukrainian]. Doctoral Degree Thesis (Engineering). Khmel’nyts’kyi (1998).

7. Shevelya, V. V., Oleksandrenko,V. P. Tribochemistry and Rheology of Wear Resistance [in Russian]. Khmel’nyts’kyi National Univ. Khmel’nyts’kyi (2006).

8. Pastukh, I. M. Energy model of glow discharge nitriding. Tech. Phys. 61, 76–83 (2016). https://doi.org/10.1134/S1063784216010151

9. Wielage, B. Arc-sprayed iron-based coatings for erosion-corrosion protection of boiler tubes at elevated temperatures. J. Therm. Spray Technol., 22. No. 5. Pp. 808–819.

10. Student, O. Z., Svirs’ka, L. M. & Dzioba, I. R. Influence of the long-term operation of 12Kh1M1F steel from different zones of a bend of steam pipeline of a thermal power plant on its mechanical characteristics. Mater Sci 48 (2012). Pp. 239–246.

11. Rudyk, O., Kaplun, P., Golenko, K., Honchar, V., & Poberezhnyi, M. (2022). Investigation of corrosion and wear resistance of steels nitrided in a glow discharge in distilled water. Problems of Tribology, 27 (3/105). Pp.61–69.

12. Lei,M. K., Zhang, Z. L. Plasma source ion nitriding: A new low temperature, lowpressure nitriding approach. Journal of Vacuum Science & Technology A 1 November 1995; 13 (6): Pp. 2986–2990. https://doi.org/10.1116/1.579625.

13. Shahin, M. M.,Advances in Chemistry Series No. 58 (American Chemical Society, Washington, D.C. (1966). Pp. 315.

14. Babei, Yu. I., Sopronyuk, N. G. Protection of Steels Against Stress Corrosion Fracture [in Russian]. Tekhnika, Kiev (1981).

15. Avner Brokman, Floyd R. Tuler; A study of the mechanisms of ion nitriding by the application of a magnetic field. Journal of Applied Physics 1 January 1981; 52 (1): 468–471. https://doi.org/10.1063/1.329809

16. Kenan Genel, Mehmet Demirkol, Mehmet Çapa, Effect of ion nitriding on fatigue behaviour of AISI 4140 steel, Materials Science and Engineering: A, Vol. 279, Issues 1–2 (2000). Pp. 207–216.

17. Stechyshyn, M.S., Martynyuk, A.V., Bilyk, Y.M. et al. Influence of the Ionic Nitriding of Steels in Glow Discharge on the Structure and Properties of the Coatings. Mater Sci 53 (2017). Pp. 343–350.

18. Stechyshyn, M. S., Sokolova, H. M., Bilyk, Yu. M. Influence of energy and mode parameters on the phase structure and microhardness of ion-nitrided structural steels. Probl. Tertya Znoshuv., No. 2, 56–64 (2017).

19. Student, M. M., Dovhunyk, V. M., Klapkiv, M. D. et al. Tribological Properties of Combined Metal-Oxide–Ceramic Layers on Light Alloys. Mater Sci 48, 180–190 (2012).

20. Samsonov, G. V. Nitrides [in Russian]. Naukova Dumka, Kiev (1969).

21. Ozbaysal, K., Inal, O. T. Structure and properties of ion-nitrided stainless steels. J Mater Sci 21 (1986). Pp. 4318–4326.

22. Kenan Genel, Mehmet Demirkol, Mehmet Çapa, Effect of ion nitriding on fatigue behaviour of AISI 4140 steel,Materials Science and Engineering: A, Vol. 279, Issues 1–2 (2000). Pp. 207-216. https://doi.org/10.1016/S0921-5093(99)00689-9.

23. Stechyshyn, M., Lyukhovets, V., Stechyshyn, N., & Tsepenyuk, M. (2022). Wear resistance of structural steels nitroded in cyclic-commuted discharge at limit modes of friction. Problems of Tribology, 27 (3/105). Pp. 27–33.

24. Kaplun, V. G., Kaplun, P. V. Ionic Nitriding in Hydrogen-Free Media [in Russian]. Khmel'nitskii National University. Khmel'nitskii (2015).

25. Stechyshyn, M. S., Skyba, M. E., Sukhenko, Y. G. et al. Fatigue Strength of Nitrided Steels in Corrosion-Active Media of the Food Enterprises. Mater Sci 55, 136–141 (2019). https://doi.org/10.1007/s11003-019-00261-8.

26. Chumalo, H.V. Influence of Hydrogen Sulfide on the Corrosion-Mechanical Properties of Welded Joints of Pipe Steel. Mater Sci 48 (2012). Pp. 176–179.

27. Stechyshyn, M. S., Stechyshyna, N. M. & Kurskoi, V. S. Corrosion and Electrochemical Characteristics of the Metal Surfaces (Nitrided in Glow Discharge) in Model Acid Media. Mater Sci 53 (2018). Pp. 724–731.

28. Yokobori, T. An Interdisciplinary Approach to Fracture and Strength of Solids, Noordhoff, Groningen (1968).

29. Polyakov, B. Z., Babushkin, V. V. Residual stresses in borated steels. In: Proc. of the All-Union Conf. "Thermochemical Treatment of Metals and Alloys", MPI, (1971). Pp. 121–125.

30. Samsonov, G. V. Nitrides [in Russian]. Naukova Dumka. Kiev (1968).

31. Stechyshyn, M. S., Stechyshyna, N. M., Martynyuk, A. V. Cavitation-Erosion Wear Resistance of Details of the Equipment of Milk Plants [in Ukrainian]. KhmNU. Khmel'nyts'kyi (2018).

32. Mashovets, N. S., Pastukh, I. M., Voloshko, S. M. Aspects of the practical application of titanium alloys after low temperature nitriding glow discharge in hydrogen-free-gas media, Applied Surface Science. Vol. 392 (2017). Pp. 356–361. https://doi.org/10.1016/j.apsusc.2016.08.180.

33. Stechyshyn, M. S., Sokolova, G. M., Bilyk, Yu. M. Influence of power and mode parameters on the phase structure and microhardness of ionnitrided structural steels. Probl. Tertya Znosh., No. 2 (2017). Pp. 56–64.

34. Tkachev, V. I., Babei, Yu. I. Machine IP-2 for the testing of metals for low-cycle fatigue in liquid media. Fiz.-Khim. Mekh. Mater., 1, No. 2 (1966). Pp. 228–229.

35. Prokopenko, A. V., Torgov, V. N. A method of testing of compressor blades of a gas turbine engine for fatigue in the corrosion medium. Probl. Prochn., No. 4 (1980). Pp. 107–109.

36. Stechyshyn, M. S., Skyba, M. E., Student, M. M. et al. Residual Stresses in Layers of Structural Steels Nitrided in Glow Discharge. Mater Sci 54 (2018). Pp. 395–399. https://doi.org/10.1007/s11003-018-0197-9.

37. Michel, H., Czerwiec, T., Gantois, M., Ablitzer, D., & Ricard, A. (1995). Progress in the analysis of the mechanisms of ion nitriding. Surface and Coatings Technology, 72 (1–2). Pp. 103–111.

38. Pastukh, I. M. Subprocesses accompanying nitriding in a glow discharge. Tech. Phys. 59. (2014). Pp. 1320–1325. https://doi.org/10.1134/S1063784214090205.

39. Skyba, M. E., Stechyshyna, N. M., Lyukhovets, V. V. and others. Hydrogen nitriding in a glow discharge as a method of increasing the wear resistance of structural steels. Bulletin of Khmelnytsky National University. Technical Sciences, 2019. № 5. P. 7–12.

40. Pastukh, I. M, Lyukhovets, V. V., Kurskoy, V. S. Features of nitriding in a glow discharge with non-stationary power supply of holes with relatively small diameter. Bulletin of Khmelnytsky National University. Technical sciences. 2013. № 3. Pp. 195–198.

41. Huang, W. H., Chen, K. C., & He, J. L. (2002). A study on the cavitation resistance of ion-nitrided steel. Wear, 252 (5–6). Pp. 459–466.

42. Jindal, P. C. (1978). Ion nitriding of steels (Doctoral dissertation, American Vacuum Society).

43. Stechishina, N., Stechishin, M., Martynyuk, A., Lukianyuk, N., Lyukhovets, V., & Bilyk, Y. (2021). Influence of the parameters of hydrogen

nitrogen nitrogen in a glow discharge on tribological and physico-chemical properties of steel 40X. Problems of Tribology, 26 (3/101). Pp. 31–41.

44. Stechyshyna, N., Stechyshyn, M., Martynyuk, A., & Gladkiy, Y. (2021). Hydrogen nitrogening in great discharge with AC power. Problems of Tribology, 26 (4/102). Pp. 6–11.

45. Device for nitriding in a glow discharge with AC power supply / I. M. Pastukh, G. M. Sokolova, V. V. Lyukhovets, O. S. Zdibel: Pat. on the utility model № 118327 Ukraine: IPC C 23 C 8/36, C 23 C 8/48. № in 2016 06460 ; stated 13.06.2016 ; publ. 10.08.2017, Bull. № 15.

46. Stechyshyn, M. S., Skyba, M. E., Stechyshyna, N. M. et al. Physicochemical Properties of the Surface Layers of 40Kh Steel After Hydrogen-Free Nitriding in Glow Discharge. Mater Sci 55. Pp. 892–898 (2020).

47. Pastukh, I. M., Sokolova, G. M., Lyukhovets, V. V., Zdibel,O. S. : Pat. for utility model № 112983 Ukraine: IPC C 23 C 8/36, C 23 C 8/48. № in 2016 05929 ; stated 01.06.2016 ; publ. 10.01.2017, Bull. № 1.

48. Pastukh, I. M., Sokolova, G. M., Lyukhovets, V. V., Zdibel O. S. Method of nitriding in a glow discharge with AC power supply : Pat. for utility model № 112983 Ukraine: IPC C 23 C 8/36, C 23 C 8/48. № in 2016 05929 ; stated 01.06.2016 ; publ. 10.01.2017, Bull. № 1.

Chapter 2.
INFLUENCE OF THE ENERGY PARAMETERS OF NITRIDATION ON THE PHYSICO-CHEMICAL AND TRIBOLOGICAL CHARACTERISTICS OF STRUCTURAL STEEL

2.1. The influence of the specific power of the energy discharge

A special attention within solving the problem of increasing the reliability and durability of machines and equipment is paid to the issue of friction and wear, because 85–90 % of machines fail due to surface wear of separate parts and units. In the field of machine building money expenditures which refer to friction and wear reach 8 % of national income. Meanwhile, according to research data from one-quarter to one-third of all energy produced in the world during per year is currently spent on overcoming the frictional forces in movable joints of machines.

Recently in order to increase wear resistance of parts and units the preference is given to the application of controlled surface modification techniques based on the impact of concentrated flows of energy and substances on metal surfaces, i.e. vacuum, ion and laser technologies. Among them one of the most developed and widely used is the method of glow discharge nitriding (GDN) [1–3], and in particular, the method of hydrogen-free nitriding in glow discharge (HFNGD) [4–6]. By retaining all the main advantages of nitriding in hydrogen-containing environments (ammonia, mixed nitrogen and hydrogen), HFNGD increases the plastic properties of the surface layer owing to eliminating hydrogen-caused embrittlement, reduces energy and material consumption, improves working conditions (excluding the possibility of an explosion of a hydrogen mixture). Moreover, HFNGD is an environmentally appropriate technology.

It should also be noted that the influence of the GDN operating conditions has been extensively studied [7–11], whereas the energy parameters (specific density of the energy flow, voltage and current density in a gas-discharge chamber) were practically not considered. We cannot ignore the inherent energy parameters of the glow discharge which acts as an identifier of primary sub-processes (nitrides formation, dispersion and diffusion saturation of the surface with nitrogen) that deal with the formation of the nitrided layer, its structure and phase composition. Essentially, doing this means losing unique capabilities of management and control of surface modification processes. The study of the tribological properties of modified friction surfaces [12–14] makes it possible to substantiate and optimize the technological parameters of nitriding in a glow discharge. Thus, the aim of this work is to study the influence of energy parameters of HFNGD process on the phase composition, the thickness of nitrided and diffusion zones and tribological properties of structural steels.

Research methodology. HFNGD was conducted on the diode-type installation UATR-1(Ukraine), which operates at direct current in hydrogen-free gas environments (nitrogen and argon). The unit is additionally equipped with heating elements located in a gas-discharge chamber, which makes it possible, given the preset temperature of the parts (samples) surface, to change the voltage value in the chamber in an arbitrary way. The following parameters of HFNGD were assumed based on the experience of experimental and industrial practices and in order to optimize the number of experiments: temperature T = 833 ºK, nitriding time – 4 hours, mixed gas composition is 80 % N_2 + 20 % Ar. An arbitrary value of voltage was chosen, and current density ($j = I/S$, where I is current, A; S is the surface area of the cathode, which is equal to the sum of the suspension and samples areas, m^2) was determined by a combination of the arbitrarily assigned voltage and pressure of the mixed gas. The specific capacitance of electric discharge in a gas-discharge chamber was determined by the formula $W = UI/S$, kW/m^2. The values of HFNGD parameters are shown in Table 2.1.

Table 2.1

HFNGD operations with independent parameters

Operation	1*	2	3	4*	5	6	7*	8	9
Pressure P, Pa	53.2			106.4			159.6		
Voltage U, V	1100	820	515	840	515	300	700	515	300
Current density j, A/m^2	11.0	7.2	3.2	13.2	7.2	2.8	15.8	12.8	7.2
Specific capacitance W, kW/m^2	12.2	5.9	1.65	11.1	3.71	0.84	11.1	6.59	2.2

*Operations conducted with dependent parameters of nitriding (without additional heating of the samples).

Structural steels of C45, 37Cr4 and 41CrMoAl7 were examined. Identification of the elemental composition of these steels was performed on an energy dispersive X-ray fluorescence spectrometer "Sprut" with SDD detector X-123 (Amptek, the USA). Steels grades identification was conducted by determining eight chemical elements (C, Al, Si, P, S, Ti, Cr, Mn). Chemical composition control has shown that the samples tested meet current standards. The microhardness of the surface was measured with the DuraScan-70 microhardness tester. In order to detect the structure of the nitrided layer steels etching was carried out in a 3 % alcoholic solution of nitric acid (HNO_3). The thickness of the nitride zone was measured with the help of Leica DMi8 metallographic microscope. X-ray diffraction analysis was performed on the DRON-3 diffractometer in the filtered radiation of an iron anode at an angle ranging from 20° to 100° with a scan step of 0.1 and an exposure time of 10 s. Investigation of samples for wear resistance in dry friction conditions was carried out on 2168UMT universal machine. Special holder-adapters were manufactured in order to secure cylindrical specimens ($d \times l = 5 \times 20$ mm) and to ensure contact all over the surface of the sample end face (Fig. 2.1). Spherical hinge 4 provides sample self-adjustment on the counterface.

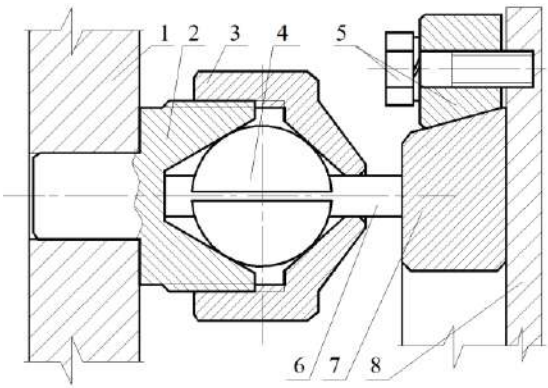

Fig. 2.1. Design of securing device for tested samples:
***1* – support, *2* – seat, *3* – nut, *4* – spherical hinge, *5* – counterface holder, *6* – sample, *7* – counterface, *8* – faceplate**

A hole with a diameter equal to the diameter of the sample is drilled is made in the sphere of the hinge. The sphere itself is divided into two equal parts. The arrangement (seat *2*, spherical hinge *4* and sample *6*) is held with a nut *3*. This way the friction pattern is applied – the chuck plate and the type of contact – interfacial slip (the face end of the cylindrical specimen slips along a flat metal disk) and the vector of relative velocity in this direction is tangent to the surface contact area. The material of the counterface is a 52100 steel with surface hardness of HRC61, pressure in a frictional contact area is 16 MPa, a rubbing speed of 0.1 m/s, the controlled parameter – linear deterioration of a sample size after it passes the accepted value of rubbing distance. As the rubbing distance changes, so the empirical data measurement interval alters (Table 2.2).

Table 2.2

Empirical data measurement time interval

Rubbing distance L, m	0–50	50–200	200–400	400–1000	Over 1000
Measurement interval l, m	5	10	25	50	100

Research results and discussion. Correlation between wear resistance of HFNGD modified surfaces and nitriding conditions was confirmed by tribological tests. Thus, in conditions of dry friction, when dealing with the surfaces modified at higher values of specific capacitance of energy flow W, the wear rate $I_h = \Delta i/L$ (slope of a curve to the abscissa axis) during the periods of wear-in and constant wear decreases (Fig. 2.2).

Fig. 2.2, *a* shows the wear area of the nitrided steel of C45 grade: I – wear-in area; II – steady wear area and III – catastrophic wear area. At the same time the location of curves *6*, *9*, *3* on wear and wear-in graphs (Fig. 2,2 *a* and *b*) corresponds to the smallest values of the specific density of the energy discharge W = 0.84; 2.12 and 1.65 kW/m^2 respectively (Table 2.1).

For alloy steels, the location order of the wear curves *9*, *6*, *3* corresponds to the minimum values of the specific density of the energy discharge, respectively, W = 2 W = 2.2; 0.84 and 1.65 kW/m^2 (steels 37Cr4 and 41CrAlMo7). Thus, operations *6*, *3* and *9* for carbon steel (C45 steel) and for alloyed steels showed the worst results in wear resistance compared to other operating conditions being applied in tests. And if the maximum extent of the steadt wear area for C45 and 37Cr4 steels is ranging from 650 to 1000 m (operation 1 and 7) then for high-alloy steel 41CrAlMo7 varying from approximately 1500 (operation *1* and *7*) to 2000 m (operation *4*).

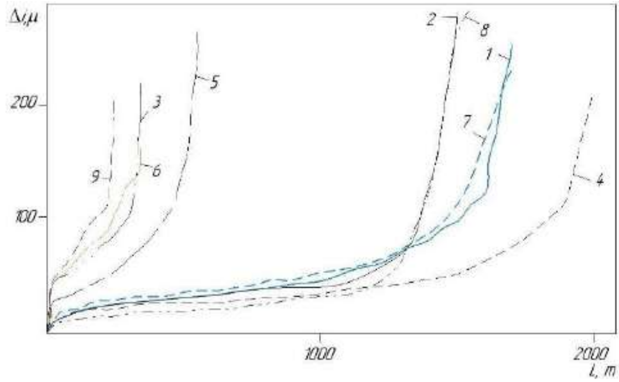
Δi,μ
200
100
1000
2000
l, m
1
2
3
4
5
6
7
8
9

a

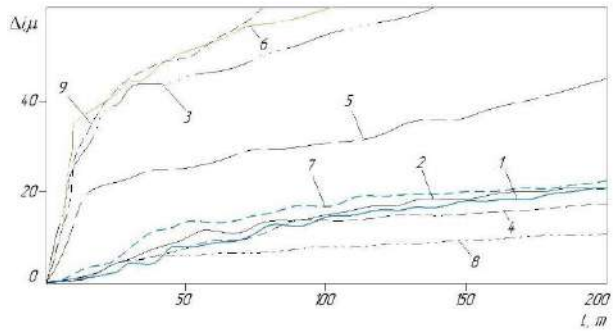
Δi,μ
40
20
0
50
100
150
200
l, m
1
2
3
4
5
6
7
8
9

b

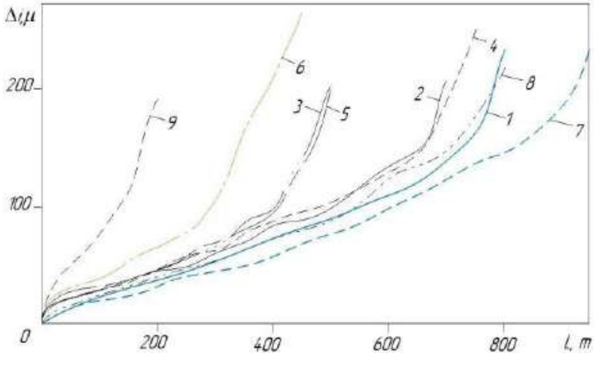
Δi,μ
200
100
0
200
400
600
800
l, m
1
2
3
4
5
6
7
8
9

c

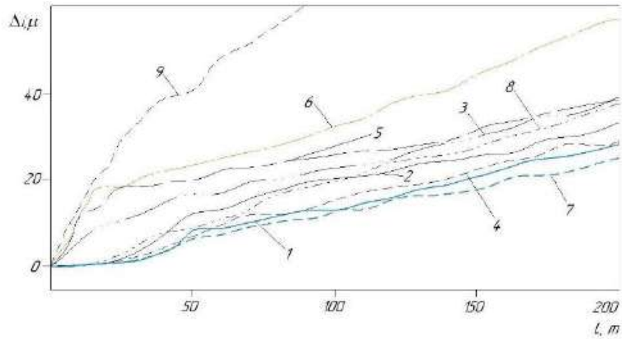

d

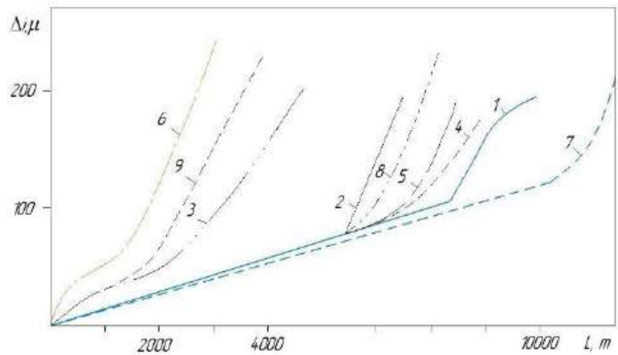

e

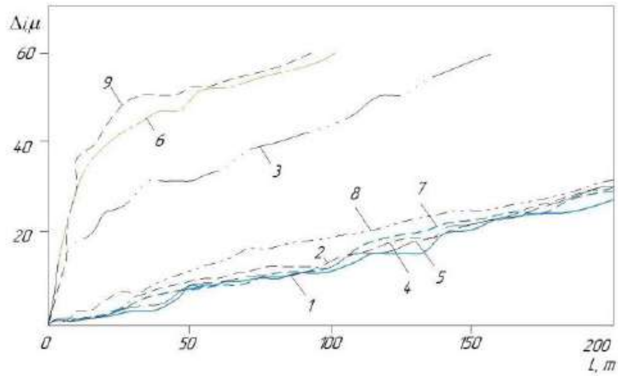

f

Fig. 2.2. Curves of wear (*a, b, c*) and wear-in (*d, e, f*) of nitrided steels: *a, d* – C45 steel; *b, e* – 37Cr4 steel, *c, f* – 41CrAlMo7 steel (digits on the curves correspond to HFNGD operations which are shown in Table 2.2)

The above-noted indicated operations of HFNGD are characterized by the largest values of $W = 12.2$ kW/m^2 (operation 1) and $W = 11.1$ kW/m^2 (operation 4 and 7). Consequently, the value of the specific capacitance of the energy flow in the gas-discharge chamber significantly affects the tribological properties of the steels. Obviously, this effect is manifested through the formation of the relevant structure and phase composition of the nitrided layers in the steels under investigation, which determines their physical-and-chemical as well as tribological properties.

In this study [4] the energy parameters of HFNGD are called "the most important factors of controlling diffusion saturation in glow discharge conditions". In this context the authors of this research suggest using the glow discharge specific capacitance W as an energy criterion.

The study of W in reference to the thickness of the diffusion layer h and the nitrided layer h_N along with the surface microhardness HV_{01} is intimately interrelated. An increase in W leads to an increase of the specified values of h, h_N and HV_{01} (Fig. 2.3).

The largest thickness of the modified (diffusion) layer is obtained on C45 carbon steel, and on the alloyed steels it is smaller. On the other hand, the thickness of the nitrided layer increases along with the increase in matrix doping level and is characterized by the greatest values for 41CrAlMo7 steel. Similarly, the value of surface microhardness varies. The worst results are obtained for operations *3*, *6* and *9*, in which there is no nitrided layer in general, and the surface microhardness is close to the microhardness of the base. Whereas for operations *3* $W = 1.65$ kW/m^2 and *6* $W = 0.84$ kW/m^2, the diffusion layer on is common for C45 and 41CrAlMo7 steels, except for 37Cr4 steel (mode *6*), then for mode *9* with the higher specific capacitance $W = 2.2$ kW/m^2 the absence of the nitrided layer totally requires a separate explanation. It is known [4, 5] that at the HFNGD process involves such basic concurrent competing, mutually complementary and exclusive sub-processes: the formation of nitrides, the spraying and diffusion saturation of the surface with nitrogen.

The energy operating conditions of the primary sub-processes behaviour differ significantly: for example, the formation of nitrides occurs at low values of the specific capacitance of energy flow, and the process of surface spraying becomes more intense at high voltage values.

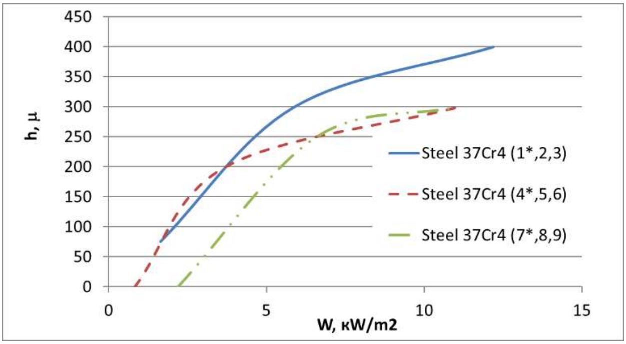

450
400
350
300
250
200
150
100
50
0
h, μ
0
5
10
15
W, кW/m2
Steel 37Cr4 (1*,2,3)
Steel 37Cr4 (4*,5,6)
Steel 37Cr4 (7*,8,9)

a

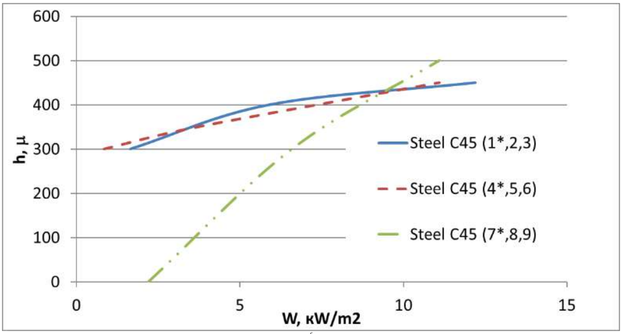

600
500
400
300
200
100
0
h, μ
0
5
10
15
W, кW/m2
Steel C45 (1*,2,3)
Steel C45 (4*,5,6)
Steel C45 (7*,8,9)

b

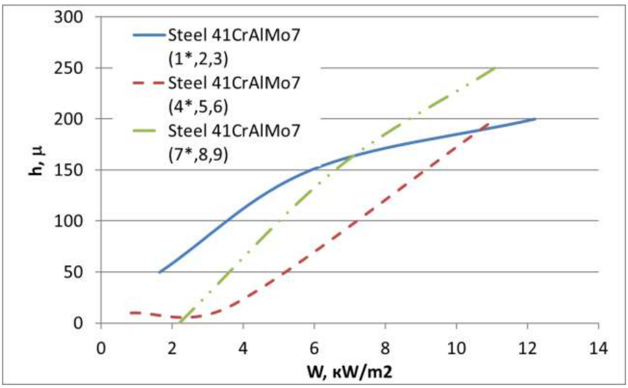

300
250
200
150
100
50
0
h, μ
0
2
4
6
8
10
12
14
W, кW/m2
Steel 41CrAlMo7 (1*,2,3)
Steel 41CrAlMo7 (4*,5,6)
Steel 41CrAlMo7 (7*,8,9)

c

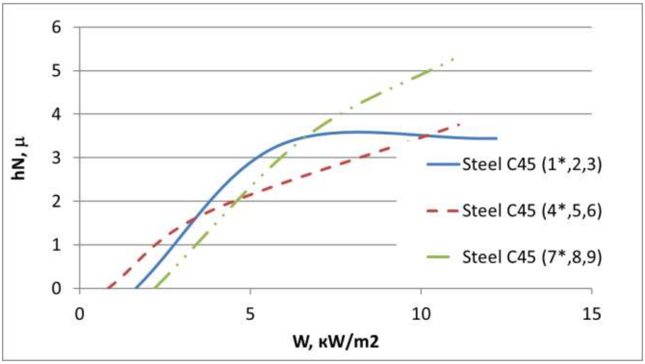
6
5
4
3
2
1
0
hN, µ
0
5
10
15
W, кW/m2
Steel C45 (1*,2,3)
Steel C45 (4*,5,6)
Steel C45 (7*,8,9)

d

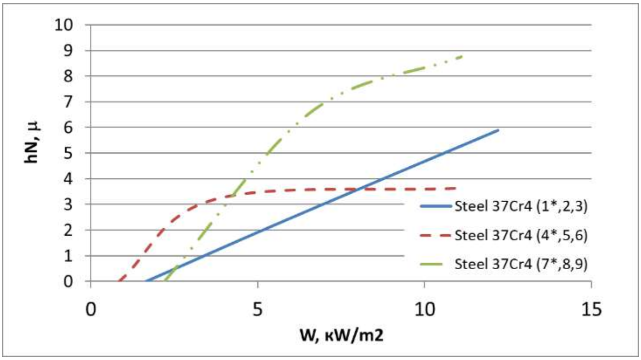
10
9
8
7
6
5
4
3
2
1
0
hN, µ
0
5
10
15
W, кW/m2
Steel 37Cr4 (1*,2,3)
Steel 37Cr4 (4*,5,6)
Steel 37Cr4 (7*,8,9)

e

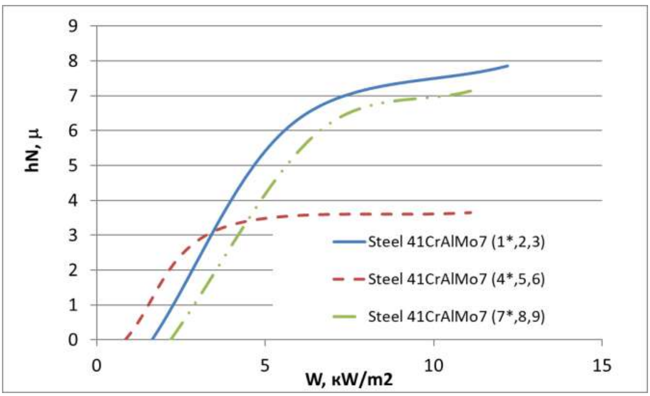
9
8
7
6
5
4
3
2
1
0
hN, µ
0
5
10
15
W, кW/m2
Steel 41CrAlMo7 (1*,2,3)
Steel 41CrAlMo7 (4*,5,6)
Steel 41CrAlMo7 (7*,8,9)

f

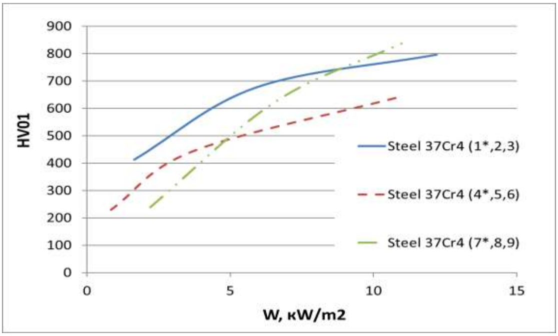

g

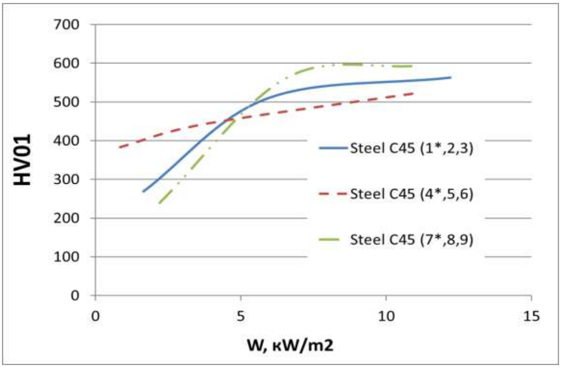

h

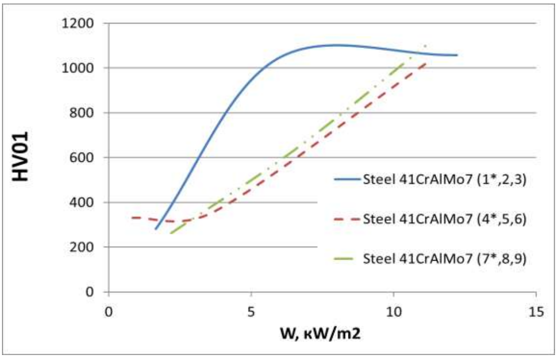

i

Fig. 2.3. Dependency of change in:
***a, b, c* – thickness *h* of diffusion layer; *d, e, f* – thickness h_N of nitrided layer;**
***g, h, i* – surface microhardness on *w* steels after HFNGD**

Since operation *9* has the lowest voltage U = 300 V, obviously, the spraying process does not occur and there is no nitrogen diffusion depthward the metal surface. The latter is convincingly confirmed by the metallographic analysis of etched microslices of 37Cr4 steel (Fig. 2.4).

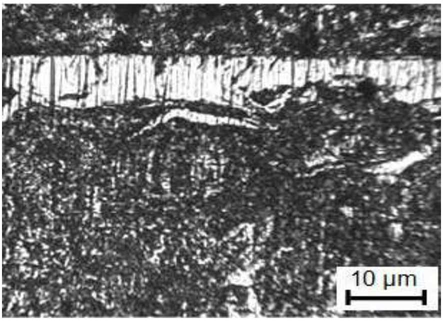

a

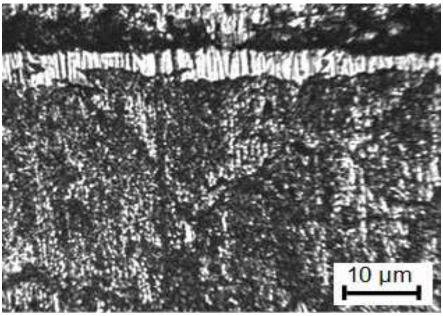

b

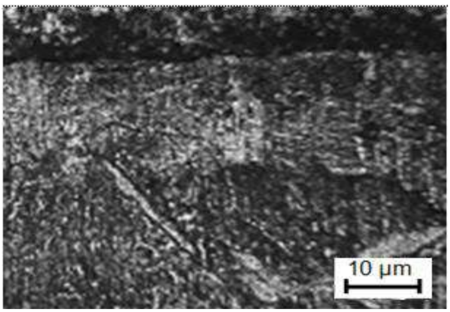

c

Fig. 2.4. Microslices of nitrided 37Cr steel (light layer – nitrided zone):
a* – operation *7*; *b* – operation – *8*; *c* – operation *9

It is evident from Fig. 2.4 that the nitrided zone is not formed on steels in operation *9* of HFNGD; the microhardness measurement data also confirms this point. The microhardness on the surface was HV01 = 238, and at a distance of 200…1000 micron HV01 = 243…240.

The decoding of the diffractogram of the sample of 37Cr4 steel which was nitrated in operating conditions *9* also showed the absence of the γ- and ε-phases.

In addition, operation *9* is realized at maximum pressure $P = P_3$= 159.6 Pa (Table 2.2), which resulted in the absence of glow discharge during nitration process.

Operations *3* and *6*, despite the insufficient W values, progress at lower pressure values of the mixed gas, and therefore the sub-process of dispersion takes place, but there is no subsequent diffusion of nitrogen atoms.

An increase in the content of alloying elements, especially active nitrogen elements, such as chromium, leads to the formation of nitrides, which inhibit the process of nitrogen diffusion depthward the metal base surface and thus prevent the formation of diffusion layers (37Cr4 steel, operation *6*).

The intensity ratio of under which the primary sub processes of HFNGD take place is determined by the structure and phase composition of the nitrided layers. Depending on the current combination of the operational parameters of the formation of the nitrided layer, the intensity of the course of the above sub-processes, and hence the intensity of the formation of these or other phases may be different, and sometimes inverse. For example, when the energy of the incident flow W is increased, the pre-formed nitrided layer is dispersed, which stimulates the process of nitrogen diffusion into the stratum of the metal base and the formation of γ- and ε-phases. In the case when the flow energy is not sufficient to disperse the nitrided layer, it acts as a kind of barrier that prevents or completely stops the process of nitrogen diffusion. The latter factor also gives reasons for the low rates of h, h_N and HV01, as well as low tribological rates obtained from test procedures under *3*, *6* and *9* operation conditions.

In [6] it is argued that there is an extreme dependency between the specific capacitance of the glow discharge W, which is called the criterion of the bearing capacity of the gas medium and its total pressure. The authors of the study argue that the pressure of the gas medium, which corresponds to the maximum specific discharge capacitance, ensures that the nitrided layer obtained is of the largest thickness values under the given conditions.

Our research findings (Fig. 2.5) showed no such dependence. On the contrary, as the pressure P of the mixed gas increases, so *W* decreases (curves I and II in Fig. 2.4), and having independent nitriding parameters (without chamber heating), the dependence of *W* on the pressure is of a completely different varieties. When $U = \text{const}$ (operations *3*, *5* and *8*, Table 2.1), as the pressure in the gas-discharge chamber increases, the current density *j* also increases and, conversely, when j = const (operations *2*, *5* and *9*, Table 2.1), the increase in pressure of the mixed gas leads to a decrease in voltage. Similar dependency relations in thermo stabilization operations are inferred in the study [3].

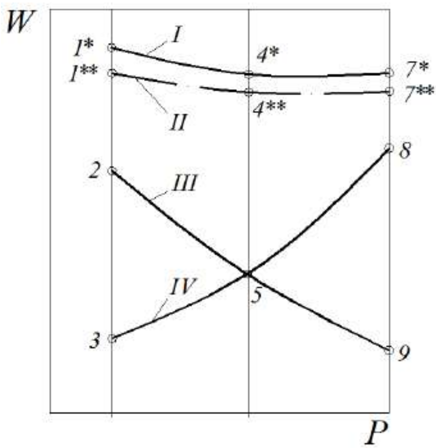

Fig. 2.5. Dependence of specific discharge capacitance *W* on the mixed gas pressure: I, II – without additional heating; III, IV – in unattended conditions (with additional heating of the chamber)

The latter confirms that even in those studies where energy parameters are examined there is not enough concrete data to draw clear conclusions about their influence on the physical and chemical characteristics of the nitrided layer. Thus, the outcome of the study [7] on the modertae energy of ions with voltage and pressure do not allow to consider them as the basis for establishing the corresponding principles due to the unavailability of the composition of the mixed gas, as well as the way of changing the voltage, provided that the constant values of temperature and pressure are maintained. The same applies to the outcome presented in [8, 9], where the effect of current density on the thickness of the nitrided layer was investigated. According to [9], increasing the current density leads to an increase in the thickness of the nitrided layer, and according to [8] – to its decrease.

The analysis of the influence of the HFNGD parameters on the results of nitriding indicates their interdependence. Thus, the composition of the mixed gas and its pressure affects the voltage of the glow discharge, and the change in voltage and current density determines the temperature of saturation and the pressure of the gas medium [4].

It is obvious that while ensuring the independence of the energy parameters of HFNGD opens additional opportunities for both the intensification of the process and for managing the processes of forming the required physical and chemical characteristics of nitrided layers that meet the requirements for machine parts and units operation. In this case, the inhibition or, conversely, the intensification of certain sub processes and the formation of different structures of the modified layer may be possible.

Thus, the study of the influence of HFNGD energy parameters on the results of this process is an important scientific issue, which opens up new possibilities in terms of optimization of nitriding operations, which provide results of modification of metal surfaces that best meet the requirements for operation of parts.

In this way, we can draw conclusions:

1. Regulation of HFNGD process can be carried out by changing the operation conditions (temperature, mixed gas composition, its pressure and time of nitriding) and energy parameters (specific capacitance of the energy flow, current density and voltage on the electrodes of the gas-discharge chamber). The influence of operating parameters on their structure and phase composition and physical and chemical properties of nitrided layers of was the topic of quite comprehensive research, unlike the influence of energy parameters, which is investigated only on the reference level.

2. It has been proved that the decrease of the specific capacitance of discharge leads to a decrease in the thickness of the nitrided and diffusion zones, and the tribological properties deteriorate. It has been consolidated that at the maximum values of energy parameters a nitrided layer containing and ε- , γ- and α-phases is formed. Reducing the voltage and current density leads to an increase in the particle γ-phase (Fe_4N)

and in accordance with the reduction of the particle ε-phase (Fe_2N). At minimal values of energy parameters, the formation of nitrides on the surface is unavailable and the nitrided layer consists only of α-phase.

3. It has been found that in the conditions of dry friction surfaces that are nitrided at higher energy indices show the reduction in intensity of wear and wear-in stage, and the level of permanent deterioration increases and along with the increase in the content of alloying elements this pattern becomes more pronounced.

2.2. Cavitation and erosion wear resistance of carbon structural steels

Unique dependencies of the intensity of the cavitation destruction of materials surfaces on the type of medium, the material, its phase composition and structure have not succeeded until now. This is primarily due to the fact that until now, an installation has been created that fully takes into account the real conditions for the cavitation, which is explained by the extraordinary complexity of the cavitation process and, accordingly, the difficulty of its implementation in the laboratory.

At present, hydrodynamic tubes or Venturi nozzles are used to model cavitation processes under laboratory conditions [15, 16]; installation with a rotating disk [17, 18]; shock erosion stands [19, 20] and installations with a magnetostrictive vibrator (MSV) [21–23]. The test method for MRI is based on the American Association for Testing Materials (ASTM) G32-72 standard [18]. It has high reproducibility of the results, is simple and relatively inexpensive and that is why it was accepted by us for testing on cavitation and erosion wear resistance of materials.

At present there is a very large number of different quality and composition brands of carbon structural steels. Data on their properties and purpose are given in the relevant reference literature, but there are no data on cavitation, hydro-erosion resistance.

Carbon steel, depending on composition and state, can have different structures and properties [24] and, accordingly, different resistance to cavitation fracture [21, 22]. As numerous studies have shown, for example, [15–23], the main effect on resistance to cavitation destruction is their structure, and therefore when conducting tests of carbon steels on cavitation it is convenient to use their classification according to the structure. Such a system is also chosen to analyze the characteristics of the cavitation wear resistance of carbon steel structures.

On the basis of own experimental data and analysis of literary sources, to systematize the laws and mechanisms of cavitation and erosion destruction of carbon structural steels depending on their heat treatment (structure) and the type of medium.

Cavitation stability of dodectoid carbon steels is determined mainly by the properties of two structural components – ferrite and perlite. Ferrite, other than carbon, can contain other elements (chromium, vanadium, titanium, etc.), which significantly affect its properties. Properties of perlite depend mainly on the form of cementite. Its grains may have a lamellar or globular shape [24].

In heterogeneous alloys, a less firm structural component is first deformed, for example, in carbonaceous steels the fracture begins with a ferrite, and then extends to the perlite grains. The degree of deformation of perlite depends on its structure. Plate perlite has a higher resistance to plastic deformation than granular. In the granular form of cementite, the main volume in the structure of perlite is ferrite [24] and as a result of resistance to plastic deformation decreases. In perlite steels, the centers of destruction occur on a ferrite grid or on the boundary between the ferrite and the carbide and extends to the side of the ferrite.

The perlite with carbides of the plastic form is destroyed uniformly, it has higher elastic properties, and in this case the ferrite-carbide mixture is more homogeneous and each of its components takes almost equal participation in the resistance of the micro-impact load.

Such a mechanism of destruction of surfaces of carbon dodectoid steels has been repeatedly confirmed by a metallographic analysis of samples with hydro-erosion, cavitation wear [19–21].

It is desirable to use high-quality carbon steel for the production of cavitation-resistant parts. In steels of standard quality, the digestion of phase components is considerably developed, which increases its electrochemical heterogeneity. In addition, in ordinary quality steels, there is a large number of nonmetallic inclusions and residues of deoxidation products. The accumulation of these impurities worsens cavitation wear resistance of steels. As a result, high-quality steel, despite the same mechanical characteristics, has 17...20 % higher cavitation wear resistance [19].

Cavitation wear resistance of zeutectoid steels is determined mainly by the properties of perlite. The mechanical properties of perlite depend on the dispersion of particles of cementite. As the degree of dispersion of the lamellar perlite increases, the boundary of strength and plasticity increases. The strength of the granular perlite is much less than the strength of the lamellar, but it has a higher plasticity [24]. Therefore, increasing the cavitation resistance of zeutectoid steels is primarily due to the increased level of their mechanical characteristics. These steels after quenching and low release have significantly higher cavitation wear resistance than pre-eutectoid steels. In this case, both types of steels are characterized by low corrosion resistance, and according to the technological properties, the preeutectoid steels considerably exceed the zeutektoid and therefore the use of the latter for the manufacture of cavitation-resistant parts is significantly limited, and for the manufacture of components of complex form they are almost not used [26–29].

The influence of carbon on cavitation and erosion stability is considered in works [19, 20, 29]. Of these, it follows that with an increase in the amount of carbon, the hydro-erosive stability increases for both annealed and tempered steel (Fig. 2.6) [19].

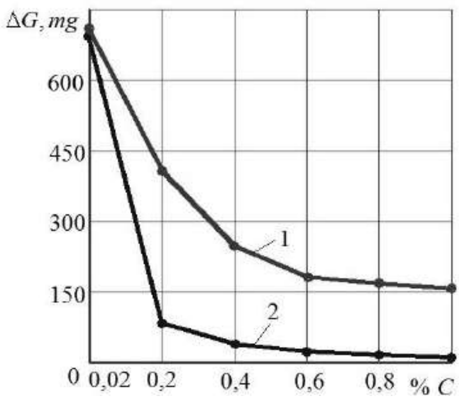

Fig. 2.6. Hydrozoerosic wear resistance of carbon steels depending on the carbon content

For annealed steel, increased erosion resistance is observed with an increase in carbon content from 0.6 % to 0.8 %. With further increase in carbon content, the erosion resistance is practically unchanged. For hardened steel, the optimum carbon content is 0.4...0.5 % and, with a further increase in its content, wear resistance is practically unchanged (Fig. 2.6). Apparently, a higher carbon content after quenching and low release does not increase the wear resistance of martensite.

Numerous studies [19–23, 29, etc.] indicate an increase in the cavitation stability of carbon steel with a fine-grained structure compared to large grain steels. The authors of the works note that, as a rule, weaker micro-sites, which can be found both in the body of grain and on its borders, are initially destroyed.

For fine-grained alloys, due to greater distortion of the crystalline lattice, greater resistance to plastic deformation of the boundary layers is observed rather than the grain itself [30, 31]. In addition, the fine-grained steel structure has higher rates of fatigue multicycle endurance in CAS than coarse-grained [30]. Therefore, when cavitation steel with a fine-grained structure is destroyed mainly by grain, and coarse grains – along the boundaries of grains.

In perlite steels, in the presence of cementite in the structure of the grid, destruction begins in the middle of the grain of perlite and on its boundaries; while the grid of cementite is stored for a long time (steel У12). In the presence of a ferrite mesh (steel 45) perlite grains are stored for a long time, and the ferrite network quickly collapses. In this case, with a smaller grain size of perlite, a finer ferrite mesh is formed that has an increased strength compared to a thick mesh formed with a relatively large perlite grain [24]. Consequently, a decrease in the value of perlite grain also leads to some increase in the erosion stability of steel [19, 32].

The conducted studies [15, 19, 28, 29, 35, etc.] show that the cavitation, hydrocarbon wear resistance of structural carbon steels of perlite and martensitic classes is determined mainly by the nature of the structures obtained as a result of their thermal treatment.

The largest cavitation and erosion wear resistance has the most homogeneous and strong structure of steel martensitic. At the same time, cavitation wear resistance of martensitic depends on its structure, carbon content and alloying elements of steel. With increasing carbon content, the hardness of martensitic during hardening increases [24] and simultaneously increases cavitation wear resistance [29].

The process of catastrophic destruction of steels tempered by martensitic develops gradually and begins after a long period of accumulation of deformations. This is characteristic of steel with a mild-to-fine structure of martensitic.

When quenching from high temperatures, when martensitic has a coarse-grained structure, the fracture develops much faster.

The holiday is the final heat treatment operation, which gives the steel its final properties, and is therefore decisive for the formation and cavitation wear resistance. For carbon steels, the general tendency is that, with increasing temperature, the hardness, strength ($\sigma_в$, $\sigma_{0,2}$) decreases, and the plasticity (δ, ψ) increases [24]. However, the change in these properties with increasing temperature of release is not monotonous. The release at 300 ºC leads to an increase in the strength and elasticity. The greatest ductility corresponds to the release at a temperature of 600...650 °C (for steel 40).

Conducting VV Fomin study of the wear and tear wear resistance of carbon steel 40 and U12A alloy steel 40X (perlite class) also showed the exceptional importance of tempering tempered steels for their wear resistance (Fig. 2.7).

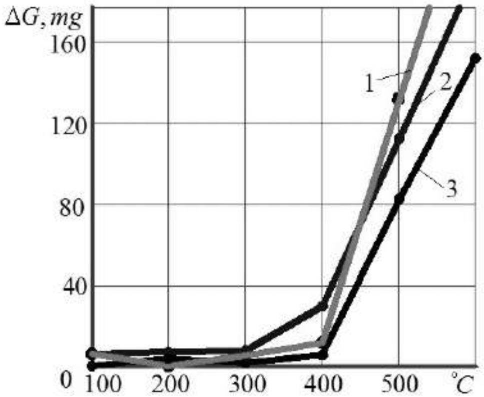

Fig. 2.7. Dependence of mass losses in hydrosis of tempered steels from the temperature of release: *1* – steel 40; *2* – steel U12A; *3* – steel 40XN

Mass losses increase sharply with the complete disintegration of martensitic, when sorbite appears in the steel structure (the temperature of release is above 400 °C).

At the release temperatures of 200 °C, martensitic is retained and the steel is characterized by high resistance to micro-shock destruction. At the release temperatures of 400 °C, troost appears in the structure of steels [24] and the erosive stability is somewhat reduced. At a release temperature of more than 400...600 °C, the structure of the steel has a sorbitol-like structure, and at 600 °C, the part of the carbides coagulates and takes the spheroidal shape, which dramatically reduces wear resistance.

At high release temperatures, ferrite-carbide mixtures in alloy steels have a greater dispersion than carbon steels [24], which increases their erosive wear resistance (straight *3* in Fig. 2.7).

Thus, the analysis of literature data and studies carried out by us show that the cavitation and erosion, hydrocarbon wear resistance of carbon structural steels is determined, first of all, by their structure.

Thermocyclic treatment (TCT) allows to obtain a fine-grained structure on carbon steels and pig-iron and, thus, to change their physical and chemical properties in the desired direction [19]. However, the analysis of literary sources indicates that in some cases, the "schematic" application of TCT for specific conditions for improving the reliability and durability of parts does not take into account the conditions of their work such as, cyclical loads, changes in temperature fields, aggressiveness of the corrosive environment, the type of wear, etc. However, for each case, optimal regimes and types of TCT, which are determined, first of all, by the material, the heating and cooling rate, the number of thermal cycles, should be used. The authors studied the influence of TCT on the steel 45 structure in order to further use of thermocycled samples to study the patterns of change in their electrochemical parameters, strength and durability characteristics.

The hardness of steels after the pendulum TCT remains virtually unchanged compared to their hardness after normalization. After the average temperature of TCT, the hardness of steel 45 increases somewhat. Thus, the Brinel hardness (HB) increases from 175 to 188 units after the average temperature of TCT, that is, approximately 7 %. Similarly, insignificant increase of hardness in the case of mid-temperature TCT was also obtained for steel 40X, which amounted to 230 HB after TCT and 215 HB after normalization.

The analysis of the mechanical characteristics of structural steels after TCT indicates that for steels 45 and 40X the gap strength is reduced, but at the same time the characteristics of plasticity increase: the yield line σ_T, the relative elongation δ and the relative narrowing of the section ψ. There is also a convergence of strength characteristics σ_V and σ_T, which is a positive factor in terms of the strength of metals (Table 2.3).

The most structurally sensitive characteristic was the impact strength of the destruction of a_H, which is significantly increased as a result of swing (from 1.9 to 3.14) and medium temperature (from 2.4 to 3.87 times) TSP. The analysis of the data obtained (Fig. 2.8) indicates that the optimal number of cycles for the swinging processing steel 45 n_{opt} = 5...6 and n_{opt} = 7...9 for steels 15X and 40X at the rotational and mid-temperature TCT. It was for the stabilized value of the impact strength found for each steel net, and then the other mechanical characteristics given in Table. 1.1. Properly similar approach is recommended in papers [19, 20].

Table 2.3

Mechanical characteristics of steels after TCT*

Steel	Pendulum TCT					Medium temperature TCT				
	σ_V	σ_T	δ	ψ	$a_H \cdot 10^4$	σ_V	σ_T	δ	ψ	$a_H \cdot 10^4$
	MPa		%		J/m^2	MPa		%		J/m^2
45	592/524	357/364	20,4/25,6	45,6/58	68/132	592/586	537/377	20,4/24,0	45,6/57,8	68/163
15X	550/573	375/402	27/31	57/62	73/147	550/580	375/408	27/34	57/64	73/212
40X	865/802	515/520	10,6/13,7	44/69	81/254	865/816	515/529	10,6/12,5	44/78	81/314

*Numerator – normalization; denominator – thermocycle treatment.

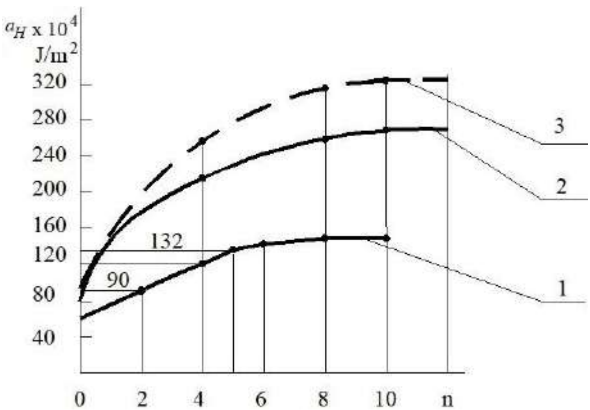

Fig. 2.8. Change in impact strength from the number of thermocycles *n*:
***1* – steel 45 at the pendulum TEC; *2* – steel 40X with a pendulum TEC;**
***3* – 40X steel with medium-temperature TCT**

The polarization curves (Fig. 2.9) were photocopied in a potent dynamical mode at a constant rate of scan of the sample potential, which was a working electrode. To obtain quantitative indicators of the rate of occurrence of corrosion processes on the basis of the Tafel equation, using the mathematical method of finding the curvature of polarization curves and the computer analysis on the basis of this, and based on the method described in [35], found currents of corrosion at normalization and at TCT of steels.

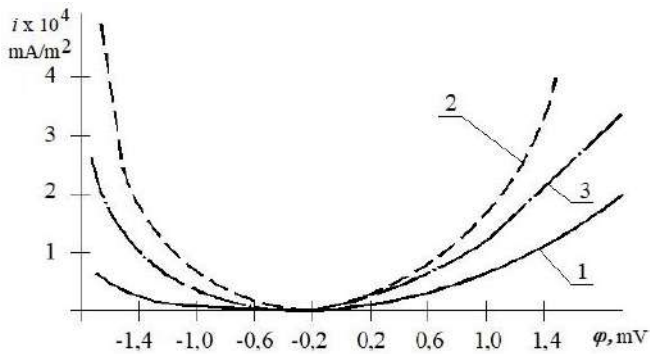

Fig. 2.9. Polarization curves of steel 45:
1 **– in hard water after normalization;**
2 **– in 3 % NaCl solution after normalization;**
3 **– in 3 % NaCl solution after mid-temperature TCT**

Comparison of polarization curves (PCs) shows that, along with the displacement of the established potential φ_{vst} into the positive region for samples after TCT, in comparison with normalized, there is an extension of the passive zone. Thus, the passive area of samples of steel 45 after TCT is from – 0.0 to 0.2 V in a solution of sodium chloride, without yielding thus the corrosion resistance of normalized steel 45 in hard water. In addition, in the anode and in the cathode regions of the polarization curves, the angle Tof their inclination to the abscissa axis for thermocycled samples is slightly lower than for the normalized ones. The latter indicates a decrease in the rate of corrosion processes in the investigated media.

Found, according to our method of corrosion currents, confirm this conclusion. They decreased for thermocycled steel samples 45 compared to normalized at 1.23 and 1.52 times, respectively, when tested in severe water and solutions of sodium chloride. The study of low cycle fatigue showed that the highest value of the endurance limit is in the alkaline medium, both for normalized and for thermocycled samples, and the lowest value in the acidic medium (apple juice (Fig. 2.10). In this case, the value of endurance in alkaline medium exceeds the values of endurance indices in the air.

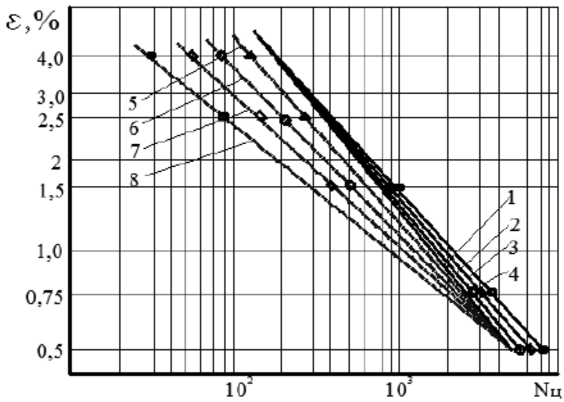

Fig. 2.10. Low-cycle durability of steel 40X after pendular TCT (*1*–*4*) and after normalization (*5*–*8*) in the media: 1.5 – alkaline with pH12; 2.6 – in the air; 3.7 – neutral (3 % NaCl solution with pH7); 4.8 – sour (apple juice with pH6.5)

The increase of low cyclic durability in alkaline medium compared with the durability in neutral, acidic environments and in the air is due to the formation of a hydroxide layer on the surface, which prevents the access of oxygen to the deformation zone and reduces the dismembering effect of oxides.

Intense electrochemical processes of dissolving steels in an acid medium result in the formation of a large number of stress concentrators, which reduce the fatigue strength of both normalized and thermocycled samples (straight lines 4 and 8 in Fig. 2.10). In solutions of sodium chloride with a lower, compared with acidic medium, corrosion activity of low-cycle durability of steel increases. However, with increasing amplitude of cyclic deformation, the influence of aggressiveness of the medium on the durability is weakened and at ε 3.5 % for thermocycled and ε 3.0 % for normalized samples the equilibrium of their durability in the air and in the corrosive medium takes place [34, 35].

Taking into account the fatigue nature of wear, the multi-cyclic fatigue life of thermocycled specimens in corrosive-active media was investigated. The studies showed that multi-cyclic fatigue endurance of 40X steel after the average temperature of the TCT compared with normalization increased in air from σ_{-1} = 160 MPa to σ_{-1} = 187 MPa, that is 17 %, and in solutions of sodium chloride with σ_{-1} = 124 MPa up to σ_{-1} = 156 MPa, or 26 % (Fig. 2.11). The results obtained can be explained by the fact that corrosion resistance grows at TCT and this increase is higher than the higher corrosion activity of the medium. As a result, the number of "corrosive" centers of stress concentrators decreases. The great influence on fatigue endurance, possibly basic, has an increase in the characteristics of steel ductility after TCT, and especially the impact strength.

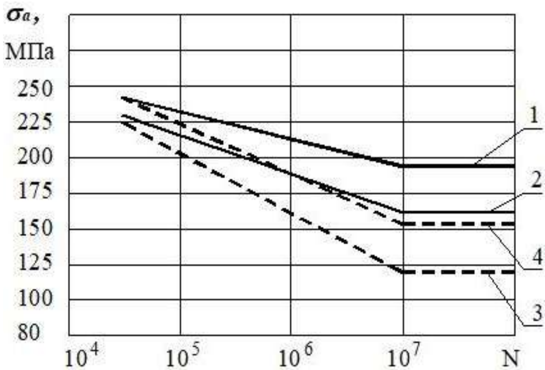

Fig. 2.11. Multi-cycle endurance of steel 40X in the air:
***1* – after average temperature TCT; *2* – after normalization and 3 % NaCl solution;**
***3* – after normalization; *4* – after mid-temperature TSP**

When cyclic loading of samples in a liquid medium, in accordance with the hydrodynamic theory of the propagation of shock waves, shock wave phenomena largely determine the intensity and ratio of elastic and plastic deformation of surface metal layers. The influence of the medium thus manifests itself in the change in the surface energy of the metal, which makes it difficult or easier to discharge the dislocations in the surface layer.

At long load (multi-cycle endurance $\sigma_A << \sigma_T$) and at low cyclic endurance, especially at $\sigma_A > \sigma_T$, from the first cycles of loading of the dislocation form a cluster. Under the influence of the external stress σ_A

and the forces of interaction with other dislocations, in the head of the cluster there are stresses exceeding the shear strength – there is a violation of continuity, the emergence of microcracks. Microcracks are formed in metal volumes, where the density of dislocations reaches a critical value [22]. The formation of microcracks facilitates the discharging of discharges to them, causing the leveling of the layer. The number of microcracks increases over time, which leads to more intensive stretching due to a decrease in the length of the run of dislocations. In this case, the displacement of dislocation clusters to microcracks can restore the activity of previously not working sources of dislocations, which causes an increase in the density of linear defects and a decrease in the rate of expansion [22].

Thus, the cyclic strength of metals is proportional to the energy intensity of their surface layers, which is determined by the energy expended on the deformation and cracking of the metal until the formation of the main crack fractures. For steels after TCT, the energy of the impact strength a_H is much larger and, accordingly, the duration of the strengthening layer of the surface layers is much longer, and the strengthening cycle itself – strengthening is also longer in time. That is why we have higher characteristics of endurance of samples after TCT when tested in air and in a medium of sodium chloride. At the same time, the multi-cycle endurance of samples in the air exceeds its value in the corrosive-active medium both during normalization and at their TCT. It is known that the deformation and destruction of materials under the simultaneous action of the medium, especially the corrosion – active medium, occurs at significantly lower mechanical stresses [30].

The analysis of the above data shows that thermocycled samples have higher corrosion resistance under static conditions (without cavitation) compared to normalized in hard water and in 3 % sodium chloride solution. Consequently, TCT can be an effective method for increasing the corrosion resistance of carbon structural steels. Also, the obtained data indicate that at 40 μm oscillation amplitudes, the thermocycled and normalized samples in a 3 % solution of NaCl showed practically the same stability. When the amplitude of oscillations decreases (decreasing the rigidity of the microwardload) from 40 to 28 microns, the stability of the thermocycled samples increased by 1.35 times compared to normalized (3 % NaCl). In studies in hard water, thermocycled and normalized samples at amplitudes of oscillations of the vibrator 40 and 28 μm showed almost the same stability (Table 2.4).

Table 2.4

Influence of pendular TCT on cavitating and erosion and corrosion resistance of steel 45

Environment	Amplitude *a*, μm	Number of hermocycles *n*	Corrosion current *i*, mA/cm^2	Mass loss Δ*m*, mg/cm^2
3 % NaCl	0*	Normalization	0,0079	–
–«–	0*	5	0,0052	–
Hard water	0*	Normalization	0,0037	–
–«–	0*	5	0,0030	–
3 % NaCl	40	Normalization	–	12,0
–«–	40	5	–	11,8
–«–	28	Normalization	–	4,2
–«–	28	6	–	3,2
Hard water	40	Normalization	–	4,8
–«–	40	6	–	4,8
–«–	40	6	–	4,7
–«–	28	8	–	2,4
–«–	28	Normalization	–	2,6
–«–	28	6	–	2,5

0* – without superimposed ultrasonic oscillations (static)

Cavitation-erosion fracture in a corrosive environment is one of the subspecies of corrosion-mechanical wear (KMW) of metals and alloys [35]. Corrosion-mechanical deterioration of metals is considered as a process based on the fatal-electrochemical nature. In this case, electrochemical processes play the role of catalyst for fatigue failure. However, the role of the corrosive medium is quite significant and the contribution of corrosion to the overall intensity of surface fracture at the microstroke load depends on the correlation between the corrosion and mechanical factors of wear. Curve analysis: the intensity of wear (total mass loss) – the rigidity of the load (the amplitude of the MSV fluctuations), and corrosion losses – the stiffness of the load showed that they are similar to the curves of superficial fatigue. On these curves there are three distinctly delimited zones [36]:

1) zone of intense corrosion-fatigue fracture with the predominant influence of corrosion processes (elastic zone, amplitude, $a \leq 5$ microns);

2) the zone of multi-cycle surface corrosion-fatigue failure with significant impact of corrosion on the total mechanical and chemical wear (elastic zone, a = 5...20 microns);

3) the zone of intense malocyclical destruction with a non-essential role of the corrosion factor (zone of predominantly plastic deformation, and > 20 microns).

Proceeding from this, taken by us during research, modes of micro-impact load a = 28 and 40 microns belong to the zone of intensive low-cycle load with a negligible role of corrosion factor of destruction. It is precisely this that one can explain the practically identical results of wear resistance at a = 40 microns in hard water and in 3 % sodium chloride solution. The mechanical destruction factor in this case is much greater than the corrosion component of the fracture. The same can be said for a = 28 μm when tested in hard water. A slight increase in the corrosion resistance of thermocycled samples (in 1,23 times) with insignificant influence of corrosion factor of destruction completely equaled the insignificant effect of increasing corrosion resistance (in 1,23 times).

When wearing in a solution of sodium chloride at a = 28 microns, an increase in corrosion resistance in 1.52 times resulted in an increase in cavitation and erosion resistance of 1.35 times. This can be explained by the fact that the research mode was closer to the zone of multi-cycle surface corrosion-fading destruction (zone 2) and with more significant influence of the corrosion resistance of thermocycled samples received a more significant increase in overall wear resistance.

Grinding of grain, in particular by TCT methods, leads to an increase in the fatigue strength of metals. Thus, according to the data obtained by us (Fig. 2.11, the average temperature TCT of steel 40X increases the limit of endurance in the symmetric cycle of loads with σ_{-1} = 167 MPa to σ_{-1} = 216 MPa, that is, almost 30 %.

Considering the fatigue-electrochemical mechanism of destruction of the surface metal layers, it would also have to be expected a more significant increase in cavitation stability of steel 45 after TCT. Obviously, the explanation of the results obtained by the reasons outlined above is not enough. It is necessary to look for them also in the relationship between the specificity of the micro-shock load and the resulting structure of the layers after the TCT.

It is known [21] that the area of the cells of the destruction of metal under cavitation is many times smaller than the size of the transverse size of the area of the grain and is proportional to the individual structural components having different strength characteristics, different ability to strengthen the phases. In accordance with this destruction, the surface layer of the metal passes initially in certain "weak" places, which for steel 45 are the boundaries of ferrite and carbide inclusions in the ferrite.

With the swirling method of thermocycling, the grain of perlite is crushed, and the ferrite remains unchanged. As a result, we obtain a structure in which the small interstices of perlite are surrounded by ferrite. Due to the micro-impact load, the destruction of the metal begins at the boundary of the ferrite component and subsequently develops in the direction of the ferrite. Thus perlite inclusions appear to be separated from the bulk of the metal, which leads to a significant weakening of the mechanical connection between the structural components. The next cuvette effect of the liquid medium is "washes out" the perlite grains, which is the reason for the intense wear of thermocycled specimens.

In the case of the application of a medium-temperature TCT throughout the cross-section, a structure of granular sorbitol-like perlite was obtained. However, it is known that steel with a grain perlite structure has less resistance to cavitation fracture than steel with a structure of plate perlite [5, 6]. In the plate form of the ferrite-cementite mixture, each phase is almost equally involved in the resistance of the micro-impact load. In the globular form, the surface of the carbide phase decreases and therefore the fraction of its participation in the resistance to destruction also decreases.

Consequently, studies have shown that the use of carbon monoxide steel structures is first and foremost in view of increasing their corrosion resistance, as well as increasing corrosion-mechanical wear resistance under loads with a predominant influence on the corrosion factor of fracture and, in part, with multicyclic surface corrosion-fatigue fracture with significant corrosion effects on the total mechanical and chemical deterioration.

Main conclusions

1. Cavitation stability of dodectoid carbon steels is determined mainly by the properties of two structural components – ferrite and perlite. Destruction begins with ferrites, and then extends to perlite grains. At the same time, the plate perlite has a higher resistance to plastic deformation than granular.

2. Cavitation wear resistance of zeutectoid steels is determined mainly by the properties of perlite. Increasing the cavitation resistance of zeutectoid steels is primarily due to the increased level of their mechanical characteristics. These steels after quenching and low release have significantly higher cavitation wear resistance than preeutectoid steels. In this case, both types of steels are characterized by low corrosion resistance, and according to the technological properties, the pre-eutectoid steels are significantly higher than the eutectoid ones, and

therefore the use of the latter for the production of cavitation-resistant parts is considerably limited, and they are hardly used for the manufacture of components of complex shape.

3. Studies have shown that cavitation, hydrous wear resistance of structural carbon steels of perlite and martensitic classes is determined mainly by the nature of the structures that are obtained as a result of their thermal treatment. The highest cavitation and erosion wear resistance has the most homogeneous and strong structure of steel martensite. At the same time, cavitation wear resistance of martensite depends on its structure, carbon content and alloying elements of steel. With increasing carbon content, the hardness of martensite during hardening increases and at the same time cavitation wear resistance increases.

4. With the increase in the amount of carbon, the hydro-erosion resistance increases for both burnt and hardened steel. For annealed steel, increased erosion resistance is observed with an increase in carbon content from 0.6 % to 0.8 %. For tempered steel, the optimum carbon content is 0.4...0.5 % and, with further increase in its content, wear resistance is practically unchanged.

5. At the release temperatures of 200 °C, the martensitic is retained and the steel is characterized by high resistance to microimpact destruction. At the release temperatures of 400 °C, troosit appears in the structure of steels and the erosive strength is slightly reduced. At a release temperature of more than 400...600 °C, the structure of the steel has a comorphoid structure, and at 600 °C, the part of the carbides coagulates and takes the spheroidal shape, which dramatically reduces wear resistance.

6. The conducted studies point to the prospect of the use of TCT carbon structural steels the first in terms of increasing their corrosion resistance, as well as increasing the corrosion-mechanical wear resistance in loads with a predominant influence of corrosion factor of fracture and, partly, with multicyclic surface corrosion-fatigue fracture with significant corrosion effects on the total mechanical and chemical deterioration.

2.3. Corrosion and mechanical wear of nitrogen steels in acid environments

Much attention in the study of the problem of increasing the reliability and durability of machines and equipment is given to the problem of friction and wear, since the overwhelming majority of machines fail due to surface wear of individual parts and assemblies. In the field of mechanical engineering, financial losses due to friction and wear reach 5 % of the national income. At the same time, according to research data, from a quarter to a third of all the energy generated in the world during the year is currently spent on overcoming friction forces in the moving joints of machines. When solving the problem of reducing power costs for friction and wear in machines and increasing their reliability and durability, the main set of measures is related to the choice of materials for friction pairs. The need to maintain a rational ratio between their cost and the appropriate level of operational characteristics will contribute to the growth of the role of various methods of strengthening surface layers, since it is the condition of the surface that determines the durability of machine parts. The structural and phase state of the surface layers of metals determines their wear resistance. One of the effective methods that improves the physical and mechanical properties of structural steel surfaces is chemical heat treatment. Chemical-thermal treatment in controlled oxygen and nitrogen-containing gaseous media pro-vides the formation of a gradient hardened layer. Depending on the physical and mechanical characteristics of the near-surface layer modified with oxygen or nitrogen, it is possible to increase the reliability under different types of loads [37–38]. It is also possible to significantly increase the wear resistance of technological methods [39–40]. It is shown that the increase of corrosion and mechanical strength during friction and cavitation of nitrided structural steels is due to the formation of the maximum level of residual compressive stresses [41], grinding subgrain structure and the formation of ordered cell dislocation structure [42]. In [43] the electrochemical and corrosion characteristics of diffusion layers formed in metals nitrided in a glow discharge were studied in acidic model media. A rela-tionship has been established between the thermodynamic potential of nitrided surfaces and their electrode potential. In [44–46] the tribological behavior of steel parts with modified surface layers in different operating conditions during fretting, for reinforcing tools and others is analyzed. Further progressive directions of application of technical surfaces of machine parts strengthened by nitriding in glow discharge and recommendations for practical use are also considered in papers [47–50].

Therefore, there is practically no information in the literature regarding tribological tests of steels nitrided in a glow discharge, which are operated in acidic environment.

Structural steels of the following grades were selected for the study: C20, C45 – high-quality carbon, 37Cr4 – chromium and 41CrAlMo7-chromium-aluminum with molybdenum of high quality. The experiments were performed in an acidic model environment: 2 % citric acid solution C3H8O7 × H2O. Hydrogen nitriding in the glow discharge was carried out at the industrial installation BATR, which is additionally equipped with heating elements placed in the gas discharge chamber. This made it possible to arbitrarily change the energy parameters: voltage *U* and the value of current density *g* (current ratio to the total area of the cage and suspension). To study the corrosion-mechanical wear resistance of materials in a wide range of loads and working environments, an end friction setup was used (Fig. 2.12).

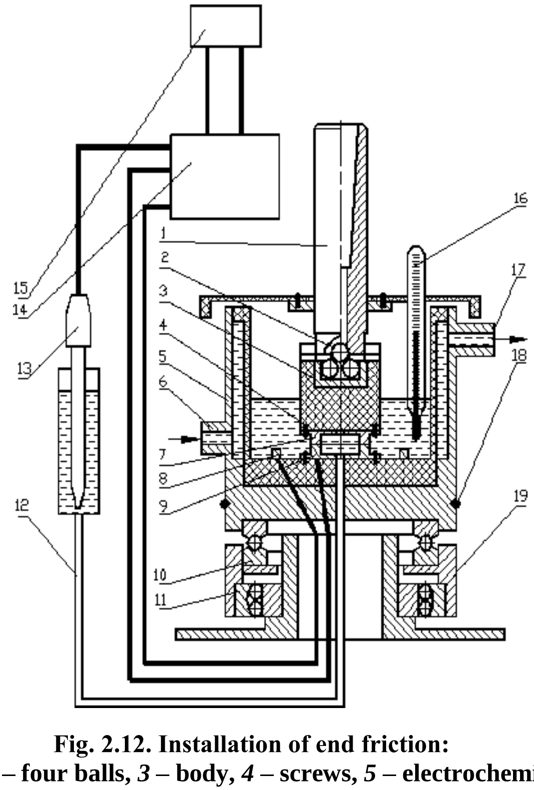

Fig. 2.12. Installation of end friction:
1 **– cone,** ***2*** **– four balls,** ***3*** **– body,** ***4*** **– screws,** ***5*** **– electrochemical cell,**
7 **– upper sample,** ***6–17*** **– fitting,** ***8*** **– electrode,** ***9*** **– lower sample,**
10–11 **– bearings,** ***12*** **– tube,** ***13*** **– reference electrode,** ***14*** **– potentiometer,**
15 **– potentiometer,** ***16*** **– thermometer,** ***18*** **– housing**

The friction machine makes it possible to obtain the kinetics of changes in the electrode potential, frictional and wear-resistant characteristics, the temperature of the friction surface, and the friction characteristic depending on the change in the electrode potential of the system.The installation consists of a rigid bed, a working chamber, a spindle assembly, a drive and a loading device, measuring and recording equipment for measuring and recording electrode potentials, friction characteristics and temperature on the friction surface of the sample.

The kinetics of electrochemical processes in static conditions, with stirring and friction were studied on a P-5827M potentiostat, and polarization curves were recorded with a PDP4-002 potentiometer. Electrode potentials were measured relative to the chlorine-silver reference electrode EVL-1M1 in a saturated KCl solution supplied to the friction zone.

The wear resistance of the friction pair was evaluated by measuring the linear wear of the samples and recording the friction force. The force of friction was measured by the tensometric method. The linear wear of the samples was determined by an indicator with a division price of 1 μm. The upper sample made of CT105 steel, hardened to HRC 61…63, had two grooves that provided free access of the medium to the friction surface. The sam-ple of the studied material served as the bottom. The heating of the samples in the contact zone did not exceed 393 ºK, which excluded the possibility of structural transformations.

The average temperature on the surface of the sample was measured using a KSP-2-23 electronic potentiometer at a distance of 1 mm from the friction surface. For this purpose, a chromel-alumel thermocouple with a diameter of 0.5 mm was used.

Polarization curves in statics and during friction were recorded in the potentiodynamic mode. The sweep rate (change in the potential of the working electrode over time) was constant in all experiments (with a potential multiplier equal to one). A silver chloride electrode immersed in an electrolyte served as a standard electrode. Auxiliary – platinum electrode was placed until the contact was completely immersed in the working solution. The corrosion current was determined by extrapolation of the linear Tafel segments of the polarization curves to the region of low overvoltages. According to the corrosion current, taking into account the fact that iron passes into solution in the form of divalent ions, the corrosive weight loss of the samples was determined according to the Faraday law. The total wear of the samples was measured on a friction machine. To separate the mechanical component, the calculated corrosion mass losses were subtracted from the total wear.

A comparison of the results of weight loss determined by the gravimetric method and by the corrosion current shows that the relative error at is no more than 7 % in an acidic environment. The results obtained indicate a satisfactory correlation between the intensity of corrosion processes obtained by electrochemical and gravimetric methods. Thus, the corrosion current and the mass loss calculated from it are used to quantify the corrosion factor of destruction in this type of wear.

Metallographic studies of nitrided samples were performed after etching in 3 percent alcoholic nitric acid solution. Measurements of the thickness of the nitride zone were performed on an RX50M microscope. Microhardness was determined on a DuraScan-20 microhardness tester at a load of 1.0 N. When conducting electrochemical measurements, experiments were repeated 3…5 times, and during corrosion and wear tests, they were repeated 5…6 times. Statistical processing of the obtained results was carried out according to standard methods.

Research results and discussion. Fig. 2.13 shows the structure of the surface layer of 37Cr4 steel after applying the technology of anhydrous nitriding in a glow discharge. The structure and phase composition of nitrided layers is determined by a combination of technological and energetic processes of formation of the nitrided layer. Strengthening was carried out according to optimal modes in relation to operating conditions, i.e. increasing the corrosion-mechanical wear resistance of steels in acidic environments (843 K, 75 % N_2 + 25 % Ar, 265 Pa, 4 h), taking into account the results of work [41]. In the photo, the nitride layer is represented by a white stripe.

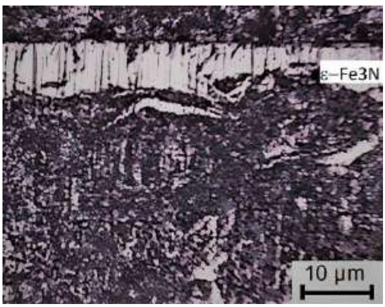

Fig. 2.13. Microplates of nitrided steel 37Cr4
(8.7 µm – nitride zone; 300 µm – modified zone)

In the initial state, the structure of the nitrided layer consists of a layer of iron nitrides, represented mainly by ε – Fe_3N and a diffusion zone consisting of an α-solid solution doped with nitrogen and nitrides of alloying elements.

To analyze the tribological properties of the investigated materials, the results of wear and friction tests were obtained depending on the pressure on the frictional contact and the sliding speed. Fig. 2.14, *a*, *b*, as an example, shows graphical dependences of wear intensity for 41CrAlMo7 steel for samples hardened and not hardened by nitriding.

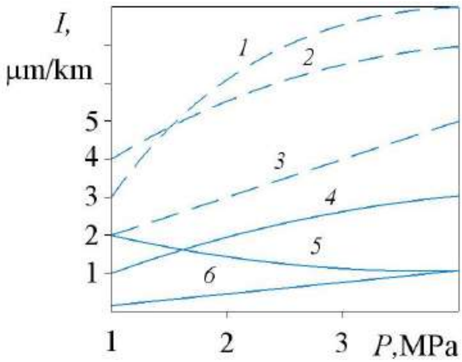

a

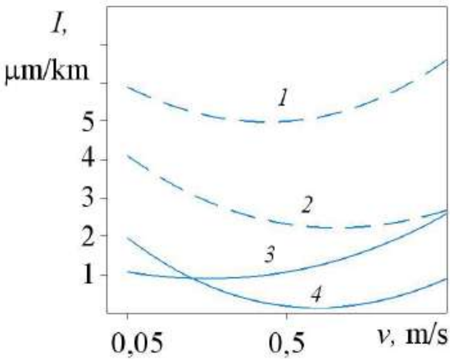

b

Fig. 2.14. Dependence of the wear intensity *I* of steel 41CrAlMo7 in an acidic environment on pressure *P* (*a*) and sliding speed v (*b*): dashed lines – without hardening; solid – after nitriding (*a*: *1, 4* – *v* = 1 m/s, *2, 5* – 0.05, *3, 6* – 0.5; *b*: *1, 3* – *P* = 4 MPa, *2, 4* – 1)

Based on the analysis of the obtained experimental results, it was established (Fig. 2.14) that with an increase in the pressure in the frictional contact, the intensity of wear of nitrided and non-nitrided materials increases. And for the sliding speed v = 0.5 m/s for nitrided layers, on the contrary, it decreases (Fig. 2.14, *a*). Unhardened steels 41CrAlMo7 and 37Cr4 wear the least at a sliding speed of 0.5 m/s (Fig. 2.14, *b*).

Wear of other materials (hardened by nitriding and unhardened) increases with increasing sliding speed (Table 2.5). As the pressure in the frictional contact increases, the friction coefficient f increases, and at v = 0.05 m/s it remains constant in the entire investigated pressure range (Fig. 2.14, *a*). At a pressure of 4 MPa, it has a maximum at a speed of v = 0.5 m/s, and in other cases, it decreases with increasing sliding speed (Fig. 2.14, *b*).

Table 2.5

The dependence of the intensity of wear *I* (µm/km) and the coefficient of friction f of materials in an acidic environment on the sliding speed v and pressure *P**

Material		Sliding speed v, m/s								
		0.05			0.5			1.0		
		Friction contact pressure P, MPa								
		1.0	2.0	4.0	1.0	2.0	4.0	1.0	2.0	4.0
C20	*I*	4/2	5.5/1	7/0.4	2/0.25	10/0.5	14/1.2	3/1	7/3.5	9/5
	f	0.32/0.25	0.32/0.25	0.32/0.25	0.20/0.14	0.39/0.25	0.65/0.54	0.07/0.06	0.12/0.10	0.19/0.16
C45	*I*	4/2	5.5/1	7.0/0.7	2.00/0.25	8.00/0.5	10/1.1	3/1	7/3	9/4
	f	0.32/0.25	0.32/0.25	0.32/0.25	0.20/0.14	0.35/0.25	0.63/0.53	0.07/0.06	0.12/0.10	0.19/0.16
37Cr4	*I*	4/2	5.5/1.5	7/1	2.00/0.25	3.0/0.5	5/1	3/1	6/2	8/3
	f	0.32/0.25	0.32/0.25	0.32/0.25	0.20/0.14	0.32/0.24	0.54/0.50	0.07/0.06	0.11/0.09	0.18/0.15
41CrAlMo7	*I*	4/2	5.5/1.5	7/1	2.00/0.25	3.0/0.5	5.0/0.9	3/1	6.0/1.5	8/2
	f	0.32/0.25	0.32/0.25	0.32/0.25	0.20/0.14	0.32/0.24	0.53/0.50	0.07/0.06	0.11/0.09	0.18/0.15

*Numerator – unreinforced materials, denominator – strengthened by nitriding.

Table 2.5 shows an array of data from the experimental results of determining the tribological characteristics of nitrided and unhardened steels depending on operational factors. The numerator shows the values for unreinforced materials, and the denominator shows the values for reinforced ones. These results are averaged after appropriate statistical processing. All obtained results show a positive effect of nitriding hardening on the reduction of wear intensity and friction coefficient.

The decrease in the intensity of wear of 37Cr4 and 41CrAlMo7 steels with an increase in the sliding speed from 0.05 to 0.5 m/s is explained by the reduction of the contact time of individual contact spots, the interaction of the corrosive environment with juvenile areas of the surface, and the partial manifestation of the hydrodynamic effect.

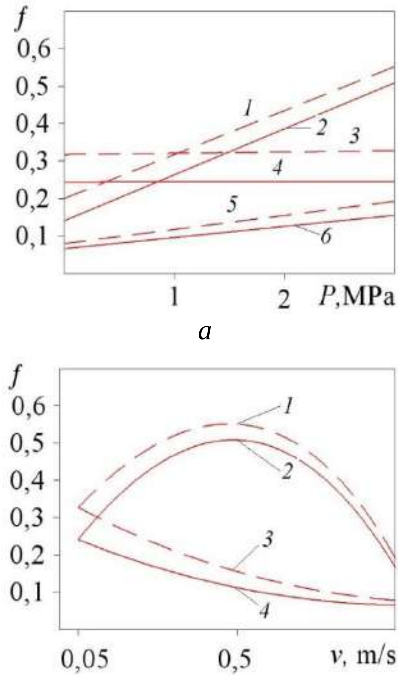

a

b

Fig. 2.15. Dependence of the friction coefficient f of steel 37Cr4 in an acidic environment on pressure *P* (*a*) and the sliding speed *v* (*b*); dashed lines – without hardening; solid – after nitriding (*a*: *1, 2* – *v* = 0.15 m/s, *3, 4* – 0.05, *5, 6* – 1; *b*: *1, 2* – *P* = 4 MPa, *3, 4* – 1)

For unstrengthened steels 20C, 45C, the maximum intensity of wear was recorded at v = 0.5 m/s and P = 4 MPa, which was caused by the activation of the mechanical factor of destruction. For nitrided materials, the minimum wear resistance corresponds to a speed of 1 m/s and a pressure of 4 MPa.

It is obvious that the high coefficient of friction (Fig. 2.15, *a*) and low intensity of wear for alloyed steels 37Cr4 and 41CrAlMo7 (Fig. 2.15, *b*) at speeds v = 0.5 m/s can also be explained by the formation of dense protective films, the strength of which is much higher than on carbon steels. The ratio of corrosive and mechanical components in the general process of wear under the action of a cold environment was also investigated. The results of such studies are shown in Table 2.6 and Fig. 2.15.

Table 2.6

Corrosion and mechanical wear ratio depending on pressure during friction of 37Cr4 steel in an acidic environment

Pressure, MPa	Corrosion current, A/m^2	Corrosion rate	Intensity of mechanical wear	Total wear rate	The percentage of corrosion destruction, %
		g/(m^2 · h)			
1	1,77	1,84	0,16	2	92
2	0,86	0,9	0,6	1,5	60
4	0,41	0,43	0,57	1	43

Fig. 2.16 shows a graphical interpretation of surface wear rates versus corrosion and mechanical components as the contact pressure increases. The graphs show that increasing the load reduces corrosion, but activates mechanical wear.

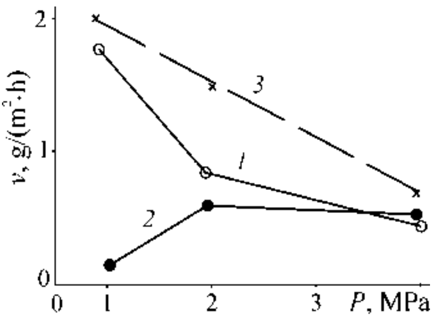

Fig. 2.16. Dependence of the corrosion rate (curve *1*), mechanical (*2*) and total (*3*) wear during friction of steel 40X in an acidic environment on the pressure is the friction contact *P* (v = 0.05 m/s)

The next block of research is devoted to the analysis of the influence of the temperature of the surface layers on the tribological properties of nitrided samples operating in an acidic environment. Table 2.7 shows how the working load in frictional contact affects the formation of the surface temperature.

Table 2.7

The temperature of the nitrided surface of steel 37Cr4 when rubbed in an acidic environment depending on the load conditions on the friction contact*

v = 0,5 m/s			*v* = 1 m/s		
P, MPa			*P*, MPa		
1	2	4	1	2	4
298/298	318/303	333/313	298/298	333/313	363/338

*The numerator is normalization, the denominator is nitriding.

The percentage share of the corrosion factor of wear in the general process of nitrided steel 37Cr4 decreases with increasing pressure. Based on the results of the research (Table 2.7), the dependence of the corrosion and mechanical factors of destruction on the pressure shows (Fig. 2.16) that at v = 0.05 m/s the rate of total mass loss vt (up to P = 4 MPa) is controlled by the rate of corrosion loss, which decreases with increasing pressure in the frictional contact. It is obvious that at the initial moment of corrosion-mechanical impact, the formed juvenile surfaces are covered with protective films (increase in vmech to P = 2 MPa), which shield the friction surface from the influence of an acidic environment (decrease in vcorr to P = 2 MPa). At the same time, the forces in frictional contact are insufficient for their destruction. With an increase in the pressure in the frictional contact from 1 to 2 MPa, the influence of the corrosive factor is sharply weakened and the mechanical factor increases up to P = 4 MPa. Further, the mechanical factor of destruction begins to prevail over the corrosive factor. One of the factors that have a significant impact on the behavior of nitrided layers is the friction surface temperature. As can be seen from Table 2.8, increasing the pressure on the friction contact leads to an increase in temperature at the friction surface. The temperature on the nitrided surface is much lower than on the surface after the normalization process due to the higher heat capacity of iron nitrides compared to iron. This creates the conditions to prevent temperature flares on the surface during friction. In Fig. 2.17 shows graphs for the intensity of wear of steel depending on the parameters of ionic nitriding. From Fig. 2.17 it follows that the most optimal structure of the nitrided surface layer is formed at T = 843…873 K, nitrogen content of 75 % and gas pressure of 265 MPa. It was found that steel 37Cr4 has the lowest wear resistance at a nitriding temperature of 793 K ε-phase, which is formed in this case on the steel surface has increased brittleness, which significantly reduces the wear resistance of the surface layer. Increasing the nitriding temperature to 873 K increases the stability of steel, which is caused by an increase in the relaxation capacity of the surface layers due to a decrease in the concentration of nitrogen in it.

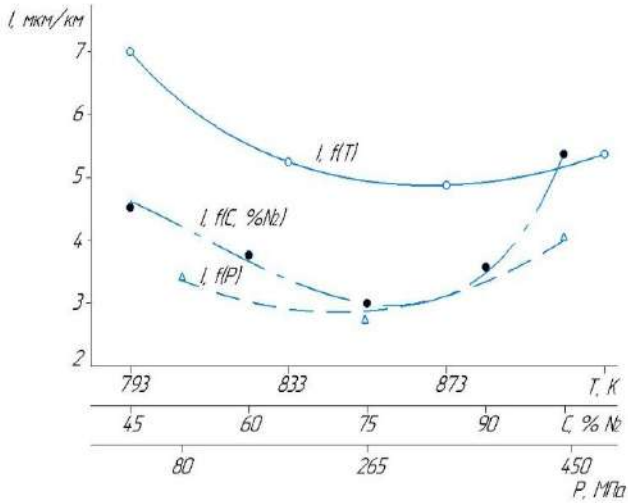

Fig. 2.17. Dependence of the intensity of wear *I* of steel 37Cr4 in an acidic environment on the parameters of ionic nitriding (wear test mode: sliding speed *v* = 1m/s, pressure *P*= 4 MPa): *1* – *I* = *f*(*T*); *2* – *I* = *f*(C, % N_2); *3* – *I* = *f*(*P*)

A further increase in temperature to 913 ºK leads to a decrease in wear resistance. The decrease in wear resistance with increasing pressure of the nitrogen-argon mixture to 450 MPa and an increase in its nitrogen content is also due to an increase in the content of ε-phase in the surface layer.

Temperature dependences for the coefficient of friction are shown in Fig. 2.18. From Fig. 2.18 it follows that the lowest coefficient of friction corresponds to a nitriding temperature of 873 K, a nitrogen content of 75 % and a medium pressure of 265 MPa.

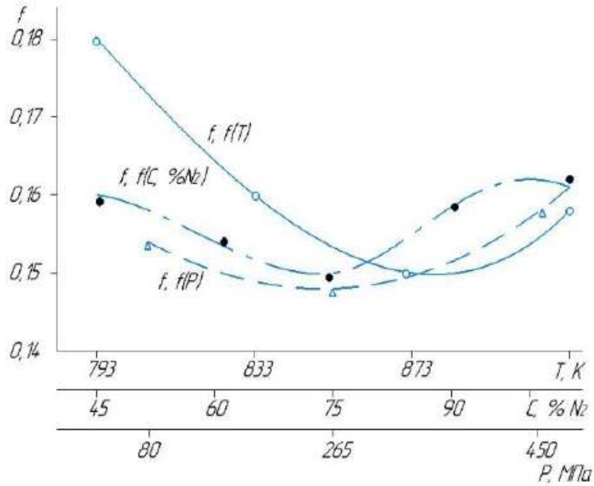

Fig. 2.18. Dependence of friction coefficient of steel 37Cr4 in an acidic environment on the parameters of ionic nitriding (wear test mode: sliding speed *v* = 1 m/s, pressure *P* = 4 MPa): *1* – *I* = *f*(*T*); *2* – *I* = *f*(C, % N_2); 3 – *I* = *f*(*P*)

It is known that tightly packed hexagonal lattices tend to be oriented so that the base (hexagonal) plane is parallel to the direction of sliding. At the same time, the bonding forces between adjacent hexagonal base planes are relatively small, which reduces the coefficient of friction and prevents the occurrence of setting processes. Increasing the nitrogen content in the gaseous medium leads to a decrease in the content of Fe_3N nitride in the surface layer and, accordingly, to increase the resistance to corrosion and mechanical wear of nitrided surfaces.

Further, experimental studies were carried out on the influence of the quantitative and qualitative content of sucrose in the medium solution on the tribological properties of 37Cr4 steel.

Many sugar intermediates (diffusion, sulfated, saturated, defecated juices, syrups, massecuite, molasses) contain significant amounts of sucrose. To develop sound recom-mendations for the choice of materials that work in these environments, it is necessary to determine the effect of sucrose on the corrosion and mechanical wear resistance of nitrided steels. Listed in Table 2.8 data show that the presence of sucrose in solutions increases the stability and reduces the coefficient of friction.

The increase in the strength of materials in sucrose solutions is due to a decrease in their electrical conductivity, as well as high lubricating properties of sucrose. Thus, the addition of 15 % sucrose increases the stability of improved and nitrided steel 37Cr4 in distilled water, respectively, 1.8 and 4.3 times, and in a buffer solution of citric acid in 1.4 and 1.5 times.

Table 2.8

Influence of sucrose on corrosion-mechanical wear resistance of 37Cr4 steel (*v* = 1 m/s, *P* = 4 MPa)*

Tribological parameters	Distilled water	Distilled water + 15 % sucrose	Citric acid buffer solution	Citric acid buffer solution + 15 % sucrose
Wear intensity *I*, μm/km	12/1.4	2.8/0.8	8.0/2.6	5.3/1.8
Coefficient of friction *f*	0.19/0.15	0.16/0.14	0.18/0.15	0.15/0.14

*The numerator is without hardening, the denominator is nitriding (843 K, 75 % N_2 + 25 % Ar, 265 Pa, 4 h).

The obtained dependences of the amount of wear and the coefficient of friction of nitrided and normalized steels when working in an acidic environment on the working pressure and sliding speed. It was established that surfaces strengthened by nitriding have better tribological characteristics compared to non-strengthened ones. Recom-mendations for choosing a range of operating pressures and speeds to ensure the re-quired wear-resistant and antifriction indicators are defined.

It was experimentally determined that the temperature on the friction surfaces for the nitrided surface is significantly lower than on the surface after normalization due to the higher heat capacity of iron nitrides compared to iron. The optimal ranges of ion nitriding parameters (temperature, nitrogen content, pressure of the environment) are established, which ensure the best tribological characteristics of steels when working in an acidic environment.

It was established that the increase in stability and decrease in the coefficient of friction of steels nitrided in the glow discharge during operation in sucrose solutions occurs due to a decrease in their electrical conductivity, as well as the high lubricating properties of sucrose.

References for Chapter 2

1. Fossati, A., Galvanetto, E., Bacci, T. & Borgioli, F. (2011). Improvement of corrosion resistance of austenitic stainless steels by means of glow-discharge nitriding., 29 (5–6). Pp. 209–221. https://doi.org/10.1515/CORRREV.2011.004

2. Borgioli, F., Galvanetto, E., Bacci, T. Surface Modification of Austenitic Stainless Steel by Means of Low Pressure Glow-Discharge Treatments with Nitrogen. Coatings. 2019; 9 (10): 604. https://doi.org/10.3390/coatings9100604.

3. Semenov, M. Y., Kai, J. D., Smirnov, A. E. et al. Use of Glow Discharge Nitriding for Raising the Surface Hardness of Bearing Parts from Precision Nickel Alloys. Met Sci Heat Treat 61. Pp.173–177 (2019). https://doi.org/10.1007/s11041-019-00396-0

4. Stechyshyn, M. S., Martynyuk, A. V., Bilyk, Y. M. et al. Influence of the Ionic Nitriding of Steels in Glow Discharge on the Structure and Properties of the Coatings. Mater Sci 53. Pp.343–350 (2017). https://doi.org/10.1007/s11003-017-0081-z

5. Mashovets, N. S., Pastukh, I. M., Voloshko, S. M. Aspects of the practical application of titanium alloys after low temperature nitriding glow discharge in hydrogen–free–gas media. Appl. Surf. Sci., 392 (2017). Pp. 356–361.

6. Stechyshyn, M. S., Stechyshyna, N. M. & Kurskoi, V. S. Corrosion and Electrochemical Characteristics of the Metal Surfaces (Nitrided in Glow Discharge) in Model Acid Media. Mater Sci 53. Pp. 724–731 (2018). https://doi.org/10.1007/s11003-018-0129-8

7. Ignatov, D. Y., Lopatin, I. V., Denisov, V. V., Koval, N. N., Ahmadeev, Y. H. Generation of Plasma in Non-Self-Sustained Glow Discharge With Hollow Cathode for Nitriding Inner Surfaces of Elongated and Complex Shaped Cavities. In IEEE Transactions on Plasma Science, 48 (6), 2050–2059, June 2020, doi: 10.1109/TPS.2020.2996739.

8. Dykha, A., Makovkin, O. 2019 J. Phys.: Conf. Ser. 1172 012003. doi:10.1088/1742-6596/1172/1/0120031.

9. Khusainov, Y. G., Ramazanov, K. N. Local Ion Nitriding of Martensitic Structural Steel in Plasma of Glow Discharge with Hollow Cathode. Inorg. Mater. Appl. Res. 10, 544–548 (2019). https://doi.org/10.1134/S207511331903016X

10. Metel, A., Grigoriev, S., Melnik, Y., Volosova, M., Mustafaev, E. Surface Hardening of Machine Parts Using Nitriding and TiN Coating Deposition in Glow Discharge. Machines. 2020; 8(3):42. https://doi./org/10.3390/machines8030042.

11. Pastukh, I. M. Subprocesses accompanying nitriding in a glow discharge. Tech. Phys. 59. Pp. 1320–1325 (2014). https://doi.org/10.1134/S1063784214090205

12. Dykha, A. V., Zaspa, Y. P. & Slashchuk, V. O. Triboacoustic Control of Fretting. J. Frict. Wear 39, 169–172 (2018). https://doi.org/10.3103/S1068366618020046

13. Kaplun, P. V., Dykha, O. V. & Gonchar, V. A. Contact Durability of 40Kh Steel in Different Media After Ion Nitriding and Nitroquenching. Mater Sci 53, 468–474 (2018). https://doi.org/10.1007/s11003-018-0096-0

14. Marchenko, D. D., Dykha, A. V., Artyukh, V. A. et al. Studying the Tribological Properties of Parts Hardened by Rollers during Stabilization of the Operating Rolling Force. J. Frict. Wear 41 (2020). Pp. 58–64.

15. Inal, O. T., & Robino, C. V. (1982). Structural characterization of some ion-nitrided steels. Thin solid films, 95(2). Pp. 195–207.

16. Pokhmurs'kyi, V. I., Zin', I. M., Student, M. M. et al. Improvement of the Anticorrosion Properties of a Working Emulsion of Mine Hydraulic Systems. Mater Sci 53 (2018). Pp. 569–575.

17. Stechyshyn, M. S., Oleksandrenko, V. P., Martyniuk, A. V. Corrosion-mechanical wear resistance of food production equipment parts: study guide for students. special "Equipment of processing and food industries" [in Ukrainian]. Khmelnytskyi : KhNU, 2015. 127 p.

18. Steller, K., Krzusztolowicz, T., Reymann Z. ASTM STP 567. 1974. 152 p.

19. Hutchings, I. M. A model for the erosion of metals by spherical particles at normal incidence, Wear, Vol. 70, Issue 3 (1981). Pp. 269–281.

20. Moholkar, Vijayanand S.; Pandit, Aniruddha B. (1997). "Bubble Behavior in Hydrodynamic Cavitation: Effect of Turbulence". AIChE Journal. 43 (6). Pp. 1641–1648.

21. Nekoz A. I. Development of methods for assessing and improving the durability of food industry equipment parts subject to cavitation-erosive wear [in Russian] : Abstract of the thesis. for the scientific degree of Doctor of Engineering. Sciences. 05.02.14. Kyiv, 1985. 43 p.

22. Durability of food industry equipment parts with corrosion and mechanical wear [Text] : thesis... Dr. Tech. Sciences: 05.02.04 / M. S. Stechyshyn ; Podolia University of Technology. Khmelnytskyi (1998). 347.l. Pp. 303–329.

23. Preece, C. M., Macmillan, N. H. Erosion. Annual Review of Materials Science (1977). 7:1. Pp. 95–121.

24. Callister, Jr., William D. (2000). Materials Science and Engineering – An Introduction (5th ed.). John Wiley and Sons. ISBN 978-0-471-32013-5.

25. Sologub, N. A. Forecasting and improving the durability of parts of technological equipment of sugar factories [in Russian] : dis. … doc. tech. Sciences. Kyiv, 1993. 57 p.

26. Pogodaev, L. I., Shevchenko, PA. Hydroabrasive and cavitation wear of ship equipment [in Russian]. L. : Shipbuilding, 1984. 264 p.

27. Stechyshyn M. Development and research of vacuum-diffusion gasradiological technologies in khmelnytskui national university / M. Stechyshyn, V. Oleksandrenko, G. Sokolova, Yu Bilyk // Actual problems of modern science. Monograf. (2017). Pp. 349–356.

28. Arola, D., Alade, A. E., & Weber, W. (2006). Improving fatigue strength of metals using abrasive waterjet peening. Machining science and technology, 10 (2). Pp. 197–218.

29. Stechyshyn, M. S., Oleksandrenko, V. P., Bilyk, Yu. M. Corrosion and corrosion protection: a study guide [in Ukrainian]. Khmelnytskyi : Khnu, 2015. 197 p.

30. Karpenko, G. V. Influence of environment on strength and durability of metals [in Russian]. Publishing house : Kyiv : Naukova Dumka, 1976.

31. Shevelya, V. V., Oleksandrenko, V. P. Tribochemistry and rheology of wear resistance [in Russian]. Monograph. Khmelnitsky : KhNU, 2006. 278 p.

32. Robinson, M. I. Hammit, F. G. Trans. ASME, Ser. D, 89. 1976. 161 p.

33. Kanel, G. I., Razorenov, S. V., Utkin, A. V., & Grady, D. E. (1996, May). The spall strength of metals at elevated temperatures. In AIP Conference Proceedings (Vol. 370, No. 1. Pp. 503–506). American Institute of Physics.

34. Stechyshyn, M. S., Berehovy, A. I., Berehovy, I. M. The influence of thermocycling on the physical, mechanical and tribological characteristics of structural steels [in Ukrainian]. Probl. friction and wear. 2009. Issue 51. Pp. 53–62.

35. Stechyshyn, M. S., Stechyshina, N. M., Martyniuk, A. V. Cavitation-erosion wear resistance of milk factory equipment parts: monograph [in Ukrainian]. Khmelnytskyi : KhNU (2018). 148 p.

36. Stechishin, M. S., Nekoz, A. I., Pogodayev, L. I., Protopopov, A. S. Regularities of cavitation-erosional wearing of metals in corrosion media. Frict. Wear (1990) Pp. 384–392.

37. Trush, V. S., Lukianenko, O. H. & Stoev, P. I. Influence of Modification of the Surface Layer by Penetrating Impurities on the Long-Term Strength of Zr – 1 % Nb Alloy. Mater Sci 55, 585–589 (2020). https://doi.org/10.1007/s11003-020-00342-z.

38. Pohrelyuk, I. M., Padgurskas, J., Tkachuk, O. V. et al. Influence of Oxynitriding on Antifriction Properties of Ti–6Al–4V Titanium Alloy. J. Frict. Wear 41 (2020). Pp. 333–337.

39. Dykha, A., Makovkin, O. Physical basis of contact mechanics of surfaces (2019) Journal of Physics: Conference Series, 1172 (1), art. no. 012003. doi: 10.1088/1742-6596/1172/1/012003.

40. Pohrelyuk, I. M., Padgurskas J., Lavrys S. M., et al. Topography, hardness, elastic modulus and wear resistance of nitride on titanium, Proceedings of BALTTRIB’2017 edited by prof. J. Padgurskas. Pp. 41–46. doi:10.15544/balttrib.2017.09.

41. Stechyshyn, M. S., Skyba, M. E., Student, M. M. et al. Residual Stresses in Layers of Structural Steels Nitrided in Glow Discharge. Mater Sci 54. Pp. 395–399 (2018). https://doi.org/10.1007/s11003-018-0197-9

42. Fedirko, V. N., Luk’yanenko, A. G. & Trush, V. S. Solid-Solution Hardening of the Surface Layer of Titanium Alloys. Part 2. Effect on Metallophysical Properties. Met Sci Heat Treat 56 (2015). Pp. 661–664. https://doi.org/10.1007/s11041-015-9818-1.

43. Stechyshyna, N. M., Stechyshyn, M. S., Oleksandrenko, V. P. et al. Influence of the Power Parameters of Hydrogen-Free Nitriding in Glow Discharge on the Physicochemical Properties of 40Kh Steel. Mater Sci 57, 484–491 (2022). https://doi.org/10.1007/s11003-022-00569-y.

44. Dykha, A. V., Zaspa, Y. P. & Slashchuk, V. O. Triboacoustic Control of Fretting. J. Frict. Wear 39, 169–172 (2018). https://doi.org/10.3103/S1068366618020046.

45. Marchenko, D. D., Dykha, A. V., Artyukh, V. A. et al. Studying the Tribological Properties of Parts Hardened by Rollers during Stabilization of the Operating Rolling Force. J. Frict. Wear 41, 58–64 (2020). https://doi.org/10.3103/S1068366620010122.

46. Dykha, A. V., Kuzmenko, A. G. Distribution of friction tangential stresses in the Courtney-Pratt experiment under Bowden’s theory. J. Frict. Wear 37, 315–319 (2016). https://doi.org/10.3103/S1068366616040061.

47. Borgioli, F., Galvanetto, E., Bacci, T. Surface Modification of Austenitic Stainless Steel by Means of Low Pressure Glow-Discharge Treatments with Nitrogen. Coatings 2019, 9 (10), 604. https://doi.org/10.3390/coatings9100604

48. Khusainov, Y. G.; Ramazanov, K. N. Local Ion Nitriding of Martensitic Structural Steel in Plasma of Glow Discharge with Hollow Cathode. Inorg. Mater. Appl. Res. (2019). 10. Pp. 544–548.

49. Metel, A., Grigoriev, S.. Melnik, Y., Volosova, M. Mustafaev, E. Surface Hardening of Machine Parts Using Nitriding and TiN Coating

Deposition in Glow Discharge. Machines. 2020, 8 (3), 42. https://doi.org/10.3390/machines8030042

50. Khoma, M. S., Korniy, S. A., Vynar, V. A. et other. Influence of Hydrogen Sulfide on the Carbon-Dioxide Corrosion and the Mechanical Characteristics of High-Strength Pipe Steel. Mater Sci 2022, 57. Pp. 805–812. https://doi.org/10.1007/s11003-022-00610-0

Chapter 3.

COMPUTATIONAL AND EXPERIMENTAL EVALUATION OF TRIBOLOGICAL PARAMETERS OF FRICTION PAIRS

3.1. Influence of lubrication on the friction and wear of car rolling bearings

Most of the contact conditions for machine parts are internal or external cylinder contact. The internal contact of the cylindrical parts of the shaft and the hole can be either with a gap or with an interference fit. In this paper, machine units are considered in which a solid cylinder contact with a hollow cylinder in a different fit and the surfaces of the cylinders roll over each other with slipping. Such machine units include: the connection of the rolling bearing rings with the shaft; key connections; wave transmission; contact in needle bearings. The types and mechanisms of wear of cylindrical couplings operating in rolling conditions with slip are common. The friction path may be small for small gaps and large enough for large gaps. In the case of a small friction path surface damage is observed in the form of fretting corrosion. In the case of a long and continuous friction path, normal wear is observed. The definition of contact pressures is based on the contact mechanics of contact surfaces. At the same time, not enough attention is paid to methods for determining the friction path or the magnitude of slip in contact. The goal of the work is to develop computational and experimental approaches to determine the wear resistance of friction units with internal contact of cylinders with slip. In this study, it is proposed to take into account the slip values when calculating the actual friction path and the total wear of the cylinders with internal contact and the proposed method for identifying the parameters of the wear law based on the results of laboratory tests. The proposed approaches make it possible to determine the effect of load, slip and lubrication conditions on the durability of the friction unit by the wear criterion.

Much attention is paid to the study the problems of rolling friction in cylindrical tribosystems. Thus, in [1] the effect of rolling resistance force, sample rotation speed and loading on wear is investigated. A mathematical model has been obtained that makes it possible to predict the wear of a friction pair under rolling friction conditions. The papers [2–3] study the role of the slip coefficient in the development of cracks and fatigue life of rail materials. The results show that the slip coefficient has an important influence on the wear of materials. The article [4] presents models for calculating the speed of the rollers of a cylindrical roller bearing. It was found that the slip of rollers depends on the bearing design, load, shaft speed, lubricant properties and temperature. In [5] on the basis of dynamic analysis of rolling bearings, differential equations of a cylindrical roller bearing are established. The influence of relative slip, sliding friction coefficients and residual stresses on the distribution of shear stresses are analyzed in paper [6]. In article [7] a bearing with turbulent lubrication is considered. The simulation results are in good agreement with the experimental data. In [8] it is noted that the powder lubricants are effective, despite the increased friction indicators compared to liquid oils. This article [9] provides an equation for calculating the frictional moment of a dry lubricated tapered roller bearing, which takes into account the misalignment of the rollers. A torque model to optimize bearing design has been developed. The papers [10–13] consider the modeling of friction and wear during rolling with slip. Thus Numerical simulation of single surface irregularities passing through lubricated rolling contacts during sliding is carried out in [10]. Phenomena have been found to explain how the roughness moves through the contact and lubricates it by sliding. In [11–12] new models of rolling bearing durability are proposed. Load capacity equations have been written for both point and line contacts. The value of the empirical constant of the ball bearing has been determined based on the regression analysis of the experimental data. In the article [13], a method for determining the equivalent stiffness for bearing devices with self-elimination of the gap has been implemented. In addition, a linear model has been proposed, taking into account the effect of contact on the vibration mode and rotor frequency. Simulations and experiments have been performed to test the effectiveness of the stiffness identification method. In works [14–15] models of bearing wear are proposed and methods of identifying the parameters of these models are described.

Thus, the determination of the amount of slip during rolling of cylinders is one of the important problems of contact mechanics and tribology in general. Without knowing the amount of slip, it is impossible to simulate the wear of rolling bearings. Known studies have not provided a calculation method for assessing the amount of slip during cylinder contact. Taking this into account, the only correct thing is to determine the slip value only experimentally.

The problem of describing the rolling slip process is one of the most difficult in contact mechanics. Note that almost all variants of rolling mechanisms relate to external contact of cylinders or balls. Let us consider the case of internal rolling of cylinders that are not connected to each other in the tangential direction (Fig. 3.1, *a*).

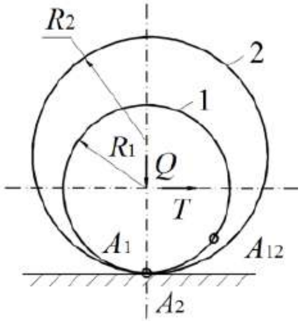

Fig. 3.1. Cylinder contact during rolling

Under the action of the forces Q and T, the outer cylinder rolls along a plane. At this time, the inner cylinder with its outer surface of radius R_1 rolls along the inner surface of radius R_2 of the outer cylinder. Let the outer cylinder, when rolling, make a full revolution $\varphi = 2\pi$ and point A_2 returned to its original position, having passed the path $S_2 = 2\pi \cdot R_2$. During this time, the inner cylinder, when rolling along the inner surface of the outer cylinder, will travel the path $S_1 = 2\pi \cdot R$ and will not return to the starting position A_1. In this case, the point A_1 will not reach the initial position by the amount of the path length ΔS:

$$\Delta s = 2\pi R_2 - 2\pi R_1 = 2\pi\Delta, \tag{3.1}$$

Next, we consider the conjugation with the gap Δ of the shaft of radius R_1 and hollow cylinder of radius R_2, connected by internal gearing with the number of teeth z (Fig. 3.1, *b*). When the cylinders are rolling internally, the teeth prevent the cylinders from sliding as in free rolling. The friction path is distributed between the teeth. When turning one tooth, the slip will be by the value:

$$s_1 = 2\pi\Delta / z. \tag{3.2}$$

With internal rolling of the shaft over a hollow cylinder, connected by a key. This connection is similar to the sliding of the teeth at z = 1: $s_k = 2\pi\Delta$. Note that formulas (3.1) – (3.2) determine the total amount of slip in the considered rolling section. In fact, there is continuous sliding throughout the entire section. Thus, it has been found that the main role for the type and value of slippage of the coupled cylinders is played by the gap between the shaft and the hollow cylinders.

In some cases, cylinders or shafts in machines rotate, and their surfaces roll over each other. As mentioned above, there are two possible cases: the inner and outer cylinders are connected by a key or pin type device; the cylinders are not connected in the circumferential direction and roll freely over each other. It is known that both in one and in the other cases, the interaction of the cylinders is worn out. Let us consider the method of testing for wear and identification of the laws of wear with internal contact of the cylinders. Experimental studies were carried out on a setup, the design of which is shown in Fig. 3.2.

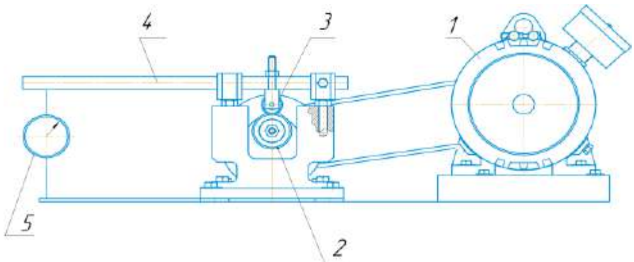

Fig. 3.2. Experimental setup

On the basis of the installation are located: engine *1* and working unit *2*, interconnected by a V-belt transmission. The load is transmitted through the bearing *3* by means of a lever *4*. The the load is controlled by an indicator *5*. The tests were carried out for two schemes of internal contact of the cylinders: connecting the cylinders with a key and without a key (Fig. 3.3). Ring *4* (52100 steel) was put on the bushing *2* (1045 steel) and fixed with a pin *3* (Fig. 3.3, *a*). The connected parts were mounted on the shaft *1* and fixed with nut *5*. Using a ball R = 2.67 mm, a hole was pressed on the outer side of the sleeve *2* to register the amount of sleeve wear. An IZA-2 optical device was used to measure the indentation diameter d. The indentation depth was determined by the formula:

$$h = d^2 / 2R. \tag{3.3}$$

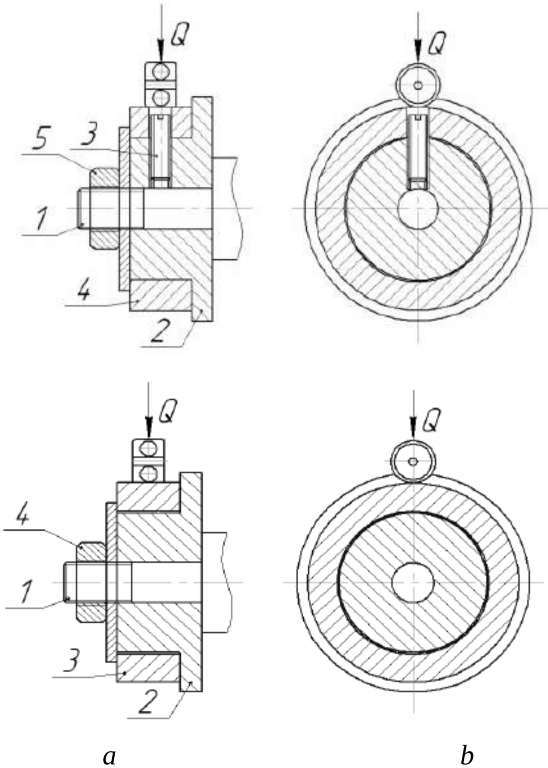

Fig. 3.3. Working unit of the installation:
***a* – with a key; *b* – without key**

The difference between the initial indentation depth h_0 and the indentation depth after testing was taken to be equal to the linear wear of the sleeve surface u_W. The friction path of two cylinders has been determined by the dependence:

$$s_1 = 2bnt, \tag{3.4}$$

where b is the contact strip half-width;
n is the part rotation frequency;
t is the time of testing.

The dimensions of the contact area with internal contact of two cylinders according to the Hertz formula:

$$b = 1.128\left(\frac{Q}{lE}\frac{R_1 R_2}{R_2 - R_1}\right)^{1/2}, \tag{3.5}$$

where Q is the part load;
R_1 is the outer radius of the sleeve;
R_2 is the inner radius of the ring;
l is the sleeve width;
E is the modulus of elasticity of the bushing material.

The tests were carried out at two loads of 100 N and 200 N. To study the effect of a lubricant on wear, three lubrication modes were used: dry contact; Fiol-3; Fiol-3 with copper powder additives (1 % by weight). The results of tests for a load of 100 N without lubricant are shown in Table 3.1. The tests were carried out with the following initial data: R = 2.67mm; n = 650 rev^{-1}; R_1 = 35mm; R_2 = 35.5mm; Δ = 0.5 mm.

Table 3.1

Test results without lubrication at a load of 100 N

t, min	d, mm	h, mm	u_w, mm	S, mm·10^5
–	1.929	0.20	–	–
100	1.83	0.159	0.008	0.3
200	1.85	0.155	0.012	0.6
300	1.83	0.152	0.015	0.9
600	1.79	0.15	0.02	1.8
900	1.75	0.144	0.025	2.5

The results have been obtained similarly for different modes of lubrication and loading. The dependence of wear on the friction path conditions is shown in Fig. 3.4 (Q = 100 N).

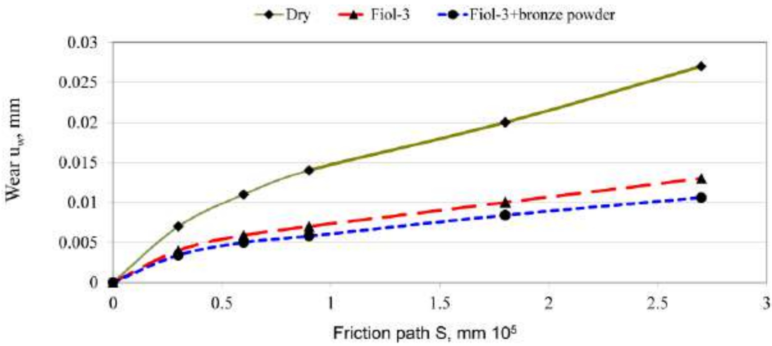

Fig. 3.4. Wear on the friction path with non-free contact of the cylinders (Q = 100 N)

Wear tests with free contact of the cylinders were carried out according to the scheme in Fig. 3.3, *b* also for two loads and three modes of contact lubrication.

The tests were carried out with the initial data: R = 2.67 mm; n = 650 rev^{-1}; R_1 = 34.7 mm; R_2 = 35.7 mm; Δ = 1 mm. The wear on the friction path with free contact of the cylinders for various lubrication conditions is shown in Fig. 3.5 (Q = 100 N).

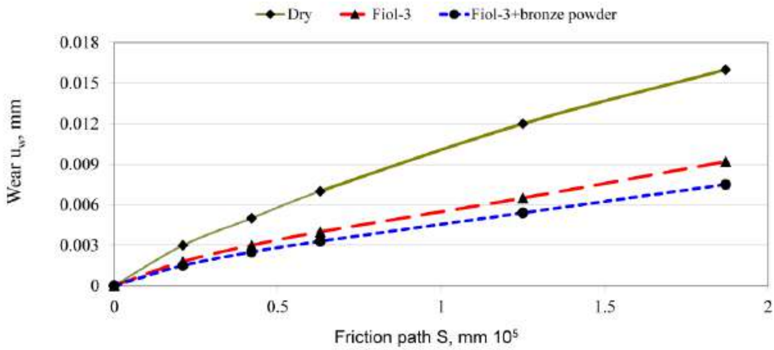

Fig. 3.5. Dependences of wear on the friction path with free contact of the cylinders (Q = 100 N)

For the analysis of the wear of machine parts, you can use a simple wear model:

$$u_w = k_w \sigma^m S, \tag{3.6}$$

where u_w is the current wear;

k_w, m are the parameters of the wear model determined from the experiment; σ is the contact pressure;

S is the friction path at wear points, determined by calculation or from experiment.

To determine the parameters of the wear law (3.6), it is proposed to use the obtained results of tests for cylinder wear under various lubrication modes. The wear law parameter m is determined by the results of the wear values and contact pressures obtained at two values of the external load: 100 N and 200 N according to the dependence:

$$m = \frac{\lg(u_{w1} / u_{w2})}{\lg(\sigma_1 / \sigma_2)}, \tag{3.7}$$

where Δu_{w1}, Δu_{w2} are the values of the wear of the part at various loads Q;

σ is the maximum contact pressure at a given load according to the Hertz formula:

$$\sigma = 0.418\left(\frac{QE}{l}\frac{R_2 - R_1}{R_1 R_2}\right)^{1/2}, \qquad (3.8)$$

Wear model parameter k_w:

$$k_w = \frac{u_{w2}}{\sigma^{m_2} S_2}. \qquad (3.9)$$

The results of wear tests and parameters of the law of wear of cylinders for various lubrication conditions are presented in Table 3.2.

Table 3.2

Results of studies of cylinders wear with slip

Lubricant	With key			Without key		
	Dry	Fiol-3	Fiol-3 + bronze	Dry	Fiol-3	Fiol-3 + bronze
b (100 N), mm	0.23	0.23	0.23	0.16	0.16	0.16
b (200 N), mm	0.32	0.32	0.32	0.23	0.23	0.23
S_{900}(100 N), mm·10^5	2.7	2.7	2.7	1.87	1.87	1.87
S_{900}(200 N), mm·10^5	3.75	3.75	3.75	2.7	2.7	2.7
σ_{100}, MPa	15			19.5		
σ_{200}, MPa	199			285		
m	1.84	2	2.04	1.8	1.76	1.78
k_w, MPa^{-1}·10^{-9}	18.4	8.85	7.2	7.1	4.3	3.52

Thus, in contrast to the known approaches, a theoretical and experimental method is proposed for determining the wear of cylinders with internal contact, taking into account the friction path from the slip value. A method for identifying the parameters of the wear law based on the results of laboratory tests is also proposed. For the further development of ideas about the mechanism of slip, it is necessary to carry out experiments to determine the slippage of uncoupled cylinders and to study experimentally the influence of interference and clearance on the amount of slippage and wear.

The task is to determine the wear of the hub shaft in the connection of the rolling ball bearing of the suspension hub of the vehicle. The initial data: load on one wheel is 3000 N; diameter of the bearing ring is d = 34 mm; ring thickness is 5 mm; the clearance Δ = 0.05 mm. The slip in the contact is taken to be equal to the value of the relative clearance: $\psi = \Delta/R = 0.003$.

The friction path in one wheel revolution: $S_1 = 2\pi R\ \psi = 0.32$. With a wheel diameter of 500 mm, the wheel makes an 640 revolutions per 1 km of run. Then the friction path for 100,000 km of run will be: $S = 0.32 \cdot 640 \cdot 100{,}000 = 2.05 \cdot 107$ mm. The calculation of the hub shaft wear was carried out to the formula (3.7). Two modes of lubrication were considered: Fiol-3 and grease with copper powder. The parameters of the wear (3.7) were taken from Table 3.2. The contact pressure was taken to be 5 MPa. The results of calculating the wear of the hub shaft are shown in Fig. 3.6.

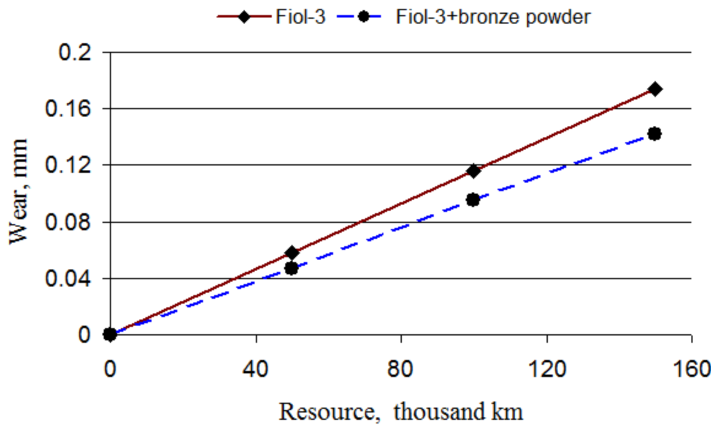

Fig. 3.6. Dependence of the hub shaft wear on the vehicle resource

The calculation results show the efficiency of using copper powder as an additive to a lubricant.

Developed a test procedure for wear during internal rolling of a cylinder. The developed technique is used to assess the effectiveness of lubricants and additives from bronze powder to increase the wear resistance of the interface. As a result of tests, it has been found that: wear of cylinders with a key is 1.35 times more than the wear of cylinders without a key, which is explained by a correspondingly large friction path; lubrication with Fiol reduces the wear of the joint by 1.81 times; lubrication with Fiol with the addition of bronze powder reduces wear in comparison with lubricant without the addition of additives by 1.2…1.8 times; the overall reduction in wear when using Fiol with bronze powder is estimated 2.3…2.1 times.

3.2. Investigation of slippage and wear in rolling bearings of machines

The main bearing unit of the machines are rolling bearings. The main causes of bearing failure are: fatigue spalling of raceways; wear of raceways; plastic deformation and creep of raceways. At present, the process of contact fatigue failure of bearings is well studied. Methods for calculating contact strength based on the solution of the contact problem according to Hertz have been developed. Test methods and definitions of damage accumulation models have been developed.

At the same time, many bearings fail due to wear rather than fatigue. This primarily applies to bearings in abrasive and high temperature conditions. There are practically no methods for calculating and testing bearings for wear, which complicates their design.

Methodology for calculations and tests for wear and reliability of bearings are the following stages.

1. The features of the design and technology of the friction unit are studied. The loads on the rolling elements are determined.

2. The contact pressures between the body and the raceway are determined.

3. The sliding path of the ball or roller along the raceway is determined.

4. Selection of a wear model and experimental determination of its parameters.

5. Solving wear-contact problems for bearing parts.

6. Calculations for bearing wear reliability using Gaussian normal distribution.

Thus, one of the main values for calculating and analyzing the process of wear of rolling friction units is the sliding friction path between the contacting bodies.

The roller bearing model in [16] was developed to evaluate cage slip, roller slip, film thickness and cage forces for a given bearing geometry and operating conditions. The model takes into account the friction of the cage guide surface, the friction of the roller pocket, and the cage unbalance. Skewed and skewed rollers were not considered. The description of the lubricating film thickness, adhesion forces and pressure is based on the solution of the isothermal problem of elastohydrodynamics.

The article [17] proposes a numerical method for determining the sliding of a cage in high-speed ball bearings with an axial load. The model agrees well with the experimental results for sliding ball bearings. The model is recommended for studying the causes of sliding in loaded ball bearings.

The influence of operating parameters on the slip of the cage in cylindrical roller bearings is considered in paper [18]. The cylindrical roller bearing test bench is designed to measure the movement of bearing elements under various operating conditions. The influence of operating parameters, namely, shaft rotation speed, radial load, lubricating oil viscosity, number of rollers and bearing temperature, on the cage sliding is obtained experimentally.

The slip of the cage and balls of ball bearings used in paper [19] for the main shafts of jet engines is evaluated. A new method has been developed for assessing slip, taking into account the increase in oil temperature caused by slip in the contacts between the ball and the raceway. The analytical results of the study were compared with experimental data.

In [20] the influence of different models of a radially loaded cylindrical roller bearing is investigated using a dynamic model of a bearing assembly. The cage rotation speed, depending on the force between the roller and the raceways, is designed for a wide range of speeds and loads. Comparison of the simulation results with the results of experimental measurements shows that the model is able to predict the operation of the rolling elements under various operating conditions.

Further modeling of sliding in rolling bearings from various points of view was also considered in papers [21–25].

Slip in ball bearings. It is known from experiments that the length of the path of a ball of a ball during rolling is not equal to the length of a circle made up of points of contact. This means that rolling occurs with slippage. In this paper, slippage is necessary to determine the sliding friction path for wear calculations. Determination of the sliding path in rolling with slip in most of the known studies was done by theoretical methods. Determination of slippage by theoretical methods leads to complex mathematical problems, the solution of which again requires simplifications and approximations. Most often, it is difficult to assess the accuracy of these solutions.

It is more rational to experimentally determine the value of the slip coefficient of bearings, taking into account various factors and apply them to other types of bearings.

Consider the basic relations for the rolling of a ball on a plane with slippage.

The rolling friction force is related to the normal load, ball radius and rolling friction coefficient by the ratio:

$$F_r = \mu_r \frac{N}{R}. \tag{3.10}$$

When the ball is rotated through an angle 2π or a full turn in the absence of slippage, the length of the contact line on the plane will be equal to the circumference of the ball:

$$l = 2\pi R. \tag{3.11}$$

In the presence of slippage, the rolling friction path will differ from the circumference by an amount Δl.

Attitude:

$$S_c = \frac{\Delta l}{l}, \tag{3.12}$$

called the slip coefficient. Experimental determination of the slip for a single ball is not difficult.

Let us assume that rolling resistance occurs due to the slipping of the ball along the plane at the points of contact. Thus, the rolling resistance due to surface deformations is neglected.

Slip resistance frictional force:

$$F_s = \mu_s N. \tag{3.13}$$

We assume that the work of rolling friction forces on the rolling path is equal to the work of sliding friction forces on the sliding path Δl:

$$W_r = W_s. \tag{3.14}$$

or

$$F_r l = F_s \Delta l. \tag{3.15}$$

Substituting (3.1) and (3.4) into (3.6), we obtain:

$$\mu_r \frac{N}{R} l = \mu_s N \Delta l \ . \tag{3.16}$$

Or, taking into account (3.3), we obtain:

$$S_c = \frac{\mu_r}{\mu_s R} \ . \tag{3.17}$$

Therefore, the coefficient of rolling slip is equal to the coefficient of rolling friction divided by the coefficient of sliding friction.

An example of a ball rolling $d = 12.3$ mm on hardened steel (Fig. 3.7).

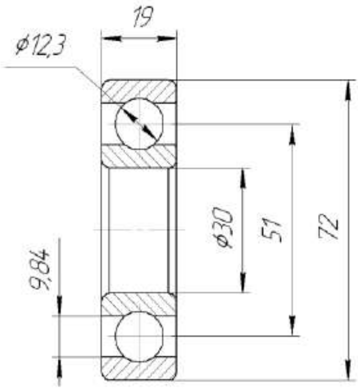

Fig. 3.7. Dimensional drawing of plain ball bearing

The rolling friction coefficient is assumed to be $\mu_r = 0.01$ mm. Sliding friction coefficient of steel on steel without lubrication $\mu_s = 0.1...0.3$.

Then:

$$S_c = \frac{\mu_r}{\mu_s R} = \frac{0.01}{(0.1...0.3)\cdot 6.15} = 0.016...0.005 \cdot$$

With a cage diameter in the bearing of $d_c = 51$ mm, the sliding friction path for the balls along the raceway per revolution is $D_s = S_c \pi d_c = (0.016...0.005)\pi \cdot 51 = 2.56...0.80$ mm.

The basis of the experimental method. The mechanics of the motion of balls in rolling bearings of machines with a slip is a complex problem in contact mechanics. The complexity is explained by the variety of ball movements: around the rotor axis; rotation around its own axis; spinning; gyroscopic motion; slippage in all contact zones.

Slip mechanics are complicated by the proximity of the ball radii and the radius of the ring track. At the same time, the calculation of rolling bearings for wear requires an accurate assessment of the sliding friction path in contact between the ball and the raceways.

A computational and experimental method is proposed for determining the amount of slip in ball bearings. The basis of the approach is as follows. From the kinematics of the bearings, precise relationships are obtained for the movements of the balls and rings without slipping. On the other hand, experimentally, you can simply measure the number of revolutions of the separator. The difference between the calculated and actual numbers of revolutions of the cage allows you to determine the average value of the ball sliding along the raceway.

The kinematics of rings and a ball in a bearing is considered under the following conditions: the inner ring rotates; the outer ring is stationary; the ball rolls over the rings without slipping. Kinematics are considered to determine the sliding friction path of a ball along the raceways.

For a bearing with a fixed outer ring, the geometric ratio is adopted:

$$V_c = \frac{1}{2} V_1 , \tag{3.18}$$

where V_c , V_1 is the linear speeds of movement of points of the separator and the inner ring V_1.

The linear speed of the ring is expressed in terms of the number of revolutions by the ratio:

$$V_1 = \frac{\pi d_1 n_1}{60} . \tag{3.19}$$

Similarly for the linear speed of the separator:

$$V_c = \frac{\pi d_c n_c}{60} = (d_1 + d_0) \frac{\pi n_c}{60} , \tag{3.20}$$

where d_c is the cage average diameter;
d_1 is the diameter of the inner ring;
n_1 is the the number of revolutions of the inner ring;
n_c is the the number of revolutions of the separator;
d_0 is the ball diameter.

After mutual substitutions and transformations, we get:

$$n_c = \frac{n_1}{2(1+d_0/d_1)}. \tag{3.21}$$

The experimental speed of the separator n_c^* differs from the theoretical speed n_c. The difference between experimental and theoretical rpm is explained by the slippage of the balls along the raceways.

With this in mind, the coefficient of slip in the rolling bearing is determined by the relationship:

$$S_c = \frac{n_c^* - n_c}{n_c^*} = 1 - \frac{n_c}{n_c^*}. \tag{3.22}$$

Installation, test procedure and results. An installation for testing rolling bearings for slip is shown in Fig. 3.2.

Carrier *1* transmits rotation with frequency *n* through pins *3* to the upper disk *4* of the working head. The load *Q* on the bearing assembly is transmitted through ball *2*. Ball *3* is fixed in a cylindrical cage *11*. A radial bearing 5 is needed to center the upper disc and the lower head housing *9*. A thrust ball bearing is tested, consisting of an upper ring *6*, a lower ring 8 and a cage *7*. The working head is attached to the table of the test bench with a nut *10*. During wear tests, the test specimen is installed in place of the lower ring of the thrust bearing. When testing for slippage when the upper ring rotates at a speed n_1, the separator *7* is simultaneously rotated at a speed n_c.

The number of revolutions of the ring and cage was measured using a DT2234B electronic digital tachometer. Foil pieces 5 × 10 mm in size were attached to the upper ring and to the separator. The beam from the tachometer periodically hits the foil and records the number of revolutions per minute accurate to the first decimal place. The measurement results are shown in Tables 3.1 and 3.2.

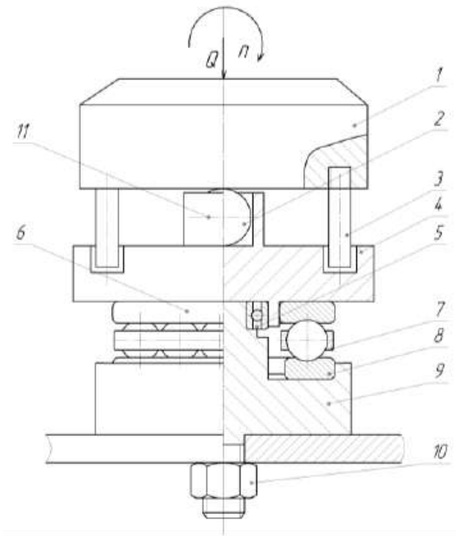

Fig. 3.8. Installation test machine for rolling bearings

Slip tests were carried out at loads Q = 100; 250; 500 N for bearing 8204. The revolutions of the upper ring were set in steps: n_1 = 250; 500; 1350 rpm.

The theoretical speed of rotation of the separator was calculated by the formula (3.18), the amount of slippage was determined by the formula (3.12). Slip tests were carried out under two lubrication modes: in the absence of lubrication and lubrication with Fiol-3 grease. The results of measurements and calculations are shown in Tables 3.3 and 3.4.

Table 3.3

Test results without lubrication

Speed, rpm	Q, N						n_0, rpm
	100	S_c	250	S_c	500	S_c	
n_1	250.2	0.0312	250.9	0.0322	250.4	0.0309	250
n_c	129.1		129.6		129.2		
n_1	497.4	0.0293	496.6	0.0312	495.9	0.0315	500
n_c	256.2		256.3		256.0		
n_1	1350	0.0321	1349	0.0320	1348	0.0317	1,350
n_c	697.4		696.8		696.1		

Table 3.4

Test results with Fiol-3 grease

Speed, rpm	Q, N						n_0, rpm
	100	S_c	250	S_c	500	S_c	
n_1	251.0	0.0331	250.5	0.0342	250.8	0.0350	250
n_c	129.8		129.7		129.9		
n_1	499.4	0.0323	498.5	0.0343	497.9	0.0335	500
n_c	258.0		258.1		257.6		
n_1	1351	0.0352	1349	0.0343	1349	0.0362	1,350
n_c	700.1		698.5		699.8		

Analysis of the results obtained shows that the slip coefficient is practically independent of the load and rotation speed. Slip fluctuations due to these factors are rather random. Average value of the slip coefficient for bearing 8204 without lubrication $S_c = 0,0313$, and when lubricated with Fiol-3 grease $S_c = 0,0342$. Thus, the use of lubricant increases slip by 8 %.

Modeling rolling bearing wear. The calculation of wear is based on the mechanics of the contact interaction of a ball and a plane with wear. The sliding of a ball on a ring (Fig. 3.9) under a load Q is considered.

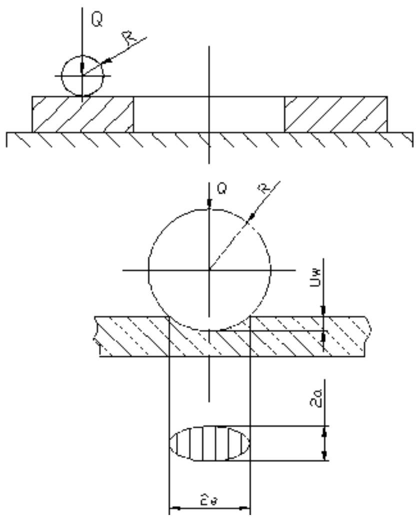

Fig. 3.9. Scheme of wear tests

The ring is stationary, the surface of the ring wears out. During the wear process, a groove with a width of *2b* is formed, which increases with wear. We assume that the ball does not wear out.

Ring wear model in differential form:

$$\frac{dU_w}{ds} = k_w \left(\frac{\sigma}{HB} \right)^m \left(\frac{\upsilon R}{\nu} \right); \tag{3.23}$$

or in the form:

$$\frac{dU_w}{ds} = k_w \sigma^m \ddot{I} \ , \ \ \ddot{I} = \left(HB \right)^m \left(\frac{\upsilon R}{\nu} \right),$$

where σ is the contact pressure; k_w, m are the parameters of the wear model;

U_w is wear;

s is the friction path for ring.

HB is Brinell ring material hardness;

υ is the relative sliding speed;

R is the radius of the ball;

ν kinematic viscosity of the lubricant.

In the process of wear, a platform is formed with dimensions: *2a* along the friction path and *2b* across the friction path. We assume that the contact pressure is evenly distributed over the contact area:

$$\sigma = \frac{Q}{\pi ab}. \tag{3.24}$$

The depth of the wear groove U_w is related to the width of the groove and the radius of the ball in the ratio:

$$U_w = \frac{b^2(s)}{2R}. \tag{3.25}$$

The friction path s for ring points is related to the size of the contact area in the sliding direction by the ratio:

$$s = 2azntS_c, \tag{3.26}$$

where z is the number of balls passing through the contact area, per revolution; n is the number of revolutions per minute; t is the duration of the bearing; S_c is the slip value.

The size a of the contact area can be determined by the Hertz formula:

$$a = 1{,}09\sqrt[3]{\left(\frac{QR}{E}\right)}, \tag{3.27}$$

where E is the modulus of elasticity of the ring material.

The main assumption is that the size of the contact area in the direction of motion of the ball is taken to be equal to the initial size a according to (3.28).

Differentiating equation (3.16) and substituting in (3.14) after transformations, we obtain the differential equation of the problem:

$$\frac{Q}{\pi ab} = \left(\frac{b}{Ï\ k_w R} \cdot \frac{db}{ds}\right)\frac{1}{m}. \tag{3.28}$$

The solution of the differential equation (3.30) with a zero initial area b = 0 gives an expression for determining the size of the wear area of the bearing ring $b(s)$:

$$b = \left((m+2)\left(\frac{Q}{\pi a}\right)^m Ï\ k_w RS\right)^{\frac{1}{m+2}}. \tag{3.29}$$

The inverse problem consists in determining the parameters of the bearing ring wear model k_w and m for the function $b(s)$ known from the experiment. Based on the test results, this function can be represented as a power-law approximation:

$$b(s) = cs^{\beta}. \tag{3.30}$$

Then equation (3.20) can be represented in the form:

$$\frac{c^{m+2} S^{\beta m + 2\beta}}{m+2} = \left(\left(\frac{Q}{\pi a}\right)^m Ï\ k_w RS\right). \tag{3.31}$$

From the condition that this equation is satisfied, we obtain:

$$\beta m + 2\beta = 1 \tag{3.32}$$

or

$$m = \frac{1 - 2\beta}{\beta}. \tag{3.33}$$

Taking into account (3.33), from (3.32) it follows:

$$k_w = \frac{c^{m+2}}{(m+2)} \left(\frac{\pi a}{Q} \right)^m \mathit{\Pi} R. \tag{3.34}$$

Thus, a generalized solution of the contact problem of the interaction of a ball and a bearing ring during ring wear is proposed. At the same time, an approximate solution of the problem of ring wear by a ball is carried out under the assumption of a slight change in the size of the contact area in the direction of the ball movement.

As a result of the conducted research, conclusions can be drawn:

1. The main bearing unit of modern machines is rolling bearings. There are practically no methods for calculating and testing bearings for wear, which complicates their design.

2. A computational and experimental method for determining the amount of slippage in ball bearings is proposed. From the kinematics of bearings, relations for the movements of balls and rings without slipping are known; on the other hand, the number of revolutions of the separator can be measured experimentally. The difference between the calculated and actual numbers of revolutions of the separator allows you to determine the amount of slip.

3. Analysis of the results obtained shows that the slip coefficient does not depend on the load and rotation speed. Slip fluctuations due to these factors are random. The use of lubricant increases slip by 8 %.

4. The solution of the wear contact problem for the ball and bearing ring in case of wear of the ring has been carried out. An approximate solution of the problem of ring wear by a ball is carried out under the assumption that the contact area remains unchanged in the direction of the ball movement.

3.3. Wear and reliability of cylindrical vehicle joints

The suspension is one of the most important parts of a car in terms of the comfort of transportation of goods and passengers and, most importantly, in terms of traffic safety. Wear of friction units is the main reason for the decrease in suspension reliability. The suspension structure of the front wheels of a car contains many important friction units. Among these supports, the most important are ball bearings. These bearings have different friction pairs: steel on steel, steel on polymers, steel on rubber, etc. The study of the support structure is the first mandatory stage of calculations and tests for wear and reliability of friction units. It is also necessary to understand how the construction of the assembly works, as well as to understand the entire subsequent calculation methodology. Analysis of the design of ball joints of different cars allows us to trace the tendencies of their improvement. Suspension ball joints are applied between control arms and wheel carriers or knuckles of the suspension that allow relative articulation and rotation between the mating components. Depending on its application, the ball joint can transmit longitudinal and lateral forces with only a small proportion of forces as well as the complete vehicle weight in vertical direction. Much attention is currently paid to the study of the tribological aspects of extending the service life of the movable joints of a car [26]. At the same time, a comprehensive study of analytical and experimental methods for predicting the resource of vehicle friction units is an actual problem.

Calculation of wear and contact pressures in ball bearings of a vehicle suspension. To determine the effectiveness of construction and lubricants used in transport, a calculation method is proposed for determining the wear of vehicle parts. The technique takes into account the properties of materials and the operating conditions of the friction unit and makes it possible to determine the durability of the friction unit by the wear criterion. The basis is the solution of the wear contact problem for a given contact pattern of parts.

In this case, the design of the ball joint of the car suspension is considered. In the ball joint, there is a contact interaction of a rigid spherical liner and a rigid cage according to the scheme in Fig. 3.10. A ball bearing of radius R rotates around its axis along the body and wears out. It is necessary to obtain the dependence of the wear of the mating of the axes of the main factors. The angle of the liner ranges from $\varphi = \varphi_1$ to $\varphi = \varphi_2$.

The mathematical formulation of the problem consists of an equilibrium condition, a geometric relationship, and a wear law.

The equilibrium condition for a spherical joint is:

$$Q = 2\pi R^2 \int_{\varphi_1}^{\varphi_2} \sigma(\varphi)\cos\varphi d\varphi, \tag{3.35}$$

where $\sigma(\varphi)$ is the required pressure function.

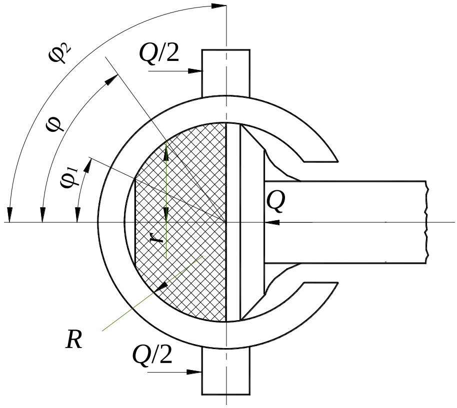

Fig. 3.10. Design scheme of the hinge

The geometric dependence of displacements u_0 on wear $u_w(\varphi)$ is as follows:

$$u_w(\varphi) = u_0 \cos\varphi. \tag{3.36}$$

The wear law with two parameters k_w and *m* is taken as:

$$\frac{du_w}{dt} = k_w \sigma^m 2\pi n r \tag{3.37}$$

where *n* is the number of vibrations of the hinge per unit time *t;* $r = R\cos\varphi$.

As a result of differentiating condition (3.37) and equating (3.37), we obtain:

$$k_w \sigma^m 2\pi n R^2 \cos\varphi = \frac{du_0}{dt}\cos\varphi, \tag{3.38}$$

from here we have:

$$\sigma = \left(\frac{du_w}{dt}\right)^{\frac{1}{m}} \left(\frac{1}{k_w 2\pi n R^2}\right)^{\frac{1}{m}}. \tag{3.39}$$

As a result of mutual substitutions, we obtain the resolving integral equation of the problem:

$$Q = 2R\left(\frac{du_w}{dt}\right)^{\frac{1}{m}}\left(\frac{1}{k_w 2\pi n R^2}\right)^{\frac{1}{m}}\int\limits_{\varphi_1}^{\varphi_2}\cos\varphi\sin\varphi d\varphi . \qquad (3.40)$$

After integration, we obtain the dependence for the maximum wear:

$$u_w(t) = \left(\frac{Q}{\pi R^2}\right)^m \frac{k_w 2\pi R n}{(\sin^2\varphi_2 - \sin^2\varphi_1)^m} t . \qquad (3.41)$$

If we take the friction path for one cycle s_1, then for the time t the total friction path is: $s = s_1 nt$ or $nt = \frac{s}{s_1}$. As a result, for the friction path we get:

$$u_w(s) = \left(\frac{Q}{\pi R^2}\right)^m \frac{k_w 2\pi R^2 s}{\sin^2\varphi_2 - \sin^2\varphi_1} . \qquad (3.42)$$

The formula for determining the contact pressure is obtained by substituting (3.43) in (3.40):

$$\sigma = \left(\frac{Q}{\pi R^2}\right)\frac{\left(k_w 2\pi R^2 n\right)^{\frac{1}{m}}}{\sin^2\varphi_2 - \sin^2\varphi_1}\left(\frac{1}{k_w 2\pi n R^2}\right)^{\frac{1}{m}} . \qquad (3.43)$$

After the transformations, we finally get:

$$\sigma = \frac{Q}{\pi R^2\left(\sin^2\varphi_2 - \sin^2\varphi_1\right)} . \qquad (3.44)$$

An example of calculating the wear of the lower support in the contact of a hardened steel shaft and a polyurethane polymer liner.

Initial data. Hinge load 2,000*N*. The total path of friction in the joint for 10,000 km of run. Ball pin radius 16 mm. The parameters of the wear model for polyurethane are: m = 2.04; $k_w = 0.5\cdot 10^{-8}$ (MPa) $^{-m}$. Liner contact angles: $\varphi_1 = 35^\circ$; $\varphi_2 = 85^\circ$.

The calculation of the wear of the liner is performed according to dependence (3.42) with the selected initial data per 10,000 km of run:

$$u_w = \left(\frac{Q}{\pi R^2}\right)^m \frac{k_w 2\pi Rs}{\sin^2\varphi_2 - \sin^2\varphi_1} =$$

$$= \left(\frac{2000}{\pi 15^2}\right)^{2{,}04} \frac{0.5\cdot 10^{-8}\cdot 2\pi\cdot 16^2\cdot 3\cdot 10^4}{\sin^2 85^0 - \sin^2 35^0} = 0.233\,\text{mm}.$$

The obtained dependencies for calculations of wear are valid for all ball bearings of the front suspension. The difference lies in the different values of the contact angles φ_1 and φ_2. The formula for calculating contact pressures is also common to all mates in ball joints. This calculates the wear due to the frictional path caused by the axial rotation of the ball pin during the rotation of the steering knuckle when turning from the steering. The friction path from lowering and raising the wheels while driving must be added to the total friction path in accordance with the suspension kinematics.

The maximum initial contact pressure in the hinge is determined by the dependence (3.45):

$$\sigma = \frac{Q}{\pi R^2\left(\sin^2\varphi_2 - \sin^2\varphi_1\right)} = \frac{2{,}000}{\pi 15^2\left(\sin^2 85^0 - \sin^2 35^0\right)} = 3.95\,.$$

It has been established that this value of contact pressure does not change with wear of the liner.

Contact pressure is the main, basic characteristic of the friction unit. To determine pressures, it is necessary to have a solution corresponding to the contact problem. The upper and lower supports each have two types of spherical couplings, which differ both in the sign of curvature and in the properties of the contacting bodies. However, all mates can be represented as one generalized mate: the convex spherical surface of the finger and the concave spherical surface of the support body (or vice versa). In all cases, contact starts at some angle $\varphi_1 > 0$ and ends at an angle $\varphi_2 \le 90^o$.

Reliability calculations of ball bearings. Let us assume that the current wear of the suspension ball bearings is distributed according to the normal law. In this case, the quantile up of the reliability function is determined [28] by the dependence:

$$u_p = -\frac{n-1}{\left(n^2 V_{w*}^2 + V_w^2\right)^{\frac{1}{2}}}(\varphi). \tag{3.45}$$

where V_{w*}, V_w is variation coefficients of limit and current wear; where n is safety factor for wear:

$$n = \frac{u_w^*}{u_w} \tag{3.46}$$

The limit wear value can be taken constant $u_w^* = 0$, then the variation coefficient $V_{w*} = 0$. In this case, from (3.46) we have:

$$u_p = -\frac{n-1}{V_w} \tag{3.47}$$

By quantile, the reliability function is determined by the Laplace function: $\phi\left(u_p\right)$:

$$P\left(u_w < u_w^*\right) = 0.5 + \phi\left(u_p\right). \tag{3.48}$$

The determination of the general variation coefficient is performed through the partial coefficients of variation, taking into account the form of the main dependence (3.41).

The determination of the general variation coefficient is performed through the partial variation coefficients, taking into account the form of the main dependence (3.41).

In this case, the load, the wear rate factor and the friction path are random values. The variation coefficients for these quantities V_Q, V_{k_w}, V_s are assumed to be known.

In accordance with the general methodology [27] determining the coefficient of variation of a function by the variation coefficients of the arguments, we have:

$$V_w = \left(m^2 V_Q^2 + V_{k_w}^2 + V_s^2\right)^{\frac{1}{2}}. \tag{3.49}$$

Let us determine the probability of failure-free operation of the ball joint of the car during 10,000 km of run. Let's use the initial data from the previous example. Let us take the coefficients of variation: $V_Q = 0.4$, $V_S = 0.4$, $V_{K_W} = 0.35$.

The general coefficient of variation of wear is determined by the dependence (3.41):

$$V_{u_w} = \left(m^2 V_Q^2 + V_{k_w}^2 + V_s^2\right)^{\frac{1}{2}} = \left(2.04^2 0.4^2 + 0.35^2 + 0.4^2\right)^{\frac{1}{2}} = 0.98;$$

A verage wear is determined by the formula (3.48). According to the accepted data, the wear of the ball joint was obtained for 10,000 km. $u_w = 0.233$ mm.

According to [28], if, when checking the wear in the upper ball joint, the total indicators of the indicator exceed 0.8 mm, then the hinge must be repaired. Thus, dividing this value into two joints (lower and upper) we obtain the allowable wear value in the ball joint of the front suspension: $u_w^* = 0.3$ mm. Safety factor: $n = \frac{u_w^*}{u_w} = \frac{0.3}{0.233} = 1.85$.

The quantile of the probability of no-failure operation is determined by the dependence (3.48):

$$u_p = -\frac{n-1}{V_w} = -\frac{1{,}85-1}{0{,}98} = -0.867.$$

According to the tables of the Laplace function: $\phi(-0.867) = 0.3078$. Finally, reliability function according to (3.48): $P = 0{,}5 + \phi\left(u_p\right) = 0.5 + 0.3078 = 0.8078$.

The given example is methodological in nature. For a more reliable assessment of reliability, it is necessary to perform an experimental determination of both the average values and their coefficients of variation.

Determination of wear parameters of ball bearings. In the calculation formulas, the wear parameters *m* and k_w were taken as given. The problem of determining the parameters of the friction pair wear model is one of the stages of the computational and experimental evaluation of the wear of the ball joints. The problem of increasing the wear resistance of this unit can be solved in two directions: improving the wear-resistant properties of the liners and choosing new types of lubricants. Currently, great progress has been made in the development of lubricants with additives. The task is to assess the effectiveness of lubricants for use in ball joints. The wear characteristics of the materials were determined from the results of wear tests. The test scheme is shown in Fig. 3.11. An automobile ball joint polyurethane liner was used as a sample. The outer surface of the insert was tested with loading with a sphere diameter R = 28 mm (Fig. 3.11).

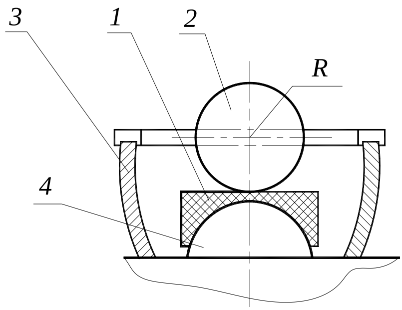

Fig. 3.11. Scheme of testing the polyurethane liner for wear:
1 **– polyurethane hinge liner;** ***2*** **– steel counter sample HRC 50;**
3 **– container with grease;** ***4*** **– loading arm**

The tests were carried out at a rotational speed $n = 830\ rev^{-1}$ and a load of 10 N. For lubrication, we used: ShRB-4 grease, Mobil grease, Shell grease. Three samples of each variant were tested. The contact patch was measured in two directions. The average test results are presented in Table 3.5.

Table 3.5

Test results of polyurethane with different types of lubricants

Friction path s 10^6, mm	*a*, mm			
	without lubrication	Shrb-4	Mobil	Shell
1	1,44	1,211	1,201	1,240
3	1,52	1,46	1,33	1,335
5	1,665	1,511	1,432	1,38
8	1,71	1,58	1,49	1,50
10	1,802	1,715	1,575	1,585

The test results were approximated by a power function of the dependence of wear on the friction path in the form: $a = cs^{\beta}$. The power-law approximation parameters were determined using the Excel program (Table 3.6).

Table 3.6

Results of determining wear parameters for various lubricants

Parameters	Without lubrication	ShRB-4	Mobil	Shell
β	0.105	0.14	0.118	0.14
c	0.33	0.25	0.269	0.295
m	3.65	3.15	3.52	3.34
k_w	$13.4\cdot10^{-6}$	$0.425\cdot10^{-6}$	$0.38\cdot10^{-6}$	$0.425\cdot10^{-6}$
I(7 MPa)$\cdot10^{-6}$	2.175	0.0827	0.064	0.0745
I(2 MPa)$\cdot10^{-6}$	0.0378	0.0029	0.00156	0.00175

The formulas for determining the wear parameters were determined by solving the inverse wear-contact problem [29]. Relationships (3.35) – (3.38) were used as the basic equations. As a result, we got the formulas:

$$m=\frac{1-2\beta}{2\beta}. \tag{3.50}$$

$$k_w=\frac{c^{2m+2}}{(2m+2)(Q/\pi)^m R}. \tag{3.51}$$

The results of calculating the wear parameters are shown in Table 3.6. Comparison of the effectiveness of lubricants is carried out in terms of the wear rate at two pressures of 7 MPa and 2 MPa. The calculation of the intensity is carried out according to the main dependence:

$$I=\frac{du_w}{ds}=k_w\sigma^m. \tag{3.52}$$

The results of calculating the wear rate for various lubricants are shown in Table 3.6. From the results of comparison with the base grease ShRB-4 it follows: the use of Mobil grease reduces wear at 7 MPa by 1.2 times; at 2 MPa by 1.79 times; the use of Shell lubricant reduces wear at 7 MPa by 1.15 times; at 2 MPa, 1.70 times.

Conclusion:

1. To estimate the wear of the ball joints of the car suspension, the wear-contact problem was solved. The solution is based on: the

equilibrium equation of the tribosystem, the law of wear, the geometric equation of continuity in contact. As a result, closed formulas were obtained for determining the amount of wear and contact pressure.

2. A method is proposed for calculating the reliability of ball joints of a car half-suspension by the criterion of wear. A method of sequential calculation of the coefficient of variation of wear is considered by the coefficients of variation of random parameters that are included in the formula for calculating wear.

3. Based on the solution of the inverse wear-contact problem, formulas are proposed for calculating the parameters of the wear law. A comparative assessment of the tribological properties of lubricants for ball joints of the car suspension is carried out.

3.4. Wear resistance of structures coated with aluminum alloys

For a long time, it was believed that the coating formed in the spark mode has lower protective properties than the traditional anode coating. Because of this, the anodizing was usually stopped at a voltage lower than the breakdown voltage. More recently, it has been established that prolonged electrolysis under sparking conditions leads to the formation of fairly thick anode coatings that exceed in their properties the films obtained by sparkless oxidation. Analysis of anode-spark coatings shows that in them, along with the metal oxides of the substrate in large quantities are atoms and groups of atoms that are part of the electrolyte. In the thickness of the amorphous oxide there are areas of the solidified melt. The latter indicates a strong thermal effect of electrical breakdown on the material of the formed oxide. There is every reason to believe that effective anode-spark molding occurs only if the breakdown is thermal.

As a result of many studies, at present, it is established that the anode-oxide films consist of two layers: a barrier layer, which has a dense structure and is directly adjacent to the oxidized metal, and a porous layer.

The use of electron microscopy has made the most significant contribution to the studied structures of anode-oxide coatings. The results of these tests performed by Keller, Kanter, Robinson and other researchers allowed us to propose a so-called model of a porous anode oxide film based on physical and geometric images.

According to this model, in the first seconds of anodizing on aluminum, a non-porous barrier layer is formed, the beginning of the formation of which is associated with the corresponding active oxidation centers on the metal surface. Hemispherical lenticular microelements grow from these embryos. First isolated, then grow and fill the metal surface with the formation of a solid barrier layer. Under the action of local influence of electrolyte ions in the barrier layer, pores begin to emerge, the number of which is associated with the magnitude of the stress of the forming oxide. As a result, an oxidizing element is formed, similar in shape to a spherical segment, the center of which lies in the area of the porous layer. The growth of the anode-spark coating occurs in two ways that run in parallel. The first of them is the formation of the anode coating by the mechanism of growth of oxide films in the metal-oxide-electrolyte (MOE) system, and the second is the formation of chemical compounds on the electrode surface with the participation of electrolyte components. In the process of forming anode-spark coatings. Along with the formation of the film may occur side chemical and electrochemical reactions that lead to unproductive energy consumption and accumulation of substances in the bath, affecting the quality of sludge. The main side processes are the formation of oxygen and hydrogen due to electrolysis in the area of spark discharges. which lead to unproductive energy costs and the accumulation of substances in the bath, affecting the quality of sludge. The main side processes are the formation of oxygen and hydrogen due to electrolysis in the area of spark discharges. which lead to unproductive energy costs and the accumulation of substances in the bath, affecting the quality of sludge. The main side processes are the formation of oxygen and hydrogen due to electrolysis in the area of spark discharges.

Let us pay attention to the most urgent problems in the field of anodic oxidation that are currently being considered.

In work [30], it was noted that tlectrochemical oxidation is an effective wastewater treatment method. Metal oxide-coated substrates are commonly used as anodes in this process. This article compiles the developments in the fabrication, application, and performance of metal oxide anodes in wastewater treatment. It summarizes the preparative methods and mechanism of oxidation of organics on the metal oxide anodes. The discussion is focused on the application of SnO_2, PbO_2, IrO_2, and RuO_2 metal oxide anodes and their effectiveness in wastewater treatment process.

In work [31] it is said that during plasma electrolytic oxidation (PEO) processes, the factors, such as the shape of the specimen, the location of the cathode electrode, and others have a critical influence on the anode (specimen to be treated) current. This may lead to different oxidation dynamics at different locations on the samples resulting in the non-uniform coating thickness and surface properties. In this work, the current through samples made of 2024 aluminum alloy was monitored in a sodium silicate solution during plasma electrolytic oxidation. The experimental results demonstrate that the distance between the cathode and anode affects the anode current and the oxidation efficiency. The current flowing through the front surface of the specimen is larger than that flowing through the back surface of the same specimen. The measured tribological properties and corrosion-resistance agree well with the effects of the current. The front surface exhibits more superior wear and corrosion resistance than the back surface.

In aqueous zinc-ion batteries, metallic zinc is widely used as an anode because of its non-toxicity, environmental benignity, low cost, high abundance and theoretical capacity. However, growth of zinc dendrites, corrosion of zinc anode, passivation, and occurrence of side reactions during continuous charge-discharge cycling hinder development of zinc-ion batteries. In study [32], a simple strategy involving application of a HfO_2 coating was used to guide uniform deposition of Zn^{2+} to suppress formation of zinc dendrites. The HfO_2-coated zinc anode improves electrochemical performance compared with bare Zn anode.

In [4] the deactivation of an IrO_2–Ta_2O_5 coated titanium anode was studied during an accelerated life test at 2 A cm^{-2} in 1 mol dm^{-3} H_2SO_4 solution using CV, EIS, SEM and EDX. The changes of voltammetric charge, double layer capacitance, oxide film resistance and charge transfer resistance of oxygen evolution with time during the electrolysis were monitored. The morphology and surface composition of the oxide anode before and after electrolysis test were analysed. A comprehensive process of deactivation of the oxide anode was proposed based on the test results and analysis.

The wettability of coatings, including ceramic ones, which show considerable promise for the use on bioengineering products, with physical solution (0.9 % NaCl) have been studied in [34]. It has been found that the use of coatings of all types under study increases the wetting angles on the surface as compared with the initial metal materials (stainless steel of the 12X18H10T grade, titanium alloy of the BT6-grade, Co–Cr–Mo alloy), which serves as a prerequisite for an improvement in the biocompatibility of implants.

Protective α-Al_2O_3 coatings on the surface of a graphite article have been obtained in [35] by method of electric-arc metallization with aluminum and microarc oxidation (anodic spark process). Investigation of the obtained coating by scanning electron microscopy (SEM), X-ray diffraction (XRD), and proton elastic recoil detection analysis (ERDA) showed good quality of the Al and α-Al_2O_3 coatings on graphite. The proposed technology can be used for obtaining protective coatings in low-accessible sites of graphite articles.

The effect of TiB_2 and CrB_2 additions to the commercial self-fluxing FeNiCrBSiC eutectic alloy on the structurization of electrospark coatings was examined in [36]. The mass transfer kinetics in the electrospark deposition of FTB20 (FeNiCrBSiC + 20 % TiB_2) and FCB20 (FeNiCrBSiC + 20 % CrB_2) composite materials and commercial self-fluxing FeNiCrBSiC alloy coatings onto steel 45 using an Alier-52 unit was studied. When the energy parameters of electrospark deposition increased, the mass transfer coefficient became higher and the electrospark coatings thicker and rougher.

The dielectric properties of coatings on AK6 alloy formed with a microarc oxidation method in two electric modes in alkaline-silicate electrolytes are estimated in [37–38]. It is shown that both modes, a galvanostatic mode and an arbitrarily falling power mode in alternating current circuits, make it possible to obtain coatings with a thickness of 30–60 μm, with sufficiently high electrophysical parameters: bulk specific resistance $\rho_v = 3–9 \times 10^9\ \Omega$ m and dielectric strength E = 9–14 V/μm. It is established that higher values of ρ_v and E in the both modes can be achieved in the solutions of 1 g/L KOH + 6 g/L of liquid glass (LG) and 12 g/L of LG. In terms of absolute value, the parameters of the coatings formed in the mode of arbitrarily falling power exceed the same characteristics of the oxide layers formed under conditions of galvanostatic mode by a factor of 1.5–2.5.

Based on the analysis of literature sources, it is established that at present the technology of anode-spark coatings in general is quite well developed. However, the lack of scientifically sound recommendations for the choice of modes of technological processes and characteristics of properties in different operating conditions do not allow the widespread introduction of this technology.

The task of this work was to analyze the processes of anode-spark coatings, improve technology and study the wear resistance of samples processed by this and traditional anode technology.

Selection of technological modes of formation of anode-spark coatings. The development of technology for the application of protective coatings on valve metals in the conditions of spark discharge includes the choice of electrolyte and mode of operation of the bath: voltage, current density, hydrodynamic conditions, etc.

Currently known different types of programmable voltage changes in the bath, pulse and alternating current voltages are selected experimentally, without the necessary theoretical justification. Meanwhile, the electrical regime determines the nature and intensity of discharges and, of course, the temperature conditions on the surface of the anode. With the appropriate choice of electrolyte and electrochemical parameters of the anode-spark sludge, you can get a coating that has high hardness, wear resistance and strong adhesion to the substrate. Appropriate selection of the electrolyte and electrolysis conditions can form a coating that is equal in hardness and wear resistance of corundum and tungsten carbide. The wear of the upper layers is not due to abrasion, but due to chipping of the unevenness of the coating.

To form a coating on aluminum alloys AD31 and B95, we take the current strength range from 1800 A/m^2 to 2500 A/m^2 and the ratio of cathode current to anode 1.15. Molding is carried out at voltages from 120 V to 600 V depending on the state and concentration of the electrolyte.

The practical implementation of the anode-spark process always requires careful coordination of metal-electrolyte pairs. One of the simplest and best-known electrolytes was a dilute (2...8 g/l) KOH solution, which makes it possible to obtain a high-quality anode coating on aluminum. Solutions of some acids can be used for this purpose. The first systematic study of the influence of the electrolyte on the possibility of realization of the anode-spark discharge on aluminum was carried out in [7], where the authors studied the properties of solutions of 33 different substances. The investigated electrolytes were divided into 6 groups. The first includes solutions of salts in which there is a fairly rapid dissolution of aluminum (NaCl, $NaClO_3$, NaOH, HCl, $NaNO_3$ and Na). The second group combines electrolytes that correspond to the achievement without much effort of the passive state of the metal. It includes H_3BO_3, citric and carbonic acids, as well as their salts. Lactic, adipic and oxalic acids (third group) correspond to less effective passive properties. Weak solution of metal at stationary potential is characterized by substances of the fourth group: H_2SO_4, (NH_4) $2SO_8$, Na_2SO_4. In oxalic acid and its sodium salt, sodium acetate, phosphoric acid (fifth group), the range of voltages at which the spark discharge occurs is narrow. The sixth group includes solutions of KF, NaF, disubstituted phosphate and sodium sulfite. in which the spark discharge is narrow. The sixth group includes solutions of KF, NaF, disubstituted phosphate and sodium sulfite. in which the spark discharge is narrow. The sixth group includes solutions of KF, NaF, disubstituted phosphate and sodium sulfite.

The formation of oxide films from aqueous electrolytes in the sparking mode allows to obtain a coating with much better properties than in the formation in the normal anodizing mode. Analysis of the chemical composition shows that in the composition of the anode-spark coatings, rocks with oxides of the base metal of the strip, in large quantities contain atoms that are part of the electrolyte. Other particles of oxides (iron, chromium) present in the electrolyte are also included in the structure of the coating, forming a composite structure.

Investigation of wear resistance of coatings on aluminum alloys. Samples measuring 5×5×20 mm from materials B 95 and AD 31 were used for the research. The samples must have a quality surface. Overflowing of edges on samples is not allowed.

After machining, the samples are ground on grinders with a grain size of: 400 μm, 200 μm, 80 μm. Then the anode-spark coatings were applied on the experimental setup. After coating according to the developed technological process, the samples were washed and dried with filtered paper. Samples with factory coating were additionally ground on the work surfaces with AP-3 diamond paste. The contact area is 0.25 cm^2.

Wear resistance tests were performed on a special installation. Structurally, the installation is made in two positions, which allows you to test two samples with different load conditions at a constant sliding speed. The design of the installation implements the friction scheme of the liner shaft.

The scheme of the test setup is presented in Fig. 3.12. Rotation counter body *7* receives from the DC motor with adjustable speed. The speed of rotation is controlled by an electronic speed meter PIT-1 (*3*). The test sample *8* is fixed in the handle *9*, which before starting work is balanced in relation to the strain beam *10*. The handle of the sample *9* is hinged to the beam. The specified load *P* is created by a set of loads *12*.

Before conducting experiments, the installation system is calibrated. The strain gauges are powered by the UT-4 strain amplifier. Recording of friction forces is performed by a potentiometer type KSP-4.

The body is made of hardened steel 45 (HRC 55) and has the shape of a disk with a diameter of 95 mm and a thickness of 10 mm. Surface roughness Ra = 0, 32 microns.

In the study of coatings under dry friction, the efficiency of the anode-spark coatings paired with hardened steel 45 is low with a predominantly abrasive type of wear. Reduced resistance of the coating is caused by brittle fracture (splitting of individual microvolumes). The coefficient of friction during operation is unstable and is measured in a wide range $f = 0.3 \ldots 0.8$.

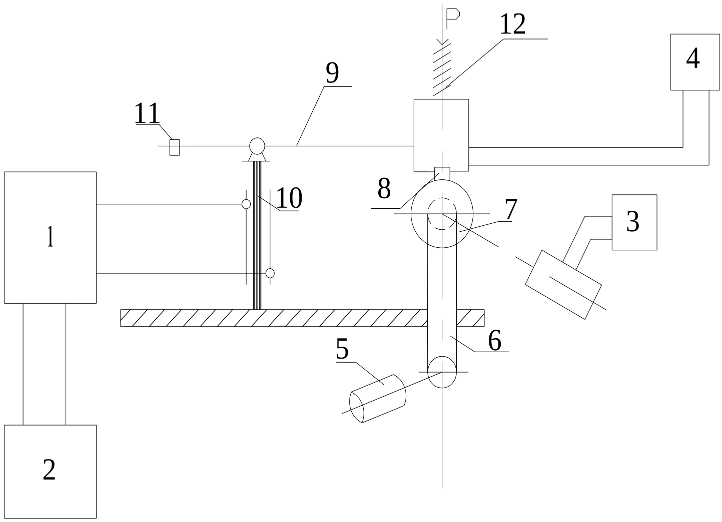

Fig. 3.12. Scheme of the test installation:
1 **– strain amplifier UTCH-1;** ***2*** **– potentiometer PCB 4;**
3 **– sensor-meter of sliding speed;** ***4*** **– thermocouple temperature sensor potentiometer EPD-12;** ***5*** **– electric motor;** ***6*** **– V-belt transmission;**
7 **– working disk (counter body);** ***8*** **– experimental sample;**
9 **– sample holder;** ***10*** **– strain beam;** ***11*** **– load-balancer;**
12 **– loads to create the desired pressure** ***R***

The study of anode-spark coatings in the mode of ultimate lubrication was studied in the medium of oil I-20, which were saturated samples. The research was carried out before complete wear of the coating formed at different durations of molding. Data on the effect of molding duration on the wear resistance of coatings are given in Table 3.7. The wear intensity is calculated by the formula:

$$U_w = \frac{\Delta G}{S},$$

where ΔG is the weight wear, g; S is the path of friction, mm.

Table 3.7

The results of studies of anode-spark coatings

Time, τ_{pr}, min	Weight of sample G_1, g	Sample weight after the study G_2, g	Weight wear $\Delta G \cdot 10^{-4}$, g	The path of friction $S \cdot 10^3$, m	Wear intensity $I_W \cdot 10^{-9}$, g/m	Coefficient of friction f
45	1.05795	1.057890	0.60	16.4	3.658	0.13
60	1.07660	1.076408	1.92	65.6	2.927	0.12
90	1.17212	1.172018	1.025	24.6	4.170	0.14

Figure 3.13 shows the dependence of wear intensity I_W from the duration of processing (molding) tobr. As can be seen, the optimal duration of molding should be considered up to 60 minutes The coefficient of friction is practically independent of the duration of processing and is measured in the range of 0.12…0.14.

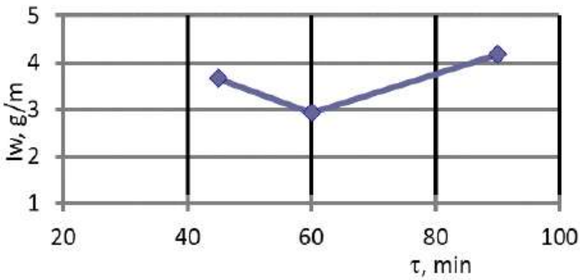

Fig. 3.13. Dependence of wear intensity of B-95 alloy on molding time

The results of comparative studies of wear resistance of anode-spark coatings and coatings formed by traditional oxidative anodizing technology are shown in Table 3.8 and graphically in Fig. 3.14. The wear criterion was the weight wear of the samples according to the results of weight measurements before and after wear.

With increasing friction path, the coefficient of friction increases slightly to the appropriate value, and then stabilizes. As the load increases, the friction force and the coefficient of friction increase.

The analysis of the obtained results shows that the anode-spark coating is superior in its properties to the coatings obtained under oxidative anodizing conditions formed in optimal modes, but in the same electrolyte with the same concentration.

Table 3.8

Wear test results

Parameters	Meter readings, N	Friction path $S \cdot 10^3$, m	Weight wear $\Delta G \cdot 10^{-4}$, g	Friction force $F_{mp} \cdot 10^{-2}$, N	Coefficient of friction f
AC P = 0.4 MPa					
1	50	16.4	0.90	40	0.12
2	100	32.8	1.52	44	0.13
3	150	49.2	1.75	43	0.14
ASC P = 0.4 MPa					
1	50	16.4	0.5	7	0.07
2	100	32.8	0.8	9	0.09
3	150	49.2	1.0	8	0.08
ASC P = 0.8 MPa					
1	50	16.4	0.75	20	0.1
2	100	32.8	1.35	24	0.12
3	150	49.2	1.50	26	0.13

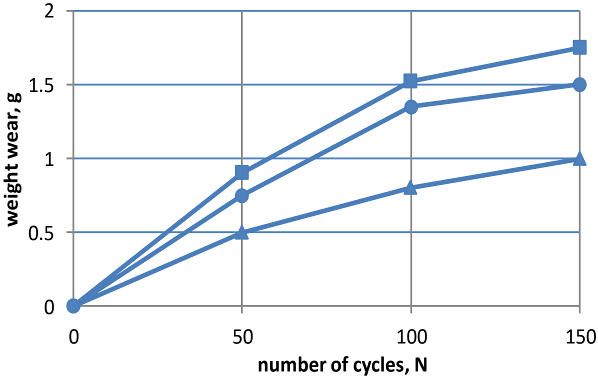

Fig. 3.14. Dependence of wear of coverings on duration of tests:
▲ – ASC P = 0.4 MPa; ● – ASC P = 0.8 MPa; ■ – AC P = 0.4 MPa

The wear resistance of anode-spark coatings in comparison with galvanic anode coatings at the same load was almost 2 times higher. The coefficient of friction of the coatings varied in the range of 0.1...0.14. The optimal duration of coating formation is 60 minutes. It is also established that the wear resistance of anode-spark coatings depends not only on the duration of treatment, but also on other process parameters.

It is established that prolonged electrolysis in the conditions of sparking leads to the formation of anode coatings that exceed in their properties the films obtained by non-sparking oxidation. Comparative studies of the wear resistance of anode-spark coatings and galvanic anode coatings under the same test conditions showed that the wear of anode-spark coatings is almost twice lower for the entire load range.

References for Chapter 3

1. Korolev, A. V., Korolev, A. A. Friction machine for accelerated wear tests of frictional rolling elements. J. Frict. Wear 38, 77–81 (2017).

2. Ronen, S., Goltsberg, R. & Etsion, I. A comparison of stick and slip contact conditions for a coated sphere compressed by a rigid flat. Friction 5, 326–338 (2017).

3. Wang, W. J., Lewis, S. R., Lewis, R., Beagles, A., He, C. G. The role of slip ratio in rolling contact fatigue of rail materials under wet conditions, Wear 376–377, 1892–1900 (2017).

4. Guo, Yi, Jonathan Keller. Validation of combined analytical methods to predict slip in cylindrical roller bearings. Tribology International 148, (2020).

5. Deng, S., Lu, Y., Zhang, W., Sun, X., Lu, Z. Cage slip characteristics of a cylindrical roller bearing with a trilobe-raceway. Chinese Journal of Aeronautics 31/2, 351-362 (2018).

6. Goryacheva, I. G., Torskaya, E. V. Modeling the Accumulation of Contact Fatigue Damage in Materials with Residual Stresses under Rolling Friction. J. Frict. Wear 40, 33–38 (2019).

7. Zhu, S., Sun, J., Li, B., Zhao, X., Zhu, G. Stochastic models for turbulent lubrication of bearing with rough surfaces. Tribology International 136, 224–233 (2019).

8. Rahmani, F., Pandey, R.,. Dutt, J. Performance Studies of Powder-Lubricated Journal Bearing Having Different Pocket Shapes. J. Tribol 140(3), 031704 (2018).

9. Zhang, C., Gu, L., Mao, Y. et al. Modeling the frictional torque of a dry-lubricated tapered roller bearing considering the roller skewing. Friction 7, 551–563 (2019).

10. Everitt, C.-M., Alfredsson, B. Surface initiation of rolling contact fatigue at asperities considering slip, shear limit and thermal elastohydrodynamic lubrication. Tribology International 137, 76–93 (2019).

11. Xue, Y., Chen, J., Guo, S. et al. Finite element simulation and experimental test of the wear behavior for self-lubricating spherical plain bearings. Friction 6, 297–306 (2018).

12. Gupta, P., Zaretsky, E. New Stress-Based Fatigue Life Models for Ball and Roller Bearings. Tribology Transactions 61(2), 304–324 (2018).

13. Jin, C., Li, G., Hu, Y., Xu, Y. Xu, L. Identification of Mechanism Stiffness of Autoeliminating Clearance for Auxiliary Bearing. Tribology Transactions 62 (2) (2019).

14. Dykha, A.,. Sorokatyi, R., Makovkin, O., Babak, O. Calculation-Experimental Modeling of Wear of Cylindrical Sliding Bearings, Eastern-European Journal of Enterprise Technologies 5 (1 (89)), 51–59 (2017).

15. Aleksandr, D., Dmitry, M. Prediction the wear of sliding bearings. International Journal of Engineering & Technology, 7 (2.23), 4–8 (2018). doi: https://doi.org/10.14419/ijet.v7i2.23.11872.

16. Poplawski JV. Slip and cage forces in a high-speed roller bearing. J Lubr Tech 1972; 94 (2): 143–50.

17. Dominy J. The Nature of Slip in High-Speed Axially Loaded Ball Bearings. Proceedings of the Institution of Mechanical Engineers, Part C: Journal of Mechanical Engineering Science. 1986; 200 (5): 359–365. doi:10.1243/PIME_PROC_1986_200_139_02

18. Selvaraj, Arthanari & Marappan, R. (2011). Experimental analysis of factors influencing the cage slip in cylindrical roller bearing. The International Journal of Advanced Manufacturing Technology. 53. 635–644. 10.1007/s00170-010-2854-5.

19. Takafumi Yoshida, Masashi Hirota, Kimito Yoshikawa. Analysis of Cage Slip in Ball Bearings Considering Non-Newtonian Behavior and Temperature Rise of Lubricating Oil, Tribology Online, 2013, Vol. 8, Issue 3, Pp. 210–218, Released May 15, 2013, https://doi.org/10.2474/trol.8.210, https://www.jstage.jst.go.jp/article/trol/8/3/8_210/_article/-char/en

20. Jafar Takabi & M. M. Khonsari (2014) On the Influence of Traction Coefficient on the Cage Angular Velocity in Roller Bearings, Tribology Transactions, 57:5, 793-805, DOI: 10.1080/10402004.2014.913327

21. Cavallaro, G., Nelias, D. Analysis of high-speed inter-shaft cylindrical roller bearing with flexible rings. Tribol T 2005; 61 (11): 38–244.

22. Hu, X., Luo, G. H., Gao, D. P. Quasi-static analysis of cylindrical roller inter-shaft bearing. Chin J Aeronaut 2006; 21 (6): 1069–74.

23. Xiuhai, Liu, Sier, Deng. Dynamic stability analysis of cages in highspeed oil-lubricated angular contact ball bearings. Trans Tianjin Univ 2011; 17 (1).

24. Deng, S. E., Jia, Q. Y., Xue, J. X. Design principle of rolling bearings. 2nd ed. Beijing: Standards Press of China; 2014. p. 113–24.

25. Gear, C. W. Simultaneous numerical solution of differential-algebraic equations. IEEE Trans Circ Syst 1971; 18 (1): 89–95.

26. Chang-Fu Han, Hsiao-Yeh Chu, Ruei-Yang Luo & etc. 2018 Effects of groove factor and surface roughness of raceway in ball-bearing-like specimens on tribological behavior and the onsets of two instabilities of dry contacts. Wear. 406, 126. https://www.sciencedirect.com/science/article/abs/pii/S004316481731551X

27. Dykha, A., Sorokatyi, R., Makovkin, O., Babak, O. 2017 Calculation-experimental modeling of wear of cylindrical sliding bearings.

Eastern-European Journal of Enterprise Technologies. 5, 1, 51–59. doi: 10.15587/1729-4061.2017.109638

28. Sorokatyi, R. V., Dykha, A. V. 2015 Analysis of Processes of Tribodamages under the Conditions of High-Speed Friction. J. Friction and Wear, 36, 422. doi: 10.3103/S106836661505013X

29. Sorokatyi, R., Chernets, M., Dykha, A., Mikosyanchyk, O. 2019. Phenomenological Model of Accumulation of Fatigue Tribological Damage in the Surface Layer of Materials Mechanisms and Machine Science, 73, 3761. https://link.springer.com/chapter/10.1007%2F978-3-030-20131-9_371

30. Subba Rao, A. N., Venkatarangaiah, V. T. Metal oxide-coated anodes in wastewater treatment. Environ Sci Pollut Res 21, 3197–3217 (2014). https://doi.org/10.1007/s11356-013-2313-6

31. Wei, C. B., Tian X. B., Yang S. Q., Wang, X. B., Ricky, K. Y. Fu, Paul, K. Chu, Anode current effects in plasma electrolytic oxidation, Surface and Coatings Technology, Vol. 201, Issues 9–11, 2007, Pp. 5021–5024.

32. Bin Li, Jing Xue, Chao Han, Na Liu, Kaixuan Ma, Ruochen Zhang, Xianwen Wu, Lei Dai, Ling Wang, Zhangxing He, A hafnium oxide-coated dendrite-free zinc anode for rechargeable aqueous zinc-ion batteries, Journal of Colloid and Interface Science, Vol. 599, 2021, Pp. 467–475.

33. Xu, L. K., Scantlebury, J. D. A study on the deactivation of an IrO_2–Ta_2O_5 coated titanium anode, Corrosion Science, Vol. 45, Issue 12, 2003, Pp. 2729–2740.

34. Sevidova, E. K., Kononenko, V. I. Assessment of bioengineering ceramic coatings using the wetting method. J. Superhard Mater. 29, 82–85 (2007). https://doi.org/10.3103/S1063457607020037.

35. Pogrebnjak, A. D., Tyurin, Y. N. The structure and properties of Al_2O_3 and Al coatings deposited by microarc oxidation on graphite substrates. Tech. Phys. 49, 1064–1067 (2004). https://doi.org/10.1134/1.1787669.

36. Umanskyi, O., Storozhenko, M., Tarelnyk, V. et al. Electrospark Deposition of Fenicrbsic–Meb_2 Coatings on Steel. Powder Metall Met Ceram 59, 57–67 (2020). https://doi.org/10.1007/s11106-020-00138-5.

37. Markov, M. A., Bykova, A. D., Krasikov, A. V. et al. Formation of Wear- and Corrosion-Resistant Coatings by the Microarc Oxidation of Aluminum. Refract Ind Ceram 59, 207–214 (2018). https://doi.org/10.1007/s11148-018-0207-3

38. Gutsalenko, Y. G., Sevidova, E. K. & Stepanova, I. I. Evaluation of Technological Capability to from Dielectric Coatings on AK6 Alloy, Using a Method of Microarc Oxidation. Surf. Engin. Appl.Electrochem. 55, 602–606 (2019). https://doi.org/10.3103/S1068375519050041

Chapter 4.

TESTS OF TRIBOLOGICAL AND OPERATIONAL PROPERTIES OF LUBRICANTS

4.1. Theory and experiment of tribological test methods

4.1.1. Modern approaches to the technique of tribological tests. Experiment, theory, methods, equipment

A review of research on modern highly cited periodicals in the field of friction and wear regarding the problems of tribological testing is proposed.

The article [1] presents the development, manufacture and testing of an experimental bench for assessing the fretting fatigue of conductor materials in power lines. The friction machine has three independent drives that allow testing under a controlled load. This makes it possible to study the influence of relevant parameters on the fretting fatigue process (such as normal, tangential and body forces, wear level and wear surface morphology).

In [2], the technological problem of testing jet engine parts under conditions close to operational ones is solved. A bench for testing blade friction is proposed to study the occurring phenomena and the behavior of rotor blades during contact interactions between the blades and the engine housing. A feature of the presented installation is the possibility of increasing the number of working elements of the chamber, which makes it possible to produce more than one contact per revolution. This article discusses the test setup and its components, the experimental procedure, and examples of results.

In [3], laser microscopy was used to quantify wear mechanisms. The results showed that for some mechanisms it is possible to obtain quantitative data for the classification of wear and tear in accordance with ASTM G98. Some suggestions for modification and improvement of the standard are offered.

In work [4] the study of the brake pad for friction and wear is carried out on an inertial brake dynamometer at various temperatures

(4.200 °C, 250 °C and 300 °C). The actual field tests are carried out on four different trucks, namely a city bus (CB), a high speed bus (HSB), a highway truck (HWT) and a dump truck (TL). This study will be useful for developing the composition of the friction material and predicting the actual life of the brake pad for various trucks.

The article [5] presents experimental setups for conducting research on real machine components and obtaining more realistic results than conventional tribological test benches. Slope pad plain bearings, as well as gears and complete gearboxes for advanced industrial applications, can be tested using the benches described in the article. A double disc machine and a closed loop gear test bench are used to investigate the various wear mechanisms that occur in gears.

The authors of the study [6] study the problem of reducing friction and wear in metal-metal systems, as well as in some mechanical components. This paper presents a computational study based on Archard's linear wear law and Finite Element Method (FEM) modeling for dry sliding wear analysis in pin-on-disk testing. The Archard wear model was implemented in a FORTRAN user routine (4.UMESHMOTION) to describe sliding wear. The modeling of wear particle formation mechanisms was taken into account using the overall wear factor obtained from experimental measurements. In such an implementation, a step-by-step calculation of surface wear based on nodal displacements is considered using adaptive mesh tools that rebuild local nodal positions. Numerical and experimental results were compared in terms of wear rate and friction coefficient. In addition, during numerical simulation, the distribution of the stress field and the change in the surface profile across the worn track of the disk were analyzed.

In the study [7], based on the classical theory of adhesive wear by Archard, a three-dimensional finite element model was created to simulate the process of destruction of self-lubricating spherical plain bearings under conditions of oscillatory wear. The results show that self-lubricating spherical plain bearings go through two different stages in the wear process, namely an initial wear stage and a stable wear stage. The moment of friction at the initial stage of wear is somewhat less than the moment of friction at the stage of stable wear; however, the wear rate in the initial wear stage is high. The developed finite element model can be used to analyze bearing wear mechanisms and predict bearing life.

The article [8] experimentally and theoretically investigates the effect of lubrication on stresses at high temperature. A statistical formula has been developed to predict the Striebeck curves given the interaction of asperities with lubricant on the contact surface. It has been found that increasing the temperature at the interface can significantly change the performance of the lubricant due to the influence of the lubricant additive and that the conventional assumption of a constant coefficient of friction for a rough contact is not practical. As the temperature increased, the boundary layer formed by the lubricant molecules dissolved, and a soft solid layer was formed by lubricant additives at the contact boundary. It was also found that in the boundary lubrication regime, friction depends on the sliding speed due to the formation-destruction cycle of a soft hard layer,

It is noted in [9] that the characteristics and service life of structural materials at high temperatures are largely affected by the degradation of the material during wear and corrosion. To evaluate material performance at high temperature, it is necessary to understand the processes and their interactions to select and develop new advanced materials. In the present study, an experimental setup for testing and high-temperature abrasion is presented, taking into account the oxidation process.

In [10], the change in temperature over time in a deep groove ball bearing in an oil bath lubrication system was experimentally and analytically studied. The test device is a radially loaded ball bearing equipped with instruments to measure the friction torque as well as the transition temperature of the outer ring, oil and housing. The developed mathematical model provides a comprehensive thermal analysis of a ball bearing, taking into account frictional heat release, heat transfer processes and thermal expansion of the bearing components. Experiments are carried out for various speeds and loads to test the model. It has been established that the predicted temperatures at various loads and speeds agree well with those measured experimentally.

The article [11] discusses the optimization of the tribological characteristics of lubricating oils used in the processing industry. Optimum lube oil performance is determined by multivariate optimization of viscosity, temperature and oil film thickness. Experimental test results are shown for the oil used in the real plant and the new oil obtained from the simulation.

Reference [12] presents a methodology for deriving pressure-dependent friction laws from experimental tribometric testing of rubber-to-metal contacts. Tribometric tests are simulated to analyze the contact area and obtain an approximation of the contact pressure distribution. The proposed methodology is recommended for evaluating the experimental results of tribometric tests carried out according to the "flat surface" and "cylinder surface" schemes. Planar and cylindrical materials have been fabricated with very similar surface morphology and therefore theoretically the same pressure dependence of the law of friction.

Article [13] contains a description of the test bench and the first experimental data concerning the mechanical and thermal characteristics of a rotor supported by air-lubricated bearings under external pressure. The stand allows you to load the rotor radially and axially in both static and dynamic modes, as well as measure the orbits on the supports. Rotating unbalance response at various speeds has been measured up to 60,000 rpm. The rotor is stable and has no vortex instability.

The authors of this work analyzed the methods for identifying the parameters of wear patterns for various wear models and test schemes [14–17].

The above review of the literature confirms the versatility of tribological testing methods in terms of techniques, test conditions, materials, design of benches and samples, modeling procedures and processing of experimental results.

4.1.2. Basic principles of tribological testing

Duration of tribological tests. Wear reduction is carried out mainly in three directions:

1) the creation of wear-resistant surfaces based on the laws of tribomaterials science;

2) creation of lubricants, lubricating additives and lubricating systems;

3) creation of methods for reliable prediction of wear of components based on theoretical tribology.

With regard to friction units, the stages of a rational test cycle are formulated as follows:

1) selection of combinations of materials based on a priori information;

2) identification of the boundaries of compatibility of a friction pair in terms of the determining parameter;

3) modeling on samples of the operating conditions of tribocouplings;

4) full-scale simulation on the stand, taking into account the main operational parameters of the tribocouplings;

5) full-scale modeling, taking into account the typical operating conditions of the friction unit in the machine during operation.

If wear tests of a friction pair are carried out strictly under the operating conditions of the unit, taking into account the statistical nature of wear, then the duration of the testing process for a statistically representative number of samples can last for months and even years. There are various methods for forcing tests in order to speed up the process. It is shown that without building reliable mathematical models of nonlinear wear processes, the use of accelerated wear testing methods can lead to errors. Based on the considered models, the following methods of accelerated forced tests are proposed:

1) extrapolation in time;
2) extrapolation by load;
3) the principle of requests;
4) interpolation on intervals;
5) extrapolation on intervals;
6) double consecutive extrapolation;
7) double parallel extrapolation, etc.

The analysis of the methods shows that the main success in the application of various accelerated methods is determined by the reliability of the mathematical model underlying the process. The friction unit of any machine, regardless of the designer, technologist or operator, goes through at least two stages during operation: the running-in stage and the stage of steady wear. When developing methods for accelerated wear testing of materials, it is necessary to take into account the presence of transient processes and running-in at the initial stages.

Test schemes and conditions in contact. The decisive role in the validity of the laboratory test method is played by the geometry of the contacting elements. Geometric schemes are systematized or simply given in many reference books and articles. In most of the frequently used test schemes, for example, ball-plane, etc., none of the publications provides formulas for calculating contact pressures, the main parameter of test conditions. This is in most cases one of the main causes of scatter and non-reproducibility of test results. On the other hand, the lack of information about the change in pressure conditions during the test devalues the results, making them estimates, as in the case of tests on a four-ball.

Can be offereda list of factors affecting the difference between the rated contact voltages and those calculated under standard conditions. Consideration of this list gives an idea of the reasons for the dispersion of wear test results according to different test schemes:

1) subsurface stress concentrators: grain boundaries, twins and other concentrators;

2) the nature of the surface: topography, texture, residual stresses; surface energy level; microstructure, pollution;

3) surface defects: inclusions and particles of the secondary phase; dents and scratches; grooves and risks; corrosion, rust; traces of etching; fretting traces; slip marks;

4) discontinuities in contact geometry: ends of line contacts; wear particles in the contact area;

5) load distribution inside the bearing: elastic deformations; distortion of parts; clearance in contact;

6) elastic-hydrodynamic lubrication;

7) tangential forces: no slip; sliding rolling.

The first three main factors that determine wear are: pressure P, sliding speed V and contact temperature T. Accounting for these three factors requires a three-factor experiment. The planning of such tests can be carried out according to the well-known mathematical theory of experiment planning.

The environment in which the friction unit operates has a decisive influence on the scheme and test method. When testing friction pairs in the presence of lubricants, their ball circuit is used. The criterion for the quality of the lubricant here is the bulk temperature at which the contact oil layer is destroyed, which is fixed by a sharp increase in the friction coefficient. However, this method, in terms of physical meaning, is the furthest (in comparison with other methods) from reproducing the actual pattern that occurs in contact during friction. It is proposed to give preference to a flat contact as the most specific and corresponding to real nodes. Obviously, to a large extent, negative conclusions about the four-ball scheme are explained by the lack of methods for estimating contact pressures and neglecting wear. Improvements in the accuracy of determining the antiwear properties on a four-ball machine can be obtained using the preprint method.

It is experimentally shown on a four-ball machine that the volumetric wear of a spherical sample is a single-valued linear function of the work of the friction forces. A linear dependence of wear on pressure was also obtained. Obviously, the results obtained are of a particular nature and are valid for specific test conditions.

BThe large discrepancy in determining the results of wear tests by various methods in the absence of lubrication and abrasive effects, according to studies performed in the USA, is due to factors:

1) heterogeneity and instability of surface morphology and wear marks;

2) the presence of particles on the sliding surface as a third body;

3) dynamic rigidity of the installation, as a factor leading to load fluctuations;

4) the shape of the sample or test design leads to different coefficients of variation of the results.

Wear measurements, testing machines. The wear measurement method is an integral part of the wear test method. The literature describes in detail the methods of artificial bases: the method of imprints, the method of punched imprints, the method of cut holes, and the concept of the method of radioactive isotopes is given. All methods are divided into periodic or discrete and continuous without stopping the machine. Among discrete methods, methods are distinguished: 1) micrometric measurements; 2) weighing; 3) profiling; 4) artificial bases.

Continuous methods:

1) according to the content of wear products in used oil;

2) radioactive isotopes;

3) pneumatic micrometering;

4) according to the flow rate of the working medium through the slots between the rubbing surfaces;

5) lever devices and indicators;

6) mesdoses;

7) inductive sensors:

8) strain gauge micrometering.

Any testing machine can be considered as a system consisting of two main parts:

1) testing unit: sample, counter-sample and their fastening;

2) everything else: drive, gears, electrical part, loading, etc.

The study of the parameters of wear particles provides such information about the nature and intensity that it is difficult to overestimate. Obviously, this branch of tribology is still waiting for its intensive development. Photographs of the surfaces of wear particles show that their structure and geometry practically repeat the surface layers of the bodies. By the type of particles, one can judge the stage of wear. Information about particle morphology can be obtained using a bichromatic microscope. The shape of the wear products themselves corresponds to the implemented friction mechanisms. For normal wear, the particles are lamellar; for abrasive – the form of microchips; Fatigue fracture mechanisms correspond to particles of rounded geometry or even spherical ones.

At present, wear particle analysis is widely used to monitor the condition and predict the failure of lubricated components in machines. The parameters of the wear particles reflect both the nature and degree of wear of the rubbing surfaces. Methods and devices for diagnosing the state of machines based on wear particles distinguish between external and built-in. An analysis of patents and publications points to the intensive development of built-in ferrodiagnostics devices. In this case, a variety of principles are used: spectral analysis, ferrography, light scattering, in-line ultramicroscopy, activation methods.

Wear contact tasks. Contact pressures are one of the first three main factors (pressures σ, temperature T, sliding speed V), determining the intensity of surface wear for given materials and lubricants.

The role of pressure here is close to the role of the stress state in the problem of ensuring strength. In problems of contact strength, contact pressures are also defined as the first stage in solving a strength problem. At the second stage, the stress state is determined, at the third stage, using the criteria of strength, ductility or fatigue, the question is decided whether the structure will fail or not. The logic of assessing the state of the friction unit in terms of wear is somewhat different. At the first stage, for a given pair of friction and lubrication, the dependence of wear is studied u_w or wear rate du_w/dS from the main factor – pressures and friction paths, the parameters of this dependence are determined.

At the second stage, the contact problem is solved taking into account the wear for the considered friction unit, for example, for a plain bearing, and the dependence of the wear of this unit on the load dimensions and the found model parameters is determined.

At the third stage, this dependence, taking into account the parameters of the model, calculates the wear of the assembly and compares it with the allowable wear. This stage can be performed in a deterministic setting based on average values or in a probabilistic setting with an estimate of the reliability of the node.

In the general case, the statement of the contact problem for two bodies, taking into account wear, consists of the following equations and conditions. The first basic basic relation is the condition of continuity in contact in algebraic form:

$$u_e(x, y, s) + u_w(x, y, s) = u(x, y),$$

where $u(x, y, S)$ – full elastic normal contact displacements of both bodies; x, y – coordinates, s – friction path.

The second basic equation in the formulation of the problem is the equation of equilibrium of contacting bodies:

$$Q = \int_F \sigma(x, y, S) dF ,$$

where Q – the total load acting on the bodies (the projection of the load on the vertical axis); $\sigma(x, y, S)$ – projection of contact pressures on the same axis; F – contact surface area.

The third basic relation of the contact problem with wear is the equation of the wear model in differential form:

$$\frac{du_w}{ds} = F(\sigma, s)$$

or in integral form:

$$u_w(s) = \int_0^S F(\sigma, s) ds .$$

The complexity of the final equation and the success of solving the problem as a whole largely depend on the degree of complexity of the wear model.

The development of methods for solving contact problems with wear taken into account has gone from the simplest problems to the refinement of models and the complexity of solutions. The wear model is a differential (or integral) relationship between wear and the main factors. In this paper, of these factors, only the influence of pressure is studied.

The test method should be based on the solution of the contact problem for a friction pair sample-counter-sample. Rigorous solutions of this problem with allowance for compliance are complex. It is promising to use a calculation scheme in which the contacting bodies are rigid. With sufficiently large wear, neglect of elasticity is permissible.

Based on the analysis of the current state of test methods for wear of friction pairs and the need for methods with uniquely defined operating conditions for contact pressures, the following task was set and solved in this work: development of a theory of a test method for wear of friction pairs according to the ball-cylinder scheme, which makes it possible to uniquely determine the parameters wear patterns and general characteristics of the wear resistance of materials.

Wear models. Models (law) of wear processes are dependences of the intensity of wear (or wear) on the determining factors of the process, which are used in the design of friction nodes, forecasting their wear and to optimize structural, technological and other parameters. The pattern of wear can be applied in practice, if the algorithm for determining the parameters of this pattern is known. It is the quantitative parameters that make it possible to assess the influence of determining factors (pressure, temperature speed). The parameters can be set only based on the results of experimental tests, which makes the model close to the real operating conditions of the friction unit.

The theory of determining the parameters of wear models is developed on the basis of the solution of inverse wear-contact problems (that is, when the dependences for the calculation of parameters are determined according to the accepted mathematical form of the law of wear, geometric ratios (conditions of continuity in contact), equilibrium conditions.

The more determining factors in the model, the more difficult the solution. So already two parameters (for example, pressure and speed) significantly complicate the task and require certain assumptions.

In this work, a conceptual methodology is considered, one of the main tasks of which is the development of the theory of test methods for the identification of wear parameters.

It is proposed as the most appropriate test schemes to use schemes when during the tests the contact pressure changes due to a change in the contact area, which makes it possible to have results for the pressure range based on the results of the tests of one sample. Such test schemes include: four-ball scheme, sphere – ring, cone – ring cross cylinders, cylinder – plane, sphere – plane and others.

For the tests, the scheme is adopted, which, according to geometric and technological features, most closely corresponds to the real tribo-coupling. Thus, the wear models obtained by the four-ball scheme should be used to evaluate the wear resistance of connections in which contact is made along a line or at points (gears, cam mechanisms) with small contact area sizes. For connections in which the dimensions of the contact area are commensurate with the dimensions of the contacting bodies (sliding bearings, ball bearings), other test schemes should be used: "cone-ring", "sphere-ring", which more adequately correspond to real contact.

At the initial stages of solving this problem, the theoretical foundations of test methods were considered only for the contact pressure factor. In this work, methods of the theory of tests for a larger number of determining factors for the above-mentioned test schemes with a variable contact area are developed. This made it possible to evaluate the influence of speed and temperature factors on the wear process.

Having a developed theoretical apparatus, tests of the friction unit are carried out in conditions close to real ones (in terms of materials, lubrication, temperature, etc.) and the parameters of the wear model are quantitatively calculated.

Based on the obtained wear model, you can:

– calculate (predict) the wear of the unit under different conditions based on contact pressure and sliding speed, for example, at the stage of the design calculation of the friction unit;

– to optimize the structural and technological parameters of the friction unit according to the wear criterion.

The proposed calculation-experimental approach does not give one hundred percent compliance with the real flow of the process, but it is a necessary way to create calculation engineering methods for predicting the wear resistance of friction nodes of technical tribostems.

4.1.3. Implementation of the method of tribological testing of structural and lubricant materials according to the "ball-cylinder" scheme

To simulate the wear of a spherical indenter along a cylinder, a wear regularity (model) is proposed in the form of a dimensionless complex of determining factors (contact pressure and sliding speed):

$$\frac{du_W}{dS} = fC_W\left(\frac{\sigma}{HB}\right)^n\left(\frac{VR^*}{\nu}\right)^p, \tag{4.1}$$

where u_W is the ball wear;

S is the friction path;

f is the coefficient of friction in the ball-cylinder pair;

σ is the normal contact pressure;

HB is the hardness of the ball material;

V is the sliding speed;

R^* is the reduced radius of the sphere and cylinder;

ν is the kinematic viscosity of the oil;

C_W, n, p are the wear resistance parameters.

Let us take the form of the worn surface of the ball in the form of a circular sector with a profile radius a (Fig. 4.1).

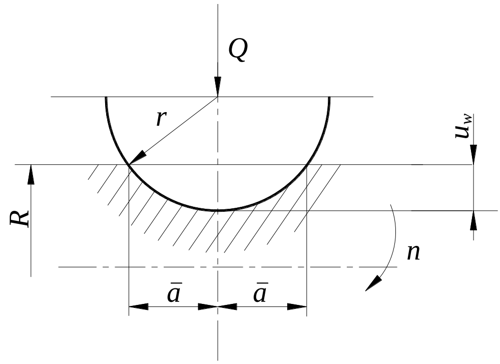

Fig. 4.1. Scheme of contact "cylinder-ball":
***Q* is load; *n* is the speed of rotation; $\bar{a}$ is the half-width of the contact;**
R, r are the radius of the cylinder and balls

We also assume that the contact pressure under the wearing ball on the non-wearing surface of the cone is uniformly distributed:

$$\sigma = \frac{Q}{\pi a^2} . \quad (4.2)$$

In the case of ball-plane contact, the maximum wear of the ball is determined by the expression:

$$u_W = \frac{a^2}{2r} , \quad (4.3)$$

where r is the radius of the ball.

In the case of ball friction not along a plane, but along a cylindrical rotating surface, the dependence of wear on the contact radius will to some extent differ from that accepted for a plane. Let us estimate the magnitude of this deviation.

For friction on the cylinder, the contact area on the ball is curved and is performed along the radius of the cylinder R. In this case, with the same (with a plane) contact area, the wear value (4.3) is added to the wear value:

$$u_{W_1} = \frac{a^2}{2R} , \quad (4.4)$$

where R is the radius of the cylinder.

The relative error in determining wear from not taking into account the curvature of the cylinder, taking into account (4.3) and (4.4), is determined by the ratio:

$$\frac{u_W}{u_{W_1}} = \frac{r}{R}. \tag{4.5}$$

It follows that an error of 1 % is provided for a ratio of radii of 1/100. Yes, at $r = 6.35$ mm the radius of the cylinder should be $R =$ 635 mm, which does not seem correct for the design of the test facility.

It follows from the obtained estimate that the use of the formula for calculations when testing a ball-cylinder pair can lead to errors. Therefore, it is necessary to take into account in the calculations of the parameters of wear models the total wear over the entire contact area:

$$u_W^* = \frac{a^2}{2r_1} + \frac{a^2}{2R} = a^2 \frac{r+R}{2Rr} = \frac{a^2}{R^*}.$$

where

$$R^* = \frac{Rr}{R+r}. \tag{4.6}$$

Thus, when testing for wear according to the ball-cylinder scheme, the dependencies for the ball-plane scheme can be used, if the ball radius is replaced by the reduced radius according to formula (4.6).

Let us represent the experimental dependence of the radius of a truncated sphere as a power approximating function:

$$a(S) = cS^{\beta}, \tag{4.7}$$

where c and β − approximation parameters, which are determined by the results of wear tests.

Integrating the wear pattern (4.1), we obtain the integral form of the ball wear model:

$$u_W(S) = fC_W \int_0^S \left(\frac{\sigma(S)}{HB}\right)^n \left(\frac{VR^*}{\nu}\right)^p dS. \tag{4.8}$$

Substituting the expression for wear into the left side of the obtained dependence $u_W = \dfrac{a^2}{2R^*}$, and to the right – the expression for the contact pressure (4.2), we get:

$$\frac{a^2(S)}{2R^*} = fC_W \int_0^S \left[\left(\frac{Q}{\pi \bar{a}^2(S)} \right) \frac{1}{HB} \right]^n \left(\frac{VR^*}{\nu} \right)^p dS, \tag{4.9}$$

or, taking into account (4.7), after integrating along the friction path, we obtain:

$$\frac{c^2 S^{2\beta}}{2R^*} = fC_W \left(\frac{Q_1}{c^2 \pi HB} \right)^n \left(\frac{VR^*}{\nu} \right)^p \frac{S^{1-2\beta n}}{1-2\beta n}. \tag{4.10}$$

From the condition of satisfiability of equation (4.10) for all values of S it follows:

$$2\beta = 1 - 2\beta n, \tag{4.11}$$

where:

$$n = \frac{1-2\beta}{2\beta}. \tag{4.12}$$

To define a parameter p tests are carried out at two values of the sliding speed V1 and V2, from which we obtain two groups of experimental data with approximating functions:

$$\begin{aligned} a_1 &= c_1 S^{\beta}; \\ a_2 &= c_2 S^{\beta}. \end{aligned} \tag{4.13}$$

Here we consider the problem of determining wear parameters based on the results of testing specimens with a changing contact area during wear. A change in the wear area causes a change in the values of the contact pressures. Exponent n expression (4.1) characterizes the rate of change of contact pressures during wear and is related to the index β experimental dependence (4.7), which characterizes the rate of change of the contact area during wear. Connection n and β in the accepted wear pattern (4.1) is uniquely described by relation (4.12). Since in the relations under consideration the sliding speed V does not depend on friction path S, then it does not affect the parameters n and β in the process of testing. In this case, changing the sliding speed V only affects the scale factor C_w in expression (4.1). The above reasoning is confirmed by the test results.

Substituting expressions (4.13) into (4.10) we obtain the system of equations:

$$\left.\begin{aligned} \frac{c_1^{\ 2}\beta}{R^*} &= fC_W\left(\frac{Q}{c_1^{\ 2}\pi HB}\right)^n\left(\frac{V_1R^*}{\nu}\right)^p; \\ \frac{c_2^{\ 2}\beta}{R^*} &= fC_W\left(\frac{Q}{c_2^{\ 2}\pi HB}\right)^n\left(\frac{V_2R^*}{\nu}\right)^p. \end{aligned}\right\} \tag{4.14}$$

Dividing the first equation by the second, after transformations we get:

$$(c_1/c_2)^{2n+2} = (V_1/V_2)^p, \tag{4.15}$$

where:

$$p = (2n+2)\frac{\lg(c_1/c_2)}{\lg(V_1/V_2)}. \tag{4.16}$$

To determine the coefficient K_w we use one of the equations (4.14):

$$C_W = \frac{\beta c_1^{\ 2n+2}}{fR^*}\left(\frac{\pi HB}{Q}\right)^n\left(\frac{\nu}{V_1R^*}\right)^p. \tag{4.17}$$

Thus, formulas (4.12), (4.16) and (4.17) make it possible to determine the parameters of the wear pattern in the accepted form (4.1).

Methodology of experimental studies. The tests of the bronze-steel pair were carried out according to the scheme of a spherical sample – a cylindrical counter-sample. A spherical surface with a radius of R = 6.35 mm was made at the end of a cylindrical specimen made of bronze with a diameter of 10 mm. The counterbody disk 96 mm in diameter and *12* mm thick was made of 40X steel, hardened and polished. The setup diagram is shown in fig. 2. The spherical sample *9*, fixed in the body *8*, is pressed against the counter-sample – disk *10* with the help of weights *7*. The disk is lubricated by dipping in an oil bath *13*. The disk is fixed on the shaft *4*, which rotates in bearings *6* with the help of an electric motor *1* through a pulley *2* and a belt transmission *3*.

The motor speed is adjustable from 0 to 1500 rpm. The load can be set up to 1 kg = 10 N per sample. The installation provides for measuring the friction force using a strain gauge beam and lever *12*.

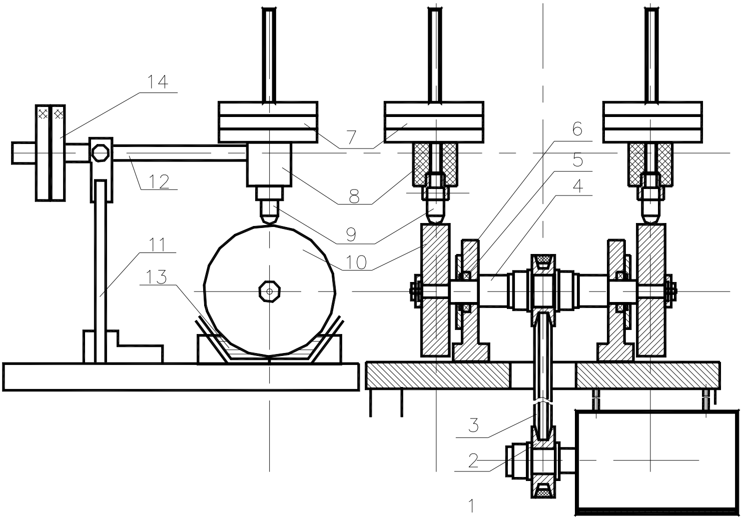

Fig. 4.2. Scheme of the ball-cylinder test setup: *1* – motor, *2* – pulley, *3* – belt transmission, *4* – shaft, *5* – case, *6* – bearing, *7* – weights, *8* – sample holder, *9* – spherical sample, *10* – counterbody (disk), *11* – tension beam, *12* – lever, *13* – oil bath, *14* – balance weight

The tests were carried out with the following initial data: the radius of the ball (sphere) of bronze – $r = 6{,}35$ mm; radius of counterbody, rotating disk $R = 48$ mm; sample load: $Q = 1$ H; the material of the ball is bronze, the disk is hardened steel; lubrication by dipping a rotating disk in a liquid lubricant; disk rotation speed 200 rpm, basic friction path of the ball surface 12 km = $12 \cdot 10^6$ mm. Lubrication was carried out with Magnum 15W–40 oil (TNK, Ukraine) with a viscosity of ν = 40 mm^2/s; friction coefficient f = 0.08. Bronze hardness BrOF10-1 HB = 90 MPa.

Reduced radius according to formula (4.6):

$$R^* = \frac{Rr}{R+r} = \frac{48 \cdot 6.35}{48 + 6.35} = 5.6 \text{ mm.}$$

When tested after a certain number of cycles, using a microscope, the diameter of the ball contact area is measured with an accuracy of microns. The test results are presented in Table 4.1.

Table 4.1

Test results of a bronze sample during friction against a steel counterbody

No.	S, km	$a(V = 0.2m/s)$, mm	$a(V = 0.4m/s)$, mm
1	0.2	0.115	0.135
2	0.4	0.135	0.16
3	1.0	0.175	0.2
4	2.0	0.21	0.235
5	6.0	0.29	0.32
6	12.0	0.335	0.38

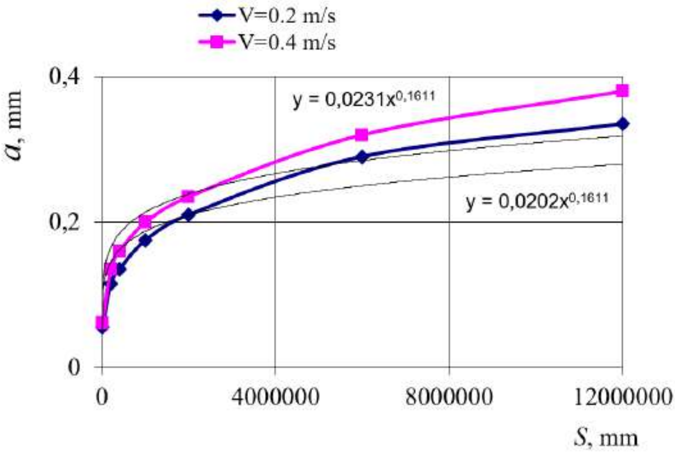

Fig. 4.3. Graphical interpretation of the test results and power-law approximation of the dependences of wear on the friction path *a*(*S*)

On fig. 4.2, based on the test results, the dependence curves of the wear area dimensions on the friction path for two values of the sliding speed are plotted. The Excel program allows you to carry out a power-law approximation of the test results in the form (4.13) with a numerical determination of the parameters of this approximation, shown on the graphs in the form of equations of the trend line (approximating curves).

The results of determining the parameters of these dependencies are shown in Table 4.2.

Table 4.2

The results of the determination of the approximation parameters (4.13)

Options	V = 0.2 m/s	V = 0.4 m/s
c	0.0202	0.0231
β	0.1611	0.1611

In accordance with the procedure shown above, the parameter n can then be determined from formula (4.12):

$$n=\frac{1-2\beta}{2\beta}=\frac{1-2\cdot 0.1611}{2\cdot 0.1611}=2.1\cdot$$

According to formula (4.16), the parameter p is calculated:

$$p=(2n+2)\frac{\lg(c_1/c_2)}{\lg(V_1/V_2)}=(2\cdot 2.1+2)\frac{\lg(0.0202/0.0231)}{\lg(0.2/0.4)}=1.19$$

To calculate the coefficient C_w we use formula (4.17):

$$C_w=\frac{\beta c_1^{2n+2}}{fR*}\left(\frac{\pi HB}{Q}\right)\left(\frac{\nu}{V_1R*}\right)=$$

$$\frac{0.1611\cdot 0.0202^{2\cdot 2.1+2}}{0.08\cdot 5.6}\left(\frac{3.14\cdot 90}{1}\right)^{2.1}\left(\frac{40}{0.2\cdot 5.6}\right)^{1.19}=0.001402$$

Thus, we have the following calculated values of the parameters in the wear pattern (4.1): $n=2.1$; $p=1.19$; $C_W=0.001402$, which identify this dependence and make it possible to predict the wear intensity of tribocouples under given initial operating conditions: by loads, sliding speed, characteristics of lubricants and structural materials.

The main results of the studies carried out in this section are:

1. Based on the analysis of the current state of test methods for wear of friction pairs and the need for methods with certain operating conditions, the problem of developing a theory of test methods for wear of friction pairs according to the ball-cylinder scheme was solved, which makes it possible to determine the parameters of wear models and the general characteristics of the wear resistance of materials.

2. Models (law) of wear processes are dependences of the intensity of wear (or wear) on the determining factors of the process,

which are used in the design of friction nodes, forecasting their wear and to optimize structural, technological and other parameters.

3. Based on the solution of wear-contact problem for the "ball-cylinder" scheme, a theory has been developed for identifying the parameters of the wear pattern. To solve the inverse problem, a method of approximating function is proposed and implemented.

4. The theory of determining the parameters of wear models is developed on the basis of the solution of inverse wear-contact problems (that is, when the dependences for the calculation of parameters are determined according to the accepted mathematical form of the law of wear, geometric ratios (conditions of continuity in contact), equilibrium conditions.

5. Having a developed theoretical apparatus, tests of the friction unit are carried out in conditions close to real ones (in terms of materials, lubrication, temperature, etc.) and the parameters of the wear model are quantitatively calculated.

4.2. Computational and experimental diagnostics of the shear properties of greases

Increasing the durability of machines is achieved not only by the use of new materials, coatings, but by the correct choice of lubricant. For the selection of oils, the most reliable tests are in real operation, but they are expensive. Therefore, laboratory tests are also used. Laboratory tests of lubricants are carried out to determine the physical and chemical properties. Liquid and grease lubricants, separating surfaces with a thin layer, are most commonly used to reduce wear. For testing liquid lubricants, a four-ball test scheme is used. The use of test results is qualitative in nature if there are no solutions to the contact problem with wear for a pair of balls. The authors of this study proposed a method of testing for wear with lubrication according to a four-ball scheme with the determination of the parameters of wear models [18]. The effectiveness of a grease is determined by how long it remains on the surface. The effectiveness of greases is determined by the shear strength of the grease. After the destruction of the framework, the lubricant begins to deform like a liquid. The resistance to flow of a grease is characterized by its viscosity. Viscosity is a property of a grease that depends on the rate of deformation. Typically, viscosity is determined at one fixed strain rate. Many friction units of machines operate under conditions of boundary lubrication of the contacting surfaces. Experimental determination of the shear stress in a loaded lubricated contact is important for analyzing the operation of friction units. In this paper, a method is proposed for determining the function of the contact tangential characteristics of a thin oil layer between solid deformable surfaces.

The idea of the method is as follows. A thin layer of grease is placed between two hard discs. The drive disc starts to turn slowly and passes through the lubricant to the other disc. By measuring the angle of rotation and the moment on the second disc, the dependence of the moment on the angle of rotation is determined. This dependence contains information about the distribution of tangential forces in the lubricant between the discs. Using a mathematical model of film deformations, it is possible to obtain a film shift function with its parameters.

The study of the properties of consistent and liquid oils is currently receiving much attention in the scientific literature on tribology. This is because lubrication is one of the most effective ways to improve machine durability. Lubrication is used in 99 % of machine friction units. The article [19] analyzes the literature and provides an overview of the latest advances in modeling friction in lubricated contact. This review is based on a large body of data, identified gaps in the relevant area that can be used for future research. Greases represent an important group of lubricants due to their specific properties of adhesion to friction surfaces. One of the most common uses for greases is in rolling bearings for various applications.

In work [20] the mechanisms of film formation during grease lubrication in final linear contacts were studied in order to improve the film-forming ability. For the research, an Elastohydrodynamic Lubrication (EHL) test bench was used with two interferometric microscopes that could simultaneously monitor two different contact points. The paper [21] studies the mechanisms of grease lubrication for rolling bearings. The evolution of a lubricating film during rotation of a glass disk in contact with an elastohydrodynamic lubrication (EHL) rolling is studied experimentally. The nature of the evolution of the fat film largely depended on the ranges of speeds and the structure of the lubricant. The main mechanisms that determine the formation of a film of grease in various lubricated contacts are revealed. In [22] considered are greases in wind turbine bearings to reduce wear. The research is completed by experiments with a contact model. Greases with a low base oil viscosity and high leak rate have been shown to be best suited, on average, for the tested conditions. In addition, the results of experiments with bearings are comparable to model experiments. Experimental studies of the tribological properties of greases: film thickness, coefficient of friction, and others are of great importance for practice. In [23] the physical properties and tribological properties of four greases were studied in detail, the worn surfaces were also investigated to understand the friction mechanism. The results show that calcium sulfonate complex grease (CSCG) has a high dropping point, good thermal and oxidative stability, excellent lubricating properties, which is mainly related to the nature and structure of the thickener and the synergism of the grease film and lubricant. In this article [24], lubricated contact at low sliding speeds is analyzed on a special tribometer under controlled boundary conditions. The coefficients of static and dynamic friction versus speed are obtained taking into account dry and lubricated contact. The influence of the coating on the surface of the DLC samples on the friction is also analyzed. The results demonstrated a significant effect of the relative sliding speed on the lubrication friction mechanisms. In [25] the thickness properties were investigated, according to which all greases form thicker than its counterpart liquid oil at low speeds. This suggests that the viscosity of the base oil determines the thickness of the lubricating film at low sliding speeds. Grease friction results indicate that the shape of the grease friction curves can differ significantly from the shape of the friction curves of liquid oils. Research on modeling work processes and mechanisms of grease lubrication of friction units is also of interest. The aim of this work [26] is to study the distribution of contact stresses and deformations of lubricated rolling bearings at high contact pressure. Three-dimensional modeling by the finite element method using the elastoplasticity of the material is carried out and a comparison of the results with the classical law of elasticity is presented. The influence of lubrication, coefficient of friction, radial load has been investigated. The numerical results were compared with lubricated tribological tests under the same loading conditions. The presented results contribute to the tribological interpretation of the lubricated bearing degradation scenario without considering the mechanical properties of the lubricant. The aim of this article [27] is to simulate a mixed elastohydrodynamic lubrication (EHL) in real contact based on a grease rheological model. The model is designed to calculate the thickness of the lubricant film applied to a smooth and rough surface. The influence of load, surface roughness and rheological parameters on the thickness of the lubricating film was also investigated. It is concluded that the friction behavior of the lubricant depends on the thickness of the lubricating film, calculated according to the proposed EHL model.

At the same time, the analysis of literary sources shows that there are practically no mathematical descriptions of the mechanisms of grease lubrication, which is necessary for the creation of engineering methods for predicting and calculating the wear of machines.

Contact interaction in a system consisting of two discs separated by a thin layer of grease is considered. The driving disc rotates at an angle φ_1 and through a layer of lubricant transfers the rotation to the second disc, which rotates at an angle φ_2. The difference between the angles of rotation $\varphi = \varphi_1 - \varphi_2$ is equal to the relative angle of rotation. We assume that the dependence of the friction moment on the disk on the angle of relative rotation in the form of a power-law approximation is known from the experiment:

$$M = c_\varphi \varphi^n , \tag{4.18}$$

where c, n are the parameters of the function, which can be determined from the experimental points by the least squares method.

Parameters c and n can be approximately determined from two experimental points (M_1, φ_1); (M_2, φ_2):

$$n = \frac{\lg(M_1 / M_2)}{\lg(\varphi_1 / \varphi_2)} ;\; c = \frac{M}{\varphi_1^n} . \tag{4.19}$$

The second main relation in the formulation of the problem is the condition of equilibrium of the lubricant layer:

$$M = \int_F \tau(r) r dF , \tag{4.20}$$

where $\tau(r)$ is the dependence of the relative shear forces (shear forces) on the radial coordinate r; F is the circular contact area.

We will assume that between the tangential forces τ and the magnitude of the shear deformation γ there is a power dependence of the form:

$$\tau = G_0 \gamma^\alpha , \tag{4.21}$$

where α, G_0 is the dependency parameters.

The task is to determine the parameters G_0 and α according to the results of the test. Dependence of the magnitude of the layer shear γ

deformation on the rotation angle φ. By definition, the shear strain is equal to the ratio of the circumferential shear displacement to the dimension of the element along the axis z (Fig. 4.4):

$$\gamma = \frac{rd\varphi}{dz} = r\Theta, \tag{4.22}$$

where Θ is the relative twist angle; r is the the radial coordinate of the layer point; $rd\varphi = V_{\varphi}$ is the relative circumferential shear displacement.

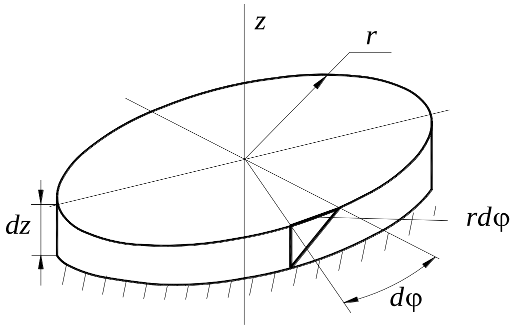

Fig. 4.4. Lubricant layer model

For a small layer thickness, you can take:

$$\gamma = \frac{V_{\varphi}}{h}, \tag{4.23}$$

where h is the grease layer thickness.

Equilibrium equation (4.20) for a circular layer with a diameter d is written in the form:

$$M = \int_0^{2\pi}\int_0^{\frac{d}{2}} \tau r^2 d\varphi = 2\pi \int_0^{\frac{d}{2}} \tau r^2 dr\,. \tag{4.24}$$

Taking into account (4.22), the maximum shear deformation:

$$\gamma_{\max} = \frac{d}{2}\Theta\,. \tag{4.25}$$

Taking the ratio (4.22) to (4.25), we have:

$$r = \frac{d}{2}\frac{\gamma}{\gamma_{\max}} \tag{4.26}$$

or in differential form:

$$dr = \frac{d}{2\gamma_{\max}} d\gamma \, . \tag{4.27}$$

Substituting (4.27) into (4.24), we have:

$$M = \frac{\pi d^3}{4\gamma_{\max}^3} \int_0^{\gamma_{\max}} \tau \gamma^2 d\gamma \, . \tag{4.28}$$

Experimental dependence (4.18) taking into account (4.22) at $r = \frac{d}{2}$:

$$\gamma_{\max} = \frac{d}{2}\Theta = \frac{\varphi}{2}\cdot\frac{d}{h} \tag{4.29}$$

takes the form:

$$M = c_\varphi \varphi^n = c_\varphi \left(\frac{2h\gamma_{\max}}{\alpha}\right)^n \tag{4.30}$$

or

$$M = c_\gamma \gamma_{\max}^n \, , \tag{4.31}$$

where

$$c_\gamma = c_\varphi \left(\frac{2h}{d}\right)^n \, . \tag{4.32}$$

Substituting (4.14) into (4.11), we obtain the equilibrium condition for the layer in the following form:

$$c_\gamma \gamma_{\max}^n = \frac{\pi d^3}{4\gamma_{\max}^3} \int_0^{\gamma_{\max}} \tau(\gamma)\gamma^2 d\gamma \, . \tag{4.33}$$

The solution of the problem in general form is represented as a series with any number of terms and is reduced to a system of algebraic equations. In this case, it makes sense to look for a solution in the form of a power function of the form:

$$\tau(\gamma) = G_0 \gamma^{\alpha}. \tag{4.34}$$

Substituting this function into (4.33), we have:

$$c\gamma_{\max}^{n} = \frac{G_0 \pi d^3}{4\gamma_{\max}^{3}} \int_{0}^{\gamma_{\max}} \gamma^{\alpha+2} d\gamma \tag{4.35}$$

or after integration:

$$c_{\gamma}\gamma_{\max}^{n} = G_0 \frac{\pi d^3}{4(\alpha+3)} \gamma_{\max}^{\alpha}. \tag{4.36}$$

One resolving equation (4.36) contains two unknown quantities G_0 and α. In this case, both unknowns can be found from one equation. From the condition of satisfying the equation for any values $\gamma_{\max}$ it follows:

$$n = \alpha \tag{4.37}$$

and further, taking into account (4.31):

$$G_0 = \frac{4c_{\varphi}(n+3)}{\pi d^3} \left(\frac{2h}{d}\right)^{n}. \tag{4.38}$$

To implement the test method, a device was used to determine the properties of plastic and other lubricants under conditions of a loaded friction lubricated contact. The design of the device is shown in Fig. 4.5. The device consists of a base on which an electric motor is mounted. The torque from the electric motor to the glass is transmitted through the gearbox *2*. Disk *3* is rigidly fixed in the glass with a sample of lubricant *4*. A metal disk contacts the sample of lubricant *4*. The mass of the disk and the rod with the parts attached to them, as well as the mass of removable weights *6*, provides the creation of an axial load lubrication from the side of the measuring disk *5*. The presence of the hinge provides an even distribution of the axial load over the entire contact surface of the disk. A lever is attached to the rod *7*, which is in contact with the dynamometer *10.* The contact cone of the indicator *9* with the screw *8* rests against the upper end of the rod to measure the thickness of the lubricant layer. The shear stress is measured as the lubricant rotates over a metal steel disk pressed against it. The frictional force is recorded with a dynamometer. The axial load of the metal disc on the grease layer can be controlled by interchangeable steel weights. The area of the metal friction disk is 15 cm^2. To test the interaction of a lubricant with a solid surface, the disc can be made of various materials with a given degree of roughness.

The shear stress of the disk (Pa) for the lubricant at a given normal load is calculated by the formula:

$$\tau = 5 \cdot 10^4 \cdot r \cdot F \text{, Па,} \tag{4.39}$$

where F is the force measured by dynamometer, N; r is the lever arm, m ($r = 0{,}0475$ m).

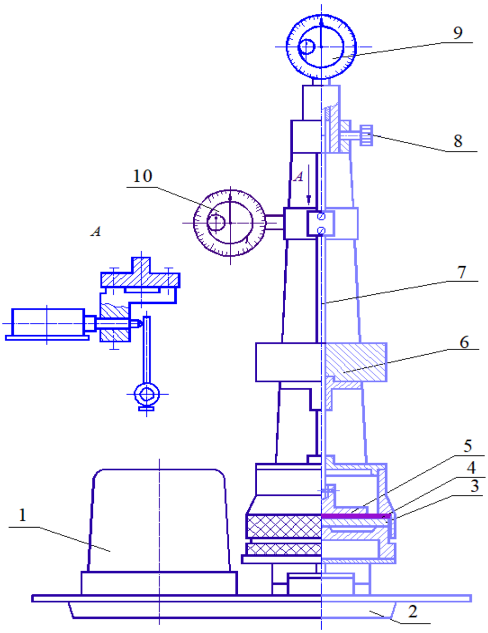

Fig. 4.5. Testing device

The device can obtain data to find the coefficient of friction μ and adhesive shear stress τ_a in accordance with the formula:

$$\tau = \mu\sigma + \tau_a \text{,} \tag{4.40}$$

where σ is the normal load on grease, Pa.

A different number of weights allows you to get several experimental points, which, according to the expression, are plotted on a graph with coordinates τ and σ, then by a known method find μ and τ_a .

The tests were carried out on the device described above with the following initial data: *d* = 43.7 mm; normal load *Q* = 25 N; lower disc speed 0.077 rpm; lever arm on the indicator *l* = 47.5 mm; graduation price of the indicator: 1 mm – 1.5 N; Fiol-3 grease.

After turning on the drive, rotation from the lower disk through the layer of lubricant was transferred to the upper disk until the beginning of full slip, when the upper disk stopped. The time point was observed from the beginning of rotation to complete slippage with fixation every 10 s of the readings of the force indicator (movement of the lever of the force-measuring device). The results of measurements and their processing are presented in Table. 4.3.

Table 4.3

Results of measurements and calculations of shear properties of Fiol-3

Time t, s	10	20	30	40	50	60
Indicator readings x, mm	2.3	4.2	5.2	5.5	5.7	6.0
Lower disc swing angle φ_2, rad	0.08	0.16	0.24	0.32	0.4	0.48
Upper disc rotation angle φ_2, rad	0.048	0.088	0.109	0.115	0.119	0.126
Displacement in the lubricant layer φ, rad	0.032	0.071	0.131	0.205	0.281	0.354
Frictional moment *M*, N·mm	16.4	29.9	37.05	39.18	40.6	42.7

A graphic interpretation of the dependence of the friction moment in the lubricant layer on the relative angular displacement is shown in Fig. 4.6.

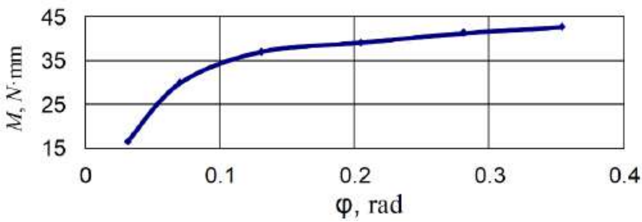

Fig. 4.6. Dependence of the friction moment on the angle of displacement of the grease layer

The parameters of dependence (4.18) can be found from experimental data using the least squares method or using the Excel program. Further, the parameters of the oil film shift function (4.21) are determined by the formulas (4.19) – (4.21). Determination of the parameters of the power-law approximation of the function. In accordance with (4.18), we will perform calculations according to (4.19). Let's take a look at the Table. 4.4 by two points: $M_1 = 16.4$, Н·мм; $\varphi_1 = 0.032$ рад; $M_2 = 42.7$, Н·мм; $\varphi_2 = 0.354$ рад.

By formula (4.19):

$$n = \frac{\lg\left(16.4 / 42.7\right)}{\lg\left(0.032 / 0.354\right)} = 0.3981 \cong 0.4 \;;$$

$$c_\varphi = \frac{16.4}{\left(0.032\right)^{0,3981}} = 64.56 \text{ N mm/(rad)}^n.$$

By formula (4.20), we find: $\alpha = n = 0.4$, and according to the formula (4.21):

$$G_0 = \frac{4 \cdot 64.56\left(0.4 + 3\right)}{\pi \cdot 43.7^3}\left(\frac{2 \cdot 0.001}{43.7}\right)^{0.4} = 61.57 \text{ Pa.}$$

The thickness of the film is taken to be 1 μm; in order to increase the accuracy of calculations, it must be determined experimentally. Thus, the shear diagrams of a thin layer from Fiol-3 grease are described by the dependence: $\tau = 61.57\gamma^{0,4}$ Pa.

In appearance, the curve of this function is similar to the curve in Fig. 3, since the exponents of these curves coincide $n = \alpha$.

Thus, based on the results of the research, the following conclusions can be drawn:

1. When studying the wear of surfaces under boundary lubrication conditions, it is necessary to know the stiffness characteristics of a thin layer of lubricant under normal and tangential stresses. Previous studies have examined the bulk mechanical properties of lubricants.

2. A method for determining the tangential stiffness properties of thin films is proposed. The method is based on twisting a round thin layer of grease between two rigid circular discs.

3. The contact mechanics of torsion of a thin circular lubricant layer has been developed and relations for determining the parameters of the shear diagram of a thin lubricant layer have been obtained.

4. A method for torsion testing of a thin lubricant layer with the determination of the parameters of the film shear diagram has been developed.

5. According to the developed method, the Fiol-3 grease was tested and the parameters of the shear diagram were determined.

4.3. Determination of the dynamic hardness of greases

Plastic lubricants in the range of lubricants are the most common. Greases are thick oily products, which include: oil, thickener, solid carbon and various additives. A distinctive feature of plastic lubricants is that they are able, depending on working conditions, to have the properties of both solid and liquid substances. Under the action of small loads, lubricants behave like a solid body, can be held on vertical and inclined surfaces. The efficiency of plastic oil is determined by the duration of its retention on the surface. Evaluation of the effectiveness of plastic lubricants depends on their mechanical properties. Among the characteristics of mechanical properties, one of the most important is the shear strength of the oil. After the destruction of the frame, the oil begins to deform and flow like a liquid. Resistance to the flow of grease is characterized by viscosity. Typically, viscosity is determined at a single fixed strain rate. In the materials science of solids, the value of hardness is accepted as one of the mechanical characteristics. Hardness is the value of the average pressure under the indenter, which stabilizes the plastic deformation. In the mechanics of lubricants, the number of penetrations is analogous to the hardness of the lubricant. The number of penetrations is determined by pressing the cone into the flat surface of the grease and is measured in tenths of a millimeter for 5 seconds. With the help of the penetration number it is possible to estimate the effect of oil deformation at different temperatures. The disadvantage is that the number of penetrations is determined at one time point in the process that develops over time. At other time points of the penetration process, data on the hardness of lubricants can be obtained as opposed to those obtained at a holding time of 5 s. Also, the number of penetration of oil is determined by the depth of indentation of the cone. For metals, hardness is defined as the ultimate pressure, which actually reflects the phenomenon of resistance to indenter indentation in the material.

Therefore, it is proposed to use the dependence of hardness on time when pressing the spherical indenter as one of the basic characteristics of the mechanical properties of plastic lubricants.

The method of determining the function of oil hardness is based on the mechanics of contact interaction of a solid ball and a plane presented in this work, which has the property of creep according to the flow theory.

The study of the tribological properties of greases in world science is given quite a lot of attention. Based on modern methods of experimental and theoretical research, new highly effective lubricants are synthesized. The behavior and properties of lubricants are modeled under various operating conditions, under heavy loads, high heat, extreme speeds.

In paper [28] three kinds of new conductive lubricating greases were prepared using lithium ionic liquids as the base oil and the polytetrafluoroethylene as the thickener. The conductivities and contact resistances of the prepared lubricating greases were investigated using the conductivity meter and the reciprocating ball-on-disk sliding tester. The results suggest that the prepared lubricating greases have high conductivities and excellent tribological properties. The high conductivities are attributed to ion diffusion or migration of the lithium ionic liquids with an external electric field, and the excellent tribological properties depend on the formation of boundary protective films.

The study [29] investigates grease film evolution with glass disc revolutions in rolling elastohydrodynamic lubrication (EHL) contacts. The evolution patterns of the grease films were highly related to the speed ranges and grease structures. The transference of thickener lumps, film thickness decay induced by starvation, and residual layer were recognized. The formation of an equilibrium film determined by the balance of lubricant loss and replenishment was analyzed. The primary mechanisms that dominate grease film formation in different lubricated contacts were clarified.

In [30] the grease film distribution under a pure rolling reciprocating motion is observed on a ball-disk test rig. It is found that the reciprocating motion reduces the accumulation of the thickener fiber gradually with time. The maximum film thickness forms around the stroke ends. The life of grease lubrication under a transient condition is far below that under steady-state conditions. When increasing the maximum entraining speed of the reciprocating motion to a certain value, during which the thickener fiber is not expected to accumulate under a steady-state condition.

In paper [31] the technique of relative optical interference intensity and simple numerical calculations were used to investigate the lubricating behavior of grease lubricant films. Experimental results indicate that at a same entrainment velocity of the inlet, the central film thickness under deceleration is larger than that under acceleration. The numerical method can also be used to explain the behavior of the grease lubricating film under non-steady state conditions.

Thermal-induced changes in the viscous and viscoelastic responses of lubricating greases have been investigated sn [32]. Small-amplitude oscillatory shear and viscous flow measurements were carried out on a model conventional lithium lubricating grease. Two different regions, below and above this critical temperature, in the plateau modulus versus temperature plot have been detected. From this thermal dependence, a much larger thermal susceptibility of the lubricating grease is apparent. The thermo-mechanical reversibility of this material has been studied by applying different combined stress–temperature protocols. The experimental results obtained have been explained on the basis of the thermo-mechanical degradation of the lubricating grease microstructure.

In [33] a methodology for continuous monitoring of grease degradation subjected to mechanical shearing is proposed. It is hypothesized that the mechanical degradation of grease is akin to the running-in process in a tribo-pair with both transient and steady-state regimes. From the results, a more effective method using the entropy generation rate is proposed for continuous monitoring of grease degradation. The proposed method is extended to estimate the time for a grease subjected to mechanical shearing to degrade to a lower grade. The efficacy of this method is demonstrated via long duration testing in a custom-built ball-bearing test apparatus.

The tribological properties of a lithium calcium complex grease based on calcium sulfonate complex and lithium complex greases are investigated in [34]. The tribological properties of the latter greases are compared using an Optimol SRV reciprocating friction and wear tester. The morphologies of the worn surfaces are traced by a scanning electron microscope (SEM) and the chemical states of several typical elements on the worn surfaces are examined by x-ray photoelectron spectroscopy (XPS). The results indicate that the new grease has a low friction coefficient and good wear-resisting ability.

The dependence of the colloidal stability, effective viscosity, penetration, and yield stress of low-temperature polymeric greases on the composition and characteristics of the dispersion medium was investigated in paper [35]. Various types of low-viscosity oil with known fractional and group composition were used as base oils. The effect of the concentration of the two-component thickener of high- or low-molecular polypropylene and the proportions of its components on the main physicochemical characteristics of the polymer greases was determined. The dependence of the structure and properties of the polymer greases on the concentration of lithium stearate was established.

Also, the scientific works of the authors [36-39] are devoted to various aspects of the use of greases in technical applications. At the same time, the analysis of studies has shown that little attention has been paid to the study of the deformation properties of greases under various conditions of tribological contact.

Contact mechanics of the process of interaction between the sphere and the viscoplastic lubricant. The direct formulation of the problem of the interaction of a solid ball of radius with a plane in a state of creep includes three relations (Fig. 4.7).

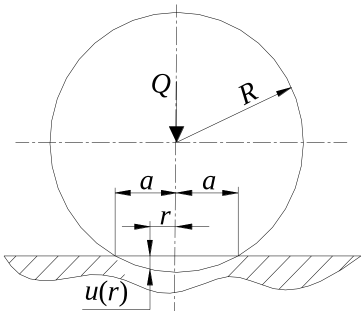

Fig. 4.7. The scheme of contact of a ball and a viscoplastic plane

1) the model of constant creep of the lubricant material has the form:

$$\frac{du_c}{dt} = k_c \sigma^{m_c} ; \qquad (4.41)$$

2) the condition of continuity in contact can be represented as:

$$u_c(t) = \frac{a^2(t) - r^2}{2R} ; \qquad (4.42)$$

3) equilibrium condition in contact:

$$Q = 2\pi \int_0^a \sigma(t, r)\, r dr , \qquad (4.43)$$

where $\sigma(t,r)$ is the time-dependent contact pressure distribution t; $a(t)$ is the radius of the circular area of contact; r is the radial coordinate.

Differentiating condition (4.42) and equating (4.41) we have:

$$\sigma(t)=\left(\frac{1}{k_c}\frac{a}{R}\frac{da}{dt}\right)^{\frac{1}{m_c}}, \tag{4.44}$$

it is obvious that the pressure is evenly distributed over the contact area.

Substituting this expression in condition (4.43), we obtain:

$$Q=2\pi\int_0^a\left(\frac{1}{k_c}\frac{a}{R}\frac{da}{dt}\right)^{\frac{1}{m_c}}rdr\,. \tag{4.45}$$

After integration we obtain a differential equation with respect to the function $a(t)$:

$$\left(\frac{Q}{\pi}\right)^{m_c}=a^{2m_c}\frac{a}{k_cR}\frac{da}{dt}\,. \tag{4.46}$$

Solving this equation, we have:

1) at $a(t=0)=0$:

$$a(t)=\left[\left(2m_c+2\right)k_cR\left(\frac{Q}{\pi}\right)^{m_c}t\right]^{\frac{1}{2m_c+2}}; \tag{4.47}$$

2) at $a(t=0)=a_0$:

$$a(t)=\left[\left(2m_c+2\right)\left(k_cR\left(\frac{Q}{\pi}\right)^{m_c}t+a_0^{2m_c+2}\right)\right]^{\frac{1}{2m_c+2}}. \tag{4.48}$$

With a uniform distribution of contact pressures we have:

$$\sigma(t)=\sigma_0(t)=\frac{Q}{\pi a^2(t)}\,. \tag{4.49}$$

The maximum displacement from creep is obtained at $r = 0$:

$$u_{c0}(t) = \frac{a^2(t)}{2R}. \qquad (4.50)$$

Example of calculating the size of the contact area when pressing the spherical indenter depending on (4.47).

Initial data:

1. Parameters of contact creep: $m_c = 1{,}82$; $k_c = 0{,}302$ МПа$^{-mc}$.
2. Spherical indenter radius $R = 6{,}35$ mm.
3. Indenter weight $Q = 1{,}9$ N.

Below are the results of the calculation obtained using the program MathCad.

t, min	2	3	7	17	37	67
$a(t)$, mm	1,47	1,58	1,83	2,14	2,46	2,73

Now suppose that the dependence of the radius of the contact $a(t)$ site on time is known from the experiment. It is necessary, using the solution of the direct problem, to determine the parameters k_c, m_c of the model of constant creep.

Consider the case of the initial zero contact site and present the experimental data in the form of a power approximation function:

$$a(t) = c_c t^{\beta_c}. \qquad (4.51)$$

Substituting (4.51) into (4.47), we obtain:

$$c_c^{2m_c+2} t^{\beta_c(2m_c+2)} = \left(2m_c + 2\right) k_c R \left(\frac{Q}{\pi}\right)^{m_c} t. \qquad (4.52)$$

From the condition that this equation is executable for any values of the argument t follows:

$$m_c = \frac{1 - 2\beta_c}{2\beta_c}. \qquad (4.53)$$

For the second parameter from (4.52):

$$k_c = \frac{c_c^{\frac{1}{\beta_c}} \beta_c}{R\left(\frac{Q}{\pi}\right)^{m_c}}. \tag{4.54}$$

The obtained results can be used to describe the contact creep of solid balls covered with thin deformed layers of lubricant, which is promising in creating tribomechanics of thin lubricating layers.

In the case of a nonzero initial contact site ($a_0 \neq 0$), it is necessary to determine the parameters of the creep model k_c, m_c given a experimental function:

$$a(t) = a_0 + a(t). \tag{4.55}$$

The solution of the problem is performed provided that the values of the two experimental points are known:

$$(a_1,\ t_1);\ (a_2,\ t_2) \tag{4.56}$$

at $a_0 < a_1 < a_2$; $0 < t_1 < t_2$.

The solution of the direct problem (4.47) for two points is presented in the form:

$$\left.\begin{aligned} a_1^{2m_c+2} - a_0^{2m_c+2} &= (2m_c+2) k_c R\left(\frac{Q}{\pi}\right)^{m_c} t_1, \\ a_2^{2m_c+2} - a_0^{2m_c+2} &= (2m_c+2) k_c R\left(\frac{Q}{\pi}\right)^{m_c} t_2. \end{aligned}\right\}. \tag{4.57}$$

Taking the ratio of equations, we obtain:

$$\frac{\alpha_1^{2m_c+2} - 1}{\alpha_2^{2m_c+2} - 1} = \frac{t_1}{t_2}, \tag{4.58}$$

where $\alpha_1 = \frac{a_1}{a_0}$; $\alpha_2 = \frac{a_2}{a_0}$. This nonlinear equation can be solved numerically.

Method for determination and research of dynamic hardness of plastic materials. The procedure for determining the parameters of the creep function of the oil at zero contact area is as follows.

The initial parameters of the process of pressing the ball into the surface of the grease are selected: R is the ball radius; Q is the load to ball. The ball is pressed into the surface of the oil with the measurement of the maximum depth of pressing u_{c0}.

Using formula (4.50), determine the radius of the area of contact of the ball with the surface of the oil:

$$a(t) = \left[2Ru_{c_0}(t)\right]^{\frac{1}{2}}. \tag{4.59}$$

The experimental dependence of the radius of the contact site on time is represented as a power function:

$$a(t) = c_c t^{\beta_c}. \tag{4.60}$$

Approximation parameters c_c, β_c are determined by the method of least squares. Parameters m_c, k_c models (4.41) of oil creep are determined by formulas (4.53) and (4.54). The procedure for determining the parameters of the dynamic hardness of the oil is as follows.

The hardness of the oil H_L or the average pressure on the ball on the oil side is determined by the relationship of type (4.49):

$$H_L(t) = \frac{Q}{\pi a^2(t)}. \tag{4.61}$$

If the value of the radius of the contact site is known from the experiment, the hardness is determined immediately by formula (4.61).

If parameters are known for oil m_c, k_c model of contact creep, the function of dynamic hardness is determined by substitution (4.47) in (4.61) at the initial zero contact area:

$$H_L(t) = \frac{Q}{\pi\left[(2m_c+2)k_c R\left(\frac{Q}{\pi}\right)^{m_c} t\right]^{\frac{1}{m_c+1}}}. \tag{4.62}$$

If it is necessary to compare the hardness of lubricants, functions are built $H_L(t)$. When the non-zero contact area is set by the initial data R, Q and a_0. Conduct tests and obtain data for the function: $a(t)=a_0+a\ (t)$. Two points are chosen for the function: $(a_1,\ t_1)$; $(a_2,\ t_2)$ and write for them equation (18) in the form:

$$\frac{\alpha_1^x-1}{\alpha_2^x-1}=\bar{t}_{12}, \tag{4.63}$$

where $x=2m_c+2$; $\bar{t}_{12}=t_1/t_2$.

Numerically solve equations (4.63). The dynamic hardness of the oil is determined from the expression (4.62).

Investigation of dynamic hardness of plastic materials and its connection with wear. To implement the method of determining the parameters of contact creep of plastic materials, studies of bitumen and plasticine were performed by pressing a spherical steel indenter with a diameter of 12.7 mm and a weight of 190 g. The results of research and calculations of the parameters of the contact creep model are given in Table 4.4 with graphical interpretation in Fig. 4.8.

Table 4.4

Test results for contact creep and determination of dynamic hardness of plastic materials

Material	Time t, min	Depth indentation, u_c, mm	The size of the contact area a_c, mm	Parameters approximations		Parameters models contact creep		Hrdness function, MPa
				c_c	β_c	m_c	k_c	
Plasticine	1	0,11	1,18	1,297	0,177	1,82	0,302	$H_L=0{,}361t^{-0{,}35}$
	2	0,18	1,5					
	3	0,23	1,7					
	7	0,29	1,9					
	17	0,36	2,14					
	37	0,47	2,44					
	67	0,55	2,64					
Bitumen	1	0,4	2,22	2,403	1,803	1,77	8,943	$H_L=0{,}106t^{-0{,}36}$
	2	0,7	2,89					
	7	1,15	3,64					
	27	1,7	4,32					
	47	2,02	4,64					

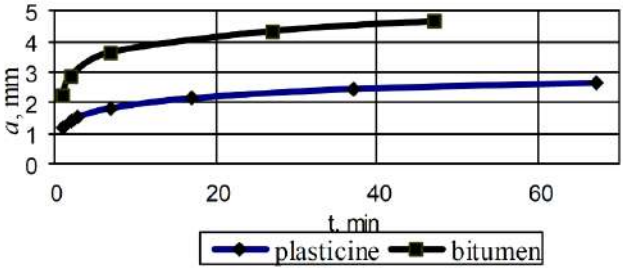

Fig. 4.8. The results of studies on contact creep

Results of tests of deformation properties of plastic oils by means of a ball with radius R = 15 mm are given in Table 4.5 with graphical interpretation in Fig. 4.9.

Table 4.5

Test results of deformation properties of plastic lubricants

t, min	Ball, d = 30 mm, m = 150 g			
	Litol-24		Solidol C	
	a, mm	Δa, mm	a, mm	Δa, mm
0,08	12,75	0	9,86	0
0,6	12,99	0,24	10,09	0,23
2,6	13,15	0,4	10,30	0,44
7,6	13,36	0,61	10,51	0,65
17,6	13,64	0,89	10,71	0,85
47,6	13,89	1,14	10,9	1,04
107,6	14,07	1,32	10,99	1,13
227,6	14,2	1,45	11,09	1,23
407,6	14,44	1,69	11,18	1,32

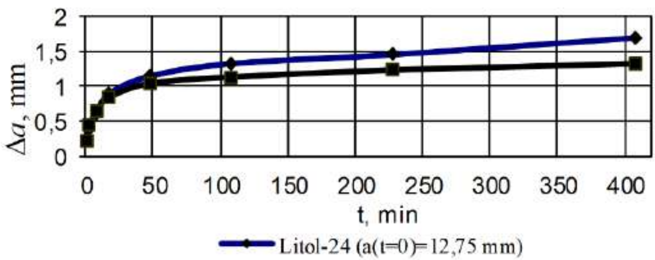

Fig. 4.9. The results of pressing the ball into the oil

The dependence (4.55) can be used to describe the process of pressing a cone and a ball with a non-zero initial contact pad.

As a result of processing the experimental data, the dependences for the contact site and the dynamic hardness when pressing the ball indenter into the surface of the plastic oil were obtained (Table 4.6).

Table 4.6

The results of determining the dynamic hardness for lubricants

Type of indentor	Solidol C	Litol –24
Steel ball, $R = 15$ mm	$a(t) = 9,86 + 0,334t^{0,258}$	$a(t) = 12,75 + 0,315t^{0,299}$
Dynamic hardness, MPA	$H_L(t) = Q/\pi a^2(t) = 0,48/a^2(t)$	

According to the obtained results, graphical dependences of hardness for two types of investigated plastic lubricants are constructed, shown in Fig. 4.10.

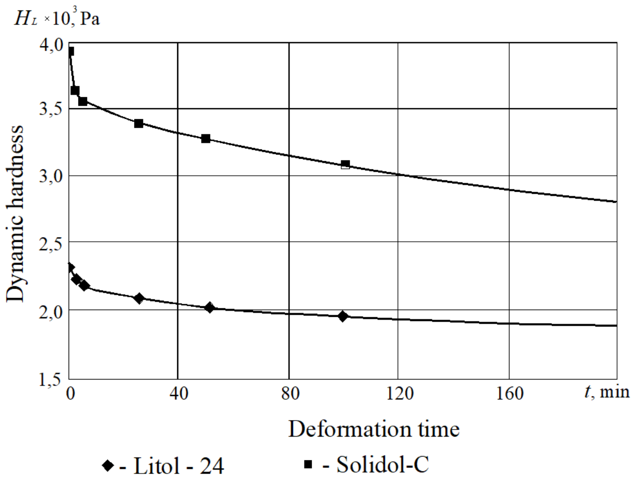

Fig. 4.10. Dynamic hardness of lubricants during deformation

Analysis of the obtained graphs shows that Litol-24 oil has a lower dynamic hardness, but is characterized by more stable indicators over time. With a durability of almost 3 hours, the hardness of Solidol-24 decreased by 40 %, while Litol-24 decreased by only 20 %, which indicates better stability of the load-bearing capacity of Litol-24 over time. The obtained dependences for the characteristic of dynamic hardness allow to analyze the processes of deformation of lubricating layers of different lubricants under the action of applied loads.

To analyze the influence of deformation properties on the tribological properties of lubricants, comparative tests of the two above-mentioned types of lubricants on a four-ball friction device were performed. (V = 0.45 m/s; N = 350 N). As a result, the dependences of wear on the test time are obtained (Fig. 4.11).

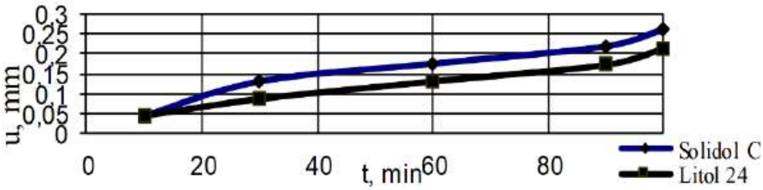

Fig. 4.11. Results of tribological tests of lubricants

It was found that Litol-24 oil has the best wear resistance. The nonlinear period of running in for this oil is practically absent that, obviously, under the given conditions of tests is connected with more stable in time deformation properties.

Thus, based on the results of the research, the following conclusions can be drawn:

1. One of the main methods of testing the deformation properties of plastic lubricants is to determine the number of penetrations. The essence of this method is to measure the depth of indentation of the conical indenter in the surface of the lubricant sample. The main disadvantages of this method are the following:

– the number of penetration is determined at one time point of the indenter indentation process, when measurements at other time points will be obtained data on the deformation of lubricants opposite to those obtained at a holding time of 5 s;

– the number of penetration of oil is determined by the depth of indentation of the indenter; more informative for such a process is the ultimate pressure, which actually reflects the phenomenon of resistance to indenter indentation in the material.

2. A more informative characteristic of the deformation properties of plastic materials is proposed – a function of dynamic hardness, which shows the dependence of the pressure of resistance to indenter indentation on the time of deformation.

3. To establish the analytical dependence for dynamic hardness, the mechanics of contact interaction of a rigid indenter in the form of a ball with plastic lubricant, which has the property of creep, is considered. Solved direct and inverse problems and recommendations for their use.

4. For uniform distribution of pressure under a spherical indenter the technique of construction of function of dynamic hardness of plastic materials is defined and on the basis of tests results of construction of dynamic hardness are received.

5. Tests on contact creep of plastic lubricants are carried out, functions of dynamic hardness are received and the analysis of influence of character of change of dynamic hardness on wear processes in the presence of lubricants is carried out.

6. The offered characteristic of dynamic hardness and a method of its definition allows to estimate and compare deformation and tribological properties of various plastic materials at certification control, operation and creation of new types of oils..

4.4. Heat and mass transfer models at boundary lubrication to determine the transition temperatures

At ultimate friction, the reduction of friction and wear of surfaces is due to the ability of the lubricant to form layers of adsorption or chemical origin on the surface. At the first stage (Fig. 4.12) of interaction of the surface and the lubricant, the adsorbed layer is formed by molecules of the surfactant component. Adsorbed films under certain conditions have the ability to self-organize, ie there is a process of dynamic equilibrium between the formation and destruction of adsorbed layers under the action of external factors. When the value of the first transition temperature is reached, the dynamic equilibrium is disturbed and the adsorption layers are destroyed. Most modern lubricants contain chemically active components, which at the temperature of chemical modification form chemically modified films on the metal surface, which leads to reduced friction and wear. Further increase of external influence leads to complete destruction of the boundary lubricating layer at the second critical temperature.

Analytical models of transition temperatures and wear in the limit lubrication mode must be used to mathematically describe the processes in the subsystems and the transition between them.

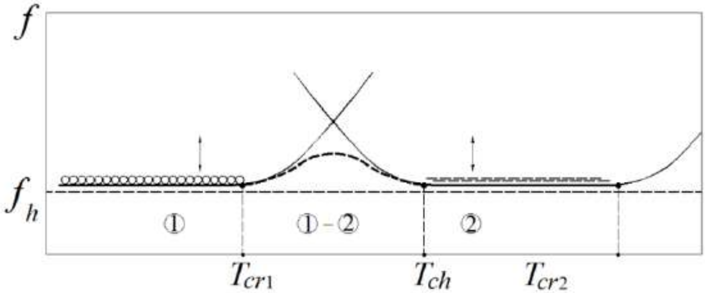

Fig.4.12. The kinetics of the formation of transition temperatures

Much attention is currently being paid to the study of models of heat and mass transfer during boundary lubrication. The heat transfer phenomenon is beneficial and applicable in engineering, industries, and technological processes. The production of energy with the help of some cheap resources plays a pivotal and renewable role in the industrial development of the countries.

In study [40] proposes a torque calculation model that incorporates the boundary conditions of the lubricant flow field and variation of oil film temperature. The torque transfer equation of a multi-plate clutch as related to viscosity was derived by combining the three-dimensional Navier-Stokes equation with the boundary conditions of the lubricant flow field. Taking the vehicle transfer case as an example, the equation for the variation in oil film radial temperature was obtained through the thermodynamic model of a flow field. By applying the parameters derived from the temperature equation to the PWA torque transfer model, the values under four working conditions were calculated. The results show that the relative errors between the corrected torque value and the test value under the four working conditions were less than 10 %.

Comparative analysis of simulation and experiment shows that PWA has advantages. In paper [41] the owing to such a significant performance of heat transfer, the steady slip flow and heat transfer of tangent hyperbolic fluid over a lubricating surface of the stretchable rotatory disk is investigated. The governing nonlinear partial differential equations (PDEs) have been converted into ordinary differential equations (ODEs), which are solved numerically using the Keller-box method. The upshots of pertinent parameters upon the dimensionless distributions of velocity and temperature are deliberated.

The surface drag forces and heat transfer rates are computed, and the effects of governing parameters on them are examined. In [42] the lubrication of the piston skirt-cylinder interface involves multiple physical fields, and these physical fields are coupled. A new method is proposed in this study for modeling and analysis of the lubricated piston skirt-liner interface with multi-physics coupling. The results indicate that although a thinner skirt will affect the stability of piston motion and increase the slapping noise and wear, it will benefit hydrodynamic lubrication between skirt and cylinder and reduce friction power loss.

In study [43] the influence of two thermal effects in a low-speed two-stroke diesel engine on piston ring lubrication performance are discussed in detail. For the TDCL, a steady-state heat-transfer model based on sequential fluid-solid coupling is used to solve for the heat-transfer coefficient and temperature on the coupling surface between the cylinder liner and the cooling water jacket. The boundary condition used to calculate the TDCL is the temperature distribution on the inner surface of the cylinder liner calculated empirically and verified experimentally. The results of the TDCL and the ASTM model are used in the lubrication model to analyze how the thermal effects influence the lubrication performance of the piston-ring-liner tribological pair. A fluid-structure coupling numerical model of an oil-jet lubricated cylindrical roller bearing (CRB) in a high-power gearbox is developed, in which the volume of fluid (VOF) method and slip mesh model are used. The heat sources of bearing are defined as the transient thermal boundary in [44].

The differences of temperatures between the rigid and flexible bearings are compared. The simulation results are validated by the presented experimental results. It indicates that the oil flow rate, speed, waviness amplitude and order, oil viscosity and nozzle number will significantly influence the bearing’s lubricating characteristics. The flexible bearing model with the transient thermal boundary is more accurate than those of other two models. To suppression the increment of bearing temperature, the waviness should be reduced. Advancements in mechanical expertise and rigorous need for gyratory components of machines expedite scientists towards essentiality of the eternal evolution of modified lubricants to corroborate the reliability, innocuous procedure and stability of sundry bearings. To enhance the performances at heftily ponderous load and high velocity, the high molecular polymers are utilized in mechanical bearings as lubricant.

These lubricants [45] are non-Newtonian in characteristics and comply with different constitutive relationships. One of them is the power law lubricant which complies with Ostwald model and is broadly utilized for the engineering lubrication. The derivation of the slip-flow conditions at the interface of bulk Jeffrey fluid and the thin layer non-Newtonian lubricant is performed over a disk spiraling with simultaneous radial stretching and rotation. To obtain a homogeneous solution, the power-law index is suggested 1/3 and no-slip boundary condition is converted into an incipient slip boundary condition. A single dimensionless slip parameter is introduced to regulate the velocity slip. Flow equations are obtained, and the similarity conversion is performed to obtain ordinary differential equations. Numerical results are computed to visually perceive the effects of lubrication on the flow field by incorporating the interfacial slip conditions. The presence of the lubrication enhances the fluid velocity and plays major role in the reduction of the skin friction at disk surface. Thus, the creation of models of heat and mass transfer during boundary lubrication is a modern problem.

Main material. Models of the formation of transition temperatures during boundary lubrication. The gradient law of Fourier thermal conductivity can be used in the formation of boundary oil films:

$$q_t = -\lambda \Delta T = -\lambda g_t \, , \tag{4.64}$$

where q_t is the heat gradient;

$g_t = \mathrm{grad} T = \nabla T$ is the temperature gradient;

λ is the thermal conductivity [50].

To summarize Fourier's law, the Maxwell–Cattaneo relationship:

$$q_t = -\lambda g_t - \tau_t \frac{\partial q_t}{\partial \tau_t} \, , \tag{4.65}$$

where τ_t is the time or period of relaxation of the temperature field.

It is established [44, 45] that the isotropic solid under the conditions of lubrication is affected by the hyperbolic equation of heat transfer:

$$\frac{\partial T}{\partial \tau} + \tau_t \frac{\partial^2 T}{\partial \tau^2} = \alpha \Delta T + \frac{\gamma_t}{\rho c_p} \, , \tag{4.66}$$

where ρ is the the density of the lubricating film;

c_p is the її molar heat capacity;

γ_t is the density of distribution of heat energy drains.

The solution of equation (4.66) with the necessary initial and boundary conditions corresponds to the propagation of the temperature field with a sharply delineated front, which propagates with velocity:

$$V_t = \sqrt{\frac{a}{\tau_t}},$$

where a is the coefficient of thermal conductivity.

$$a = \frac{\lambda}{\rho c_p}. \tag{4.67}$$

Therefore, equation (4.63) describes the process of heat propagation with a finite velocity V_t.

However, the process of heat distribution in the formation of lubricating films is not Markov, ie the magnitude of heat flux is determined by the entire "history" of heat transfer in some elementary volume.

With this approach, the equation of the relationship between heat flux and temperature gradient will take the form:

$$g_t = -\int_0^{\Delta T} k(\theta) g(\tau - \theta) d\theta, \tag{4.68}$$

where $k(\theta)$ is the lubrication film temperature field relaxation function;

τ, θ is the coordinates of this field.

If $g(\tau - \theta) = g(\tau)$, then equation (4.68) passes into (4.64), and:

$$\lambda = \int_0^{\Delta T} k(\theta) d\theta. \tag{4.69}$$

Assuming that the relaxation $k(\theta)$ function attenuates exponentially, i.e.:

$$k(\theta) = \frac{\lambda}{\tau_t} \exp\left(-\frac{\theta}{\tau_t}\right), \tag{4.70}$$

you can go from (4.68) to (4.65).

The heat flux q_t and internal energy e of the film, taking into account the relaxation functions, can be found as follows:

$$\begin{cases} q_t = -\int\limits_0^{\Delta T} k(\theta) g'(\theta) d\theta; \\ e = e_0 + cT - \int\limits_0^{\Delta T} l'(\theta) T'(\theta) d\theta, \end{cases} \tag{4.71}$$

Where value $g'(\theta)$ and $T'(\theta)$ determined by the ratios:

$$\begin{cases} \frac{d}{d\theta} g'(\theta) = g(\tau - \theta); \\ \frac{d}{d\theta} T'(\theta) = T(\tau - \theta) \end{cases}, \tag{4.72}$$

where c is the volumetric heat capacity of the oil;

$l(\theta)$ is the relaxation function of internal energy [43, 44].

Find the time derivatives of heat flux and internal energy:

$$\begin{cases} \frac{\partial q_t}{\partial \tau} = -k(\theta) g - \int\limits_0^{\Delta T} k'(\theta) g(\tau - \theta) d\theta; \\ \frac{\partial e}{\partial \tau} = c \frac{\partial T}{\partial \tau} + l(\theta) T + \int\limits_0^{\Delta T} l'(\theta) T(\tau - \theta) d\theta. \end{cases} \tag{4.73}$$

Using the conservation equation for the internal energy in the form:

$$\frac{\partial e}{\partial \tau} = div q_t + \gamma_t, \tag{4.74}$$

we obtain the following integro-differential equation of heat transfer in the lubricating film, considering the lubricant an isotropic material:

$$c\frac{\partial^2 T}{\partial\tau^2}+l(\theta)\frac{\partial T}{\partial\tau}+\int_0^{\Delta T} l'(\theta)\frac{\partial T(\tau-\theta)}{\partial\tau}d\theta=k(\theta)\Delta T+\int_0^{\Delta T} k'(\theta)\Delta T(\tau-\theta)d\theta+\gamma_t\,. \quad (4.75)$$

The heat flux determined by relation (4.68) does not explicitly depend on the instantaneous value of the temperature gradient, but is determined by the entire "history" of heat transfer. However, in explicit form, equation (4.68) will have the form:

$$q_t=-k(\theta)g-\int_0^{\Delta T} k'(\theta)g(\tau-\theta)d\theta\,. \quad (4.76)$$

If we use the equation for the internal energy of the film in the form:

$$l=e_0+l(\theta)T+\int_0^{\Delta T} l'(\theta)T(\tau-\theta)d\theta\,, \quad (4.77)$$

then equation (4.75) will take the form:

$$l(\theta)\frac{\partial T}{\partial\tau}+\int_0^{\Delta T} l'(\theta)\frac{\partial T(\tau-\theta)}{\partial\tau}d\theta=k(\theta)\Delta T+\int_0^{\Delta T} k'(\theta)\Delta T(\tau-\theta)d\theta+\gamma_t\,. \quad (4.78)$$

At $k(\theta)\to 0$ this equation will take the form:

$$l(\theta)\frac{\partial T}{\partial\tau}+\int_0^{\Delta T} l'(\theta)\frac{\partial T(\tau-\theta)}{\partial\tau}d\theta=\int_0^{\Delta T} k'(\theta)\Delta T(\tau-\theta)d\theta+\gamma_t\,. \quad (4.79)$$

Equation (4.79) can be represented in the form close to (4.75):

$$l(\theta)\frac{\partial^2 T}{\partial\tau^2}+l'(\theta)\frac{\partial T}{\partial\tau}+\int_0^{\Delta T} l''(\theta)\frac{\partial T(\tau-\theta)}{\partial\tau}d\theta=k'(\theta)\Delta T+\int_0^{\Delta T} k''(\theta)\Delta T(\tau-\theta)d\theta+\gamma_t\,. \quad (4.80)$$

Equation (4.80) can be considered a mathematical model of the phenomenon of heat transfer by the lubricating film up to the formation of its limit state at temperature T_{cr1}, determined according to [70, 71] ($T_{cr1}=\Delta T$).

The equation of motion of the lubricating film on the surface of the lubricated body is obtained from the equation of motion for the Newtonian continuous medium [11]:

$$\frac{\partial v}{\partial \tau} + (\nabla v)v = g - \frac{1}{\rho}\nabla p + \frac{\mu}{\rho}\Delta v + \frac{1}{\rho}\left(\xi + \frac{1}{3}\mu\right)\text{grad div } v, \quad (4.81)$$

where p is the contact stresses in the lubrication zone;

v is the the average speed of movement of the lubricating film on the body surface;

μ is the chemical potential of the surface [74];

ξ is the chemical potential reduction factor.

In the case of uncompressed solid medium in the oil, when the value $\text{grad div } V$ rather small, equation (4.81) turns into the Navier–Stokes equation:

$$\frac{\partial v}{\partial \tau} + (\nabla v)v = g - \frac{1}{\rho}\nabla p + \frac{\mu}{\rho}\Delta v. \quad (4.82)$$

In mathematical modeling of the processes of physicochemical transformations of the lubricating film until the values are reached T_{ch} i T_{cr2} we will analyze the phenomenon of mass transfer in the film itself. To do this, we use Fick's diffusion law [73–75]:

$$q = -De\Delta\rho, \quad (4.83)$$

where De is the effective diffusion coefficient;

q is the irreversible flow of mass transfer.

Lubrication filtration transfer in the first approximation obeys Darcy's law, [44]:

$$v = -\frac{k}{\mu}\nabla p, \quad (4.84)$$

where k is the the permeability coefficient of the porous surface structure;

μ is the dynamic viscosity coefficient of the lubricating film;

v is the average mass transfer rate of wear products.

From (4.83) and (4.84) after the corresponding transformations we obtain the mass transfer equation with a lubricating film:

$$\varepsilon\frac{\partial \rho}{\partial \tau} = De\Delta\rho + \frac{k}{\mu}\nabla(\rho\nabla\rho) - \frac{k}{\mu}g\nabla\rho^2 + \nu, \quad (4.85)$$

where ε is the porosity or relative fraction of voids of the lubricant:

$$\varepsilon = \lim_{V\to 0}\frac{V - V_s}{V}, \tag{4.86}$$

where V is the the volume of the element of the porous structure;

V_s is the the total volume of the rigid frame of the same element;

ν is the density of surface bodies, $\nu = \rho g$;

g is the acceleration of gravity.

The transfer potential in the process of mass transfer is the chemical potential μ_i transferable component. The chemical potential is related to the concentration of the component ρ_i, with:

$$\nabla\mu_i = \left(\frac{\partial\mu_i}{\partial\rho_i}\right)_{p,T}, \quad \nabla\rho_i + \left(\frac{\partial\mu_i}{\partial T}\right)_{\rho_i,T}, \ \nabla T + \left(\frac{\partial\mu_i}{\partial\rho}\right)_{\rho_i,p}\nabla p. \tag{4.87}$$

For mass transfer at constant pressure, contact stresses and in isothermal conditions:

$$\nabla\mu_i = \left(\frac{\partial\mu_i}{\partial\rho_i}\right)_{p,T}\nabla\rho_i, \tag{4.88}$$

If the deviations of our system from the state of thermodynamic equilibrium are not so large, then the mass transfer flow can be described by a linear gradient law:

$$q_{mi} = -K\nabla\mu_i = -K\left(\frac{\partial\mu_i}{\partial\rho_i}\right)_{p,T}\nabla\rho_i = -D_i\nabla\rho_i. \tag{4.89}$$

Ziegler, [50], showed that the principle of thermodynamics of irreversible processes in combination with the principle of the smallest irreversible forces gives the maximum speed of dissipation. The speed of dissipation (dissipative function of the system) is determined by the ratio:

$$D(q_m) = \frac{dW}{d\tau} = g(q_m)q_m, \tag{4.89*}$$

where $g(q_m)$ is the generalized thermodynamic force that is proportional to the gradient of chemical potential.

Dissipative function can be introduced without the aid of irreversible force:

$$D(q_m) = T\left(\frac{dS}{d\tau}\right)_{ir} \geq 0, \tag{4.90}$$

де $\left(\frac{dS}{d\tau}\right)_{ir}$ is the entropy flow due to the irreversible process of mass transfer.

The principle of maximum speed of dissipation requires ensuring the maximum $D(q_m) = g(q_m)q_m$ due to the appropriate choice of transfer flow in the presence of restrictions on the species $F(q_m) = 0$. We get the solution from the relation:

$$\frac{\partial}{\partial q_m}\left[g(q_m)q_m - \lambda F(q_m)\right] = 0. \tag{4.91}$$

Condition $F(q_m) = 0$, де $F(q_m) = D(q_m) - g(q_m)q_m$ is a condition for the stability of the process of transition of the system to a state of thermodynamic equilibrium. From relation (4.91) it follows that:

$$g(q_m) = \frac{\lambda}{1+\lambda}\frac{\partial D}{\partial q_m}. \tag{4.92}$$

Determining the Lagrange multiplier λ, can be obtained:

$$g(q_m) = \left(\frac{\partial D}{\partial q_m}\right)^{-1} D\frac{\partial D}{\partial q_m}. \tag{4.93}$$

Dissipative functions of homogeneous processes satisfy the functional equation:

$$\frac{\partial D}{\partial q_m}q_m = f(D). \tag{4.94}$$

The condition of stability has the form:

$$f(D) > D \text{ при } D > 0. \tag{4.95}$$

Possible dissipative functions for the mass transfer process must be solutions of equation (31) with condition (4.95).

A special case (31) is equation:

$$\frac{\partial D}{\partial q_m} q_m = \alpha D. \tag{4.96}$$

The stability condition (4.95) in this case will be:

$$\alpha > 1. \tag{4.97}$$

Equation (4.93) can be converted by (4.94) into a more convenient relationship:

$$g\left(q_m\right) = \frac{D}{f\left(D\right)} \cdot \frac{\partial D}{\partial q_m}. \tag{4.98}$$

The solution of functional equation (4.97) will be the dissipative function of the form:

$$D = \mathrm{const} \cdot q_m^{\alpha}, \;\; \alpha > 1. \tag{4.99}$$

Using equations (4.98) and (4.99) we can obtain the following relationships between the gradient of chemical potential and mass transfer flow:

$$g = \mathrm{const} \cdot q_m^{\alpha - 1}, \; \alpha > 1. \tag{4.100}$$

Non-Markov process confirms that the magnitude of the mass transfer flow is determined by the entire "history" of mass transfer:

$$q_m = -\int_0^{\Delta T} M(\theta) g^n (\tau - \theta) d\theta, \;\; n \le 1. \tag{4.101}$$

If we explicitly determine the dependence of the magnitude of the transfer flux on the instantaneous value of the gradient of the chemical potential, the relationship (4.101) will take the form:

$$q_m = -M(\theta) g^n - \int_0^{\Delta T} M' g^n (\tau - \theta) d\theta, \quad n \le 1. \tag{4.102}$$

Assumptions about the exponential attenuation of the relaxation function, i.e.:

$$M(\theta) = \frac{m}{\tau_m} \exp\left(-\frac{\theta}{\tau_m}\right), \tag{4.103}$$

converts (4.102) into a ratio of the form:

$$q_m = -[M(\theta) + m]g^n - \tau_m \frac{\partial q_m}{\partial \tau}. \tag{4.104}$$

In formulas (4.101) – (4.104) g is thegradient of the chemical potencial.

Therefore, formulas (4.85) – (4.104) represent a mathematical model of the actual mass transfer of the lubricating film in the formation of its limit state. From formulas (4.85) – (4.104) follows the value T_{ch} and T_{cr2} [47, 48].

The nonlinear models of heat and mass transfer for determination transition of temperatures by forming boundary lubricant film according to the conception of structure-thermodynamic approach of description the process of boundary lubricating is developed.

References for Chapter 4

1. Miguel A. Garcia, Luís Augusto Mendes Veloso, Fabio Comes de Castro, José Alexander Araújo, Jorge L.A. Ferreira, Cosme Roberto Moreira da Silva. Experimental device for fretting fatigue tests in 6201 aluminum alloy wires from overhead conductors, Wear. Vol. 460–461, 2020. https://doi.org/10.1016/j.wear.2020.203448.

2. Nitschke, S., Wollmann, T., Ebert, C., Behnisch, T., Langkamp, A., Lang, T., Johann, E., Gude, M. An advanced experimental method and test rig concept for investigating the dynamic blade-tip/casing interactions under engine-like mechanical conditions, Wear. Vol. 422–423, 2019. Pp. 161–166. https://doi.org/10.1016/j.wear.2018.12.072.

3. Siefert, J. A., Babu, S. S. Experimental observations of wear in specimens tested to ASTM G98, Wear. Vol. 320, 2014. Pp. 111–119. https://doi.org/10.1016/j.wear.2014.08.017.

4. Surya Rajan, B., Sai Balaji, M.A. & Velmurugan, C. Correlation of field and experimental test data of wear in heavy commercial vehicle brake liners. Friction 5, Pp. 56–65 (2017). https://doi.org/10.1007/s40544-017-0138-x.

5. Ciulli, E. Experimental rigs for testing components of advanced industrial applications. Friction **7**. Pp. 59–73 (2019). https://doi.org/10.1007/s40544-017-0197-z.

6. Bortoleto, E. M., Rovani, A. C., Seriacopi, V., Profito, F. J., Zachariadis, D. C., Machado, I. F., Sinatora, A., Souza, R. M. Experimental and numerical analysis of dry contact in the pin on disc test, Wear, Vol. 301, Issues 1–2, 2013, Pp. 19–26, https://doi.org/10.1016/j.wear.2012.12.005.

7. Xue, Y., Chen, J., Guo, S. *et al.* Finite element simulation and experimental test of the wear behavior for self-lubricating spherical plain bearings. *Friction* 6, 297–306 (2018). https://doi.org/10.1007/s40544-018-0206-x.

8. Chuhan, Wu, Peilei, Qu, Liangchi, Zhang, Shanqing, Li, Zhenglian, Jiang. A numerical and experimental study on the interface friction of ball-on-disc test under high temperature, Wear, Vol. 376–377, Part A, 2017, Pp. 433–442, https://doi.org/10.1016/j.wear.2016.11.035.

9. Maksim Antonov, Irina Hussainova. Experimental setup for testing and mapping of high temperature abrasion and oxidation synergy. Wear, Vol. 267, Issue 11, 2009, P. 1798-1803, https://doi.org/10.1016/j.wear.2009.01.008.

10. Takabi, Jafar, Khonsari, M. M. Experimental testing and thermal analysis of ball bearings, Tribology International, Vol. 60, 2013, Pp. 93–103, https://doi.org/10.1016/j.triboint.2012.10.009.

11. Steven Chatterton, Paolo Pennacchi, Andrea Vania, Andrea De Luca, Phuoc Vinh Dang. Tribo-design of lubricants for power loss reduction in the oil-film bearings of a process industry machine: Modelling and experimental tests, Tribology International, Vol. 130, 2019, Pp. 133–145, https://doi.org/10.1016/j.triboint.2018.09.014.

12. Bielsa, J. M., Canales M., Martínez, F. J., Jiménez, M. A. Application of finite element simulations for data reduction of experimental friction tests on rubber–metal contacts, Tribology International, Vol. 43, Issue 4, 2010, Pp. 785–795, https://doi.org/10.1016/j.triboint.2009.11.005

13. Guido Belforte, Terenziano Raparelli, Vladimir Viktorov, Andrea Trivella, Federico Colombo. An experimental study of high-speed rotor supported by air bearings: test RIG and first experimental results, Tribology International, Vol. 39, Issue 8, 2006, Pp. 839–845, https://doi.org/10.1016/j.triboint.2005.07.013.

14. Dykha, A. Marchenko, D. Prediction the wear of sliding bearings. International Journal of Engineering & Technology. 2018. Vol. 7. No. 2.23. Pp. 4–8. DOI: 10.14419/ijet.v7i2.23.11872.

15. Dykha, A. V., Marchenko, D. D. & Dytynyuk, V. A. Determination of the Parameters of the Wear Law Based on the Results of Laboratory Tests. *J. Frict. Wear* 41, 153–159 (2020). https://doi.org/10.3103/S1068366620020038.

16. Dykha, A., Artiukh, V., Sorokatyi, R., Kukhar, V., & Kulakov, K. (2021). Modeling of wear processes in a cylindrical plain bearing. In Advances in Intelligent Systems and Computing (Vol. 1259 AISC, pp. 542–552). Springer. https://doi.org/10.1007/978-3-030-57453-6_52.

17. Dykha, A., Padgurskas, J., Musial, J., Matiukh, S. Wear models and diagnostics of cylindrical sliding tribosystem. Monograph. Bydgoszcz: Foundation of Mechatronics Development, 2020, 196 p. http://znm.khnu.km.ua/wp-content/uploads/sites/23/2020/12/Wear_Models_and_Diagnostics.pdf.

18. Dykha, A. V., Kuzmenko, A. G. Journal of Friction and Wear, 2, 138 (2015).

19. Khan, Z. A., Chacko, V. & Nazir, H., Friction, 5, 1 (2017). https://doi.org/10.1007/s40544-017-0143-0.

20. Wang, Z., Shen, X., Chen, X., et al., Friction, 7, 237 (2019). https://doi.org/10.1007/s40544-018-0208-8.

21. Li, X., Guo, F., Poll, G., et al., Friction, 9, 179 (2021).

22. Schwack, F., Bader, N., Leckner, J., Demaille, C., Poll, G., Wear, V. 454–455, 203335 (2020).

23. Fan, X., Li, W., Li, H., Zhu, M., Xia, Y., Wang, J. Tribology International, 118, 128 (2018).

24. Ghezzi, I., Tonazzi, D., Rovere, M., Coeur, C. Le, Berthier, Y., Massi, F. Tribology International, Vol. 155, 106788 (2021).

25. Vengudusamy, B., Enekes, C., Spallek, R., Tribology International, 129, 323 (2019).

26. Tonazzi, D., Komba, E. Houara, Massi, F., Jeune, G. Le, Coudert, J. B., Maheo, Y., Berthier, Y. Wear, 376 B, 1164 (2017).

27. Wang,D., Yang, J., Wei, P., Pu, W. Tribology International, 154, 106710 (2021).

28. Fan, X., Xia, Y. & Wang, L. Tribological properties of conductive lubricating greases. Friction 2, 343–353 (2014). https://doi.org/10.1007/s40544-014-0062-2.

29. Li, X., Guo, F., Poll, G. et al. Grease film evolution in rolling elastohydrodynamic lubrication contacts. Friction 9, 179–190 (2021). https://doi.org/10.1007/s40544-020-0381-4.

30. Han, Y., Wang, J., Wang, S. et al. Response of grease film at low speeds under pure rolling reciprocating motion. Friction 8, 115–135 (2020). https://doi.org/10.1007/s40544-018-0250-6.

31. Li, G., Zhang, C., Luo, J. et al. Film-Forming Characteristics of Grease in Point Contact Under Swaying Motions. Tribol Lett 35, 149 (2009). https://doi.org/10.1007/s11249-009-9455-1.

32. Delgado, M. A., Valencia, C., Sánchez, M. C. et al. Thermorheological behaviour of a lithium lubricating grease. Tribol Lett 23, 47–54 (2006). https://doi.org/10.1007/s11249-006-9109-5.

33. Lijesh, K. P., Khonsari, M. M. On the Assessment of Mechanical Degradation of Grease Using Entropy Generation Rate. Tribol Lett 67, 50 (2019). https://doi.org/10.1007/s11249-019-1165-8.

34. Xia, Y., Wen, Z. & Feng, X. Tribological Properties of a Lithium-Calcium Grease. Chem Technol Fuels Oils 51, 10–16 (2015). https://doi.org/10.1007/s10553-015-0569-x.

35. Zaichenko, V., Kolybel'skii, D.S., Popov, P.S. et al. Composition, Properties, and Structure of Low-Temperature Lubricating Greases Based on Polymeric Thickener. Chem Technol Fuels Oils 54, 531–540 (2018). https://doi.org/10.1007/s10553-018-0956-1.

36. Ren, G., Zhang, P., Ye, X. et al. Comparative study on corrosion resistance and lubrication function of lithium complex grease and polyurea grease. Friction 9, 75–91 (2021). https://doi.org/10.1007/s40544-019-0325-z

37. Ge, X., Xia, Y., Shu, Z. et al. Erratum to: Conductive grease synthesized using nanometer ATO as an additive. Friction 3, 352 (2015). https://doi.org/10.1007/s40544-015-0085-3

38. Wang, Z., Shen, X., Chen, X. et al. Experimental investigation of EHD grease lubrication in finite line contacts. Friction 7, 237–245 (2019). https://doi.org/10.1007/s40544-018-0208-8.

39. Huang, L., Guo, D., Wen, S. et al. Effects of Slide/Roll Ratio on the Behaviours of Grease Reservoir and Film Thickness of Point Contact. Tribol Lett 54, 263–271 (2014). https://doi.org/10.1007/s11249-014-0301-8

40. Liang, X., Chen, L., Wang, Y. A proposed torque calculation model for multi-plate clutch considering boundary lubrication conditions and heat transfer. International Journal of Heat and Mass Transfer, Volume 157, 2020, 119732, ISSN 0017-9310. https://doi.org/10.1016/j.ijheatmas/stransfer.2020.119732.

41. Khan, U. W., Badruddin, I. A., Ghaffari, A., Ali, H. M. Heat transfer in steady slip flow of tangent hyperbolic fluid over the lubricated surface of a stretchable rotatory disk. Case Studies in Thermal Engineering, Volume 24, 2021, 100825, ISSN 2214-157X. https://doi.org/10.1016/j.csite.2020.100825.

42. Zhao, B., Hu, X., Li, H., Si, X., Dong, Q., Zhang, Z., Zhang, B. A new approach for modeling and analysis of the lubricated piston skirt-cylinder system with multi-physics coupling. Tribology International, Vol. 167, 2022, 107381. https://doi.org/10.1016/j.triboint.2021.107381.

43. Jiao, B., Li, T., Ma, X., Wang, C., Xu, H., Lu, X., Liu, Z. Lubrication analysis of the piston ring of a two-stroke marine diesel engine considering thermal effects. Engineering Failure Analysis, Vol. 129, 2021, 105659, ISSN 1350-6307. https://doi.org/10.1016/j.engfailanal.2021.105659.

44. Liu, J., Xu, Z. A simulation investigation of lubricating characteristics for a cylindrical roller bearing of a high-power gearbox. Tribology International, Vol. 167, 2022, 107373. https://doi.org/10.1016/j.triboint.2021.107373.

45. Sadiq, M. N., Sajid, M., Javed, T., Ali, N. Modeling and simulation for estimating thin film lubrication effects on flow of Jeffrey liquid by a spiraling disk. European Journal of Mechanics – B/Fluids, Vol. 91, 2022, P. 167–176. https://doi.org/10.1016/j.euromechflu.2021.10.002.

46. Ludema, K. C. (1996). Friction, wear, lubrication : a textbook in tribology. USA: CRC-Press.

47. Dykha, O. V. Principles of construction of the structural-dynamic scheme at boundary greasing, Theses dopov. international scientific and technical conf. "Wear resistance and reliability of friction units of machines (ZNM-2001)." Khmelnitsky : TUP, 2001, P. 52.

48. Zum Gahr, K. (1987). Microstructure and Wear of Materials. Elsevier Science.

49. Mate, C. M., Carpick, R. W. (2019). Tribology on the Small Scale: A Modern Textbook on Friction, Lubrication, and Wear. OUP Oxford. 448 p.

50. Snedden, R. (2001). Energy Transfer. GB: Heinemann Library. 48 p.

51. Abrasion Resistance of Materials. (2012). Croatia : IntechOpen. 212 p.

TRIBOTECHNOLOGIES OF STRENGTHENING AND WEAR MODELING OF STRUCTURAL MATERIALS

Authors:

Myroslav Stechyshyn
Professor, Dr. Sci. Eng., Khmelnytskyi National University,
Faculty of Engineering, Transport and Architecture
Institutska str., 11, Khmelnitsky, Ukraine, 29016
E-mail: miro011951@gmail.com
+38 098 58 918 14

Marek Macko
Associate Professor, Dr. Sci. Eng., Kazimierz Wielki University
Faculty of Mechatronics,
Kopernika 1 Street, 85-044 Bydgoszcz, Poland
E-mail: marek.macko@ukw.edu.pl
+48 52 32 57 623

Oleksandr Dykha
Professor, Dr. Sci. Eng., Khmelnytskyi National University,
Faculty of Engineering, Transport and Architecture
Institutska str., 11, Khmelnitsky, Ukraine, 29016
E-mail: tribosenator@gmail.com
+38 097 55 469 25

Serhii Matiukh
Associate Professor, PhD, Khmelnytskyi National University
Faculty of International Relations and Law,
Institutska str., 11, Khmelnitsky, Ukraine, 29016
E-mail: matuh@khmnu.edu.ua
+38 097 99 807 52

Janusz Musial
Associate Professor, Dr. Sci. Eng., Kazimierz Wielki University
Faculty of Mechatronics,
Kopernika 1 Street, 85-044 Bydgoszcz, Poland
E-mail: janusz.musial@ukw.edu.pl
+48 52 32 57 642